

Diss. ETH No. 16736

Measurement of Fracture Mechanical Properties of Snow and Application to Dry Snow Slab Avalanche Release

A dissertation submitted to the
SWISS FEDERAL INSTITUTE OF TECHNOLOGY ZÜRICH
for the degree of
DOCTOR OF SCIENCES

presented by

CHRISTIAN SIGRIST

Master of Science in Physics, University of Bern

born 24.03.1976

citizen of Sigriswil, Bern

accepted on the recommendation of
Prof. Dr. Jürg Dual, examiner
Dr. Jürg Schweizer, co-examiner
Dr. Hans-Jakob Schindler, co-examiner

2006

Abstract

A dry snow slab avalanche is released by a sequence of failure processes in the snow cover. When a weak layer in the snow cover is damaged over a certain area, the weak layer starts to fail progressively in slope parallel direction. This shear failure disconnects the overlying slab from the basal layer. Finally, a tensile fracture occurs in slope normal direction across the layering which releases the slab. For a better understanding of these mechanisms a well founded understanding of the fracture mechanical properties of homogeneous and layered snow is essential.

The aim of this work was to investigate the fracture mechanical properties of snow under tension (mode I) and under shear (mode II) with homogeneous and layered snow samples on the basis of experiments in the cold laboratory and in the field and to relate the results to dry slab avalanche release. The experimental work was structured in three groups of fracture experiments: experiments in mode I with homogeneous snow samples in the cold laboratory, experiments in mode II with layered snow samples in the cold laboratory and mode II experiments with in-situ snow beams in the field.

For the mode I experiments, beam-shaped snow specimens cut from homogeneous layers of naturally deposited snow were subjected to three-point bending and cantilever beam tests. Uncracked specimens were used to determine the tensile strength of snow and notched specimens to determine the critical stress intensity factor in mode I. The three-point bending tests provided higher values than the cantilever beam tests. Furthermore the cantilever beam tests depended on cantilever length. The differences between the test methods were significant and were attributed to non-negligible size and shape effects. The fracture process zone was experimentally determined and was estimated to be in the order of several centimeters, implying that snow has to be considered as a quasi-brittle material at the scale of our experiments. For a quasi-brittle material linear elastic fracture mechanics is applicable only with a size correction. As a method to correct the critical stress intensity factor to the size-independent fracture toughness, K_{Ic} , which is a material property, the equivalent fracture toughness, K_{Ic}^e , was determined according to Bazant and Planas (1998) and a size correction function was proposed. The results for K_{Ic}^e ranged from $0.8 \text{ kPa}\sqrt{\text{m}}$ for a density of $\rho = 150 \text{ kg/m}^3$ up to $6 \text{ kPa}\sqrt{\text{m}}$ for a density of $\rho = 350 \text{ kg/m}^3$ for typical slab layers. It was confirmed that snow has an extremely low value of K_{Ic} . Fracture toughness is expected to be size dependent up to

the scale of a slab avalanche.

Layered snow samples including a weak layer were tested in mode II to determine the energy release rate of a crack propagating along the weak layer. A new experimental setup based on a cantilever beam experiment was designed and proved to be applicable for layered snow samples. In absence of an analytical solution, the finite element method (FEM) was used to simulate the experiments and determine the energy release rate numerically. A critical energy release rate $G_f = 0.04 \pm 0.02 \text{ J/m}^2$ was found for the tested weak layers. G_f was primarily a material property of the weak layer. For similar snow densities, mode I fracture toughness results were about two times as large as for the tested weak layers in mode II. Two analytical approaches were tested and compared to the FEM results. Both analytical approaches, a homogeneous cantilever beam with a deep crack, and a bilayer beam with interface crack were highly correlated with the results obtained from the FE model. The analytical results of both approaches were too large by a factor of about two. Due to the higher coefficient of determination, the cantilever beam approach should be preferred. In addition, the dynamic Young's modulus of the tested snow samples was determined. The results for the Young's modulus were strongly correlated with an index for the Young's modulus derived from a penetration resistance profile recorded with a snow micro-penetrometer SMP.

A field test was developed in which a weak layer in an isolated snow beam was tested in mode II in-situ on a slope. The critical energy release rate G_f was determined numerically in a FEM simulation. The result for the tested weak layers was $G_f = 0.07 \pm 0.01 \text{ J/m}^2$. It was found that slope normal bending of the slab contributed considerably to the energy release rate G of our tests and was more important than the component due to shear loading for angles between 30° and 45° . Critical crack sizes of about 25 cm were required to start fracture propagation along the weak layer of the isolated beams.

By applying new test methods to snow and acquiring a considerable data set of fracture mechanical properties of snow in laboratory and field tests, it was possible to improve the knowledge and the understanding of the fracture mechanical behaviour of snow. It could be shown that for fracture propagation the material properties of the weak layer as well as of the overlaying slab play an important role. Whereas the energy to fracture a weak layer depends on the material properties of the weak layer, the available energy for crack propagation depends mainly on the material properties of the overlaying slab and the slope normal collapse height of a weak layer. It is expected that this behaviour holds also for the scale of a slab avalanche.

Zusammenfassung

Bevor eine Schneebrettlawine abgleitet, kommt es in der Schneedecke zu einer Reihe von Bruchprozessen. Sobald eine genügend grosse Fläche einer Schwachschicht in der Schneedecke geschädigt ist, kommt es zu einer selbstständigen Bruchausbreitung entlang dieser Schwachschicht in hangparalleler Richtung. Durch diesen Scherbruch wird das Schneebrett von der darunter liegenden Schicht getrennt. Unter der zunehmenden Last kommt es zu einem Zugbruch senkrecht zur Hangrichtung der zum abgleiten des Schneebrettes führt. Um diese Mechanismen besser verstehen zu lernen ist es wichtig, vorerst einmal die bruchmechanischen Eigenschaften von homogenem und geschichtetem Schnee zu kennen.

Die Zielsetzung dieser Arbeit war es, in Labor- und in Feldexperimenten die bruchmechanischen Eigenschaften von Schnee unter Zugbelastung (Mode I) und unter Scherbelastung (Mode II) experimentell zu bestimmen und die Resultate auf die Auslöseprozesse einer Schneebrettlawine zu übertragen. Die experimentelle Arbeit wurde in drei Gruppen unterteilt: Mode I Experimente mit homogenen Schneeproben im Kältelabor, Mode II Experimente mit geschichteten Schneeproben im Kältelabor und Mode II Experimente mit Schneeblocken im Gelände.

Für die Mode I Tests wurden balkenförmige Schneeproben aus einer homogenen Schicht der Schneedecke ausgestochen. Diese wurden in Drei-Punkt-Biegeversuchen und in Balkenversuchen mit einem Ausleger (Cantilever beam tests) getestet. Dabei wurden ungekerbte Proben verwendet um die Zugfestigkeit zu bestimmen und vorgekerbte Proben zur Bestimmung der kritischen Spannungsintensitätsfaktoren. Die Resultate der Drei-Punkt-Biegeversuchen fielen höher aus als diejenigen der Balkenversuche. Die Resultate der Balkenversuche wurden zudem durch die Länge des Auslegers beeinflusst. Die signifikanten Unterschiede zwischen den verschiedenen Testmethoden wurden nicht vernachlässigbaren Grössen- und Formabhängigkeiten zugeordnet. Die Grösse der Bruchprozesszone wurde aus Experimenten auf einige Zentimeter geschätzt. Dies zeigt, dass für die Grössenordnung unserer Experimente Schnee als quasi-brüchiges Material angesehen werden muss. Handelt es sich um ein quasi-brüchiges Material, ist die linear elastische Bruchmechanik nur mit einer Grössenkorrektur anwendbar. Um die gemessenen kritischen Spannungsintensitätsfaktoren auf die grössenunabhängige Bruchzähigkeit, K_{Ic} , zu korrigieren, wurde die äquivalente Bruchzähigkeit K_{Ic}^e , nach Bazant und Planas (1998) bestimmt. Für ty-

pische Schneeschichten reichten die Resultate für K_{Ic}^e von $0.8 \text{ kPa}\sqrt{\text{m}}$ für eine Dichte von $\rho = 150 \text{ kg/m}^3$ bis $6 \text{ kPa}\sqrt{\text{m}}$ für eine Dichte von $\rho = 350 \text{ kg/m}^3$. Damit konnte bestätigt werden, dass Schnee eine extrem niedrige Bruchzähigkeit hat. Es wird erwartet, dass die Bruchzähigkeit bis hin zur Grösse eines Schneebrettes Grössenabhängig ist.

Aus Experimenten mit geschichteten Schneeproben die eine Schwachschicht enthielten wurde die Energiefreisetzungsrate in Mode II bestimmt. Dafür wurde ein neuer experimenteller Aufbau entwickelt, der auf einem Balkenexperiment beruht. Da keine analytische Lösung für die Bestimmung der Energiefreisetzungsrate zur Verfügung stand, wurde diese numerisch, mittels der finiten Element Methode (FEM) bestimmt. Für die getesteten Schwachschichten wurde eine kritische Energiefreisetzungsrate von $G_f = 0.04 \pm 0.02 \text{ J/m}^2$ bestimmt. G_f war in erster Linie eine Materialeigenschaft der Schwachschicht. Für Schnee vergleichbarer Dichte war die Bruchzähigkeit in Mode I etwa doppelt so gross wie in Mode II. In der Folge wurden die FEM Resultate mit den Resultaten zweier adaptierter analytischer Lösungen verglichen. Es handelte sich dabei um eine analytische Lösung eines homogenen Auslegerbalkens mit einem tiefen Riss und einer Lösung für einen Balken bestehend aus zwei Schichten mit einem Schichtgrenzriss. Die Resultate der analytischen Lösungen waren gut korreliert mit den FEM Resultaten, aber überstiegen diese für beide Lösungen um einen Faktor zwei. Auf Grund des höheren Bestimmtheitsmasses, sollte die Auslegerbalken-Lösung vorgezogen werden. Zusätzlich wurde das Elastizitätsmodul der getesteten Schneeproben bestimmt. Die Resultate waren gut korreliert mit einem Elastizitätsindex der aus einem Eindringwiderstandsprofil eines Schnee-Mikro-Penetrometers (SMP) bestimmt wurde.

Ein Feldtest wurde entwickelt in dem Schwachschichten in allseitig isolierten Schneeblocken direkt im Hang in Mode II getestet wurden. Die kritische Energiefreisetzungsrate wurde numerisch in einer FEM Simulation bestimmt. Für die getesteten Schwachschichten lag die kritische Energiefreisetzungsrate bei $G_f = 0.07 \pm 0.01 \text{ J/m}^2$. Ein Durchbiegen des Schneebrettes rechtwinklig zum Hang trägt erheblich zu G bei und kann für Hangneigungen zwischen 30° und 45° den Beitrag auf Grund der Scherbelastung sogar überwiegen. Kritische Schnittlängen von 25 cm waren nötig, um eine selbstständige Bruchausbreitung entlang der Schwachschicht auszulösen.

Mit den neuen Testmethoden konnte im Labor und im Feld eine repräsentative Datenmenge der bruchmechanischen Eigenschaften von Schnee gesammelt werden. Damit war es möglich das Wissen und Verständnis um die Bruchmechanik von Schnee zu erweitern. Es konnte gezeigt werden, dass für die Bruchausbreitung im Schnee sowohl die Schwachschicht als auch das darüber liegende Schneebrett eine entscheidende Rolle spielen. Während die Energie die benötigt wird um eine Schwachschicht zu brechen von den Eigenschaften der Schwachschicht abhängt, hängt die für den Bruchprozess zur Verfügung stehende Energie vor allem vom Schneebrett ab. Es wird angenommen, dass dies nicht nur für den experimentellen Fall, sondern auch für den Fall eines Schneebrettes gilt.

List of Symbols

Symbol	Description	Unit
A	Cross sectional area	m^2
a	Crack length or cut length	m
$da, \Delta a$	Crack or cut extension	m
a_c	Critical crack or cut length	m
b	Ligament width	m
D	Specimen or structure size	m
D_0	Characteristic structure size	m
E	Young's modulus	Pa
F	Applied force	N
F_f	Force leading to specimen failure	N
G	Energy release rate	J/m^2
G_f	Critical energy release rate	J/m^2
G_c	Effective critical energy release rate	J/m^2
g	Gravitational acceleration	m/s^2
H	Slab thickness	m
h	Specimen height	m
K	Stress intensity factor	$Pa\sqrt{m}$
$K_{I,II,III}$	Stress intensity factor in mode I, mode II and mode III	$Pa\sqrt{m}$
K_c	Fracture toughness	$Pa\sqrt{m}$
K_{Ic}^e	Equivalent fracture toughness	$Pa\sqrt{m}$
K_f	Critical stress intensity factor	$Pa\sqrt{m}$
L	Length of protruding part (CB-test)	m
l	Specimen length	m
M	Moment	Nm
M_f	Bending moment due to applied force (per specimen width)	N
M_G	Bending moment due to body weight (per specimen width)	N
m	Mass	kg
P	Applied load	N
R	Size of the fracture process zone	m
R_c	Maximum size of the fracture process zone	m
r, \vec{r}	Position, position vector	m

Symbol	Description	Unit
S	Shear modulus	Pa
s	Span (Distance between supporting points, 3PB-test)	m
t	Layer thickness	m
U	Stored elastic strain energy	J
U^*	Complementary strain energy	J
u	Displacement	m
V_e	Elastic energy	J
V_f	Fracture energy	J
V_g	Gravitational energy	J
w	Specimen or body width	m
w_f	Specific fracture energy	J/m ²
Greek		
α	Inclination of weak layer to the vertical	°
δ	Crack tip opening displacement (CTOD)	m
ε	Deformation	
$\dot{\varepsilon}$	Deformation rate	1/s
$\theta(x)$	Heaviside step function	
ν	Poisson's ratio	
ξ	Bimaterial constant	
ρ	Density	kg/m ³
σ, σ_{ij}	Stress, stress component ($i = 1, 2, 3; j = 1, 2, 3$)	Pa
σ_c	Tensile strength (Maximum stress a material can sustain. Equal to σ_f if no crack is present)	Pa
σ_{coh}	Cohesive stress (cohesive crack model)	Pa
σ_{coh}^{max}	Maximum cohesive stress (cohesive crack model)	Pa
σ_f	Nominal failure stress = nominal strength	Pa
σ_N	Nominal stress (Load divided by the original undeformed and uncracked cross section)	Pa
σ_{Na}	Effective stress (Load divided by the remaining cross section)	Pa
σ_y	Plastic yield strength (Stress that is necessary to initiate inelastic behaviour in ductile materials)	Pa
τ	Shear stress	Pa
τ_c	Shear strength	Pa
τ_g	Shear stress due to a gravitational load	Pa
τ_p	Peak (maximum) shear stress	Pa
τ_r	Residual shear stress	Pa
ϕ	Position angle (polar coordinate system)	
φ	Slope angle, inclination of weak layer to the horizontal	°
Ψ	Phase angle of loading	
Others		
\mathfrak{D}	Flexural rigidity	Nm

Symbol	Description	Unit
Subscript		
b	bottom	
c	critical (for material properties)	
f	failure	
t	top	
WL	weak layer	
y	yield, yielding	

Seite Leer /
Blank leaf

Contents

Acknowledgements	v
1 Introduction	1
1.1 Living with avalanche danger	1
1.2 Snow as a material	2
1.3 Snow avalanche formation	5
1.4 Dissertation outline	12
2 Fracture mechanics	15
2.1 Definition and history	15
2.2 Strength of materials vs. fracture mechanics	16
2.3 Linear elastic fracture mechanics	17
2.3.1 Energy release rate and specific fracture energy	17
2.3.2 Stress intensity factor and fracture toughness	18
2.3.3 Energy release rate versus stress intensity factor	20
2.4 Non linear extensions	20
2.4.1 Brittle, ductile and quasi-brittle fracture behaviour	21
2.4.2 Fracture process zone	22
2.4.3 Consequences of quasi-brittle behavior	24
2.5 Failure of interfaces	27
2.5.1 The complex stress intensity factor	27
2.5.2 Energy release rate for an interface crack	28
2.6 Application of fracture mechanical concepts to snow	29
2.6.1 Experimental studies	29
2.6.2 A model for shear fracture propagation	30
2.6.3 A model for a slope normal displacement of the slab	32
3 Methods	35
3.1 Standard measurement techniques for snow characterization	35
3.2 Laboratory tests	37
3.2.1 Sample collection	37
3.2.2 Three-point bending test	38
3.2.3 Cantilever beam test	41

3.2.4	Shear fracture test	43
3.2.5	FE model of shear fracture test	45
3.3	Field test	47
3.3.1	FE model of field test	49
3.4	Young's modulus	49
3.4.1	Dynamic measurement with cyclic loading device	51
3.4.2	Derived from penetration resistance	51
3.5	High-speed photography	53
4	Results	55
4.1	Fracture in homogeneous snow samples	55
4.1.1	Behaviour of snow under loading	57
4.1.2	Tensile strength	58
4.1.3	Critical stress intensity factor in mode I from 3PB-tests	59
4.1.4	Critical stress intensity factor in mode I from CB-tests	61
4.1.5	Quantification of the size effect	63
4.1.6	Fracture process zone	68
4.1.7	Application of the failure assessment diagram	69
4.1.8	Fracture speed in mode I	70
4.2	Fracture in layered snow samples	73
4.2.1	Tested weak layers	73
4.2.2	Young's modulus	75
4.2.3	Energy release rate in mode II	79
4.2.4	Comparison of analytical approaches to FEM results	81
4.2.5	Comparison of mode I and mode II results	83
4.3	Fracture of weak layers on slopes	85
4.3.1	Shear strength of the tested weak layer	85
4.3.2	Energy release rate for the tested weak layer	88
4.3.3	Influence of bending	90
4.3.4	Analytical approach for the field experiments	95
5	Discussion	99
5.1	Fracture in mode I	99
5.1.1	The load-displacement curve	99
5.1.2	The bending experiment to determine tensile strength	100
5.1.3	Comparison of 3PB-tests and CB-tests	101
5.1.4	Fracture speed	103
5.2	The limitation of LEFM for snow	105
5.2.1	The size correction function	105
5.2.2	The fracture process zone	106
5.2.3	The FAD	107
5.3	Fracture in mode II	108
5.3.1	Determination of the Young's modulus	108
5.3.2	Energy release rate in a mode II fracture	110

5.3.3	Comparing numerical and analytical solutions	111
5.3.4	Comparing mode I and mode II results	112
5.4	Field experiments	112
5.4.1	Failure behaviour	112
5.4.2	Energy release rate measured in the field	113
5.4.3	FEM results	114
5.4.4	Analytical approach	115
5.4.5	Further use of the field test	116
6	Conclusions	117
6.1	Summary	117
6.2	Conclusions	117
6.3	Outlook	122
	Bibliography	125
A	Calculation of errors	133
A.1	The error of σ_N	133
B	Stratigraphic snow cover profiles	135
	Acknowledgements	
	Curriculum Vitae	

Introduction

1.1 Living with avalanche danger

The oldest documents reporting on avalanches can be traced back to the time between the 12th and 14th century. In this period, the Walser and the Alemanni started to settle even the remotest valleys of the European Alps in search of new living space (Ammann et al., 1997). From that time on the settlers were increasingly exposed to the specific dangers of the alpine terrain including mud flows, rock falls, landslides and snow avalanches, the subject of this thesis. Step by step they learned to live with the danger and began to search for protection. Already in medieval times people recognized that avalanche frequency increased when they cut down too much of the alpine forest. Letters dating from this time testify that the clearing of forest was prohibited in some exposed areas. In the 19th century people started to build avalanche defence structures high up the mountain slopes in areas where avalanches tended to release. First they used wood or stones to build up fences or walls which were replaced by large steel structures from the beginning of the 1950ies. Countless damage could be prevented since then, but up to now it is not possible to control the danger caused by avalanches completely. Avalanches can not be predicted in space and time nor can their extension and runout path be foreseen in detail.

Nowadays avalanches are not only threatening alpine infrastructure like buildings, roads or railways but also an increasing number of people following their outdoor activities in the snow covered mountains. Skiing and snowboarding beyond the controlled runs has become very popular in recent years and about 90% of an average of 26 fatalities per year in the Swiss Alps can be attributed to winter sports (Tschirky et al., 2000). The fatal human triggered avalanches are in 90% triggered by the victims or by another member of their group (Schweizer and Lüttschg, 2001), or in other words, the victims actively expose themselves to danger.

Since the 1940ies the Swiss avalanche warning service has provided information on the

actual avalanche situation in Switzerland. Today, a forecast of the avalanche danger for the next day, the so called avalanche bulletin¹, provides the basis for decisions of local authorities, persons in charge of road safety, ski patrols and backcountry skiers. The avalanche forecast has proved to be an indispensable tool to prevent accidents over the past years. However, the predictability of the avalanche danger is limited. Today, avalanche forecasters use a heuristic approach to estimate the avalanche probability and characteristics. For a specific situation, the influence of the contributory factors, such as terrain, meteorological conditions (precipitation, temperature, wind, radiation) and snowpack including its stability, are empirically weighted. Provided that the relevant factors are considered, the precision of the forecast depends on how precise every contributory factor can be determined, if measurable at all. Especially the stability of the snowpack is still difficult to assess. Another approach to assess avalanche danger would be to study and model the physical and mechanical processes of avalanche formation (Schweizer et al., 2003).

With the aim to increase and improve the knowledge of the physical and mechanical processes involved in avalanche formation, an internal research program was initiated at the Swiss Federal Institute for Snow and Avalanche Research, SLF, five years ago. The results of this program should help to increase the predictability of the avalanche release potential and should further improve the avalanche warning in general. Therefore, several research projects were launched including projects on spatial variability of the snow cover, on an improved description of the vertical layering of the snow cover with special emphasis on so called weak layers, on modelling of the slab release process in 3D, and on fracture nucleation and propagation in the snow cover. The present work is a contribution to the last topic.

1.2 Snow as a material

Consulting the Encyclopædia Britannica on "Snow" results in: *"Snow is the solid form of water that crystallizes in the atmosphere and, falling to the Earth, covers, permanently or temporarily, about 23 % of the Earth's surface."* It is true that the atmosphere is the only place where natural snow is formed. If not, the development of man made snow would probably never have been necessary. However, we will only focus on natural snow in this work.

The appearance of snow lying on the ground is completely different from the well known hexagonal shape of a snow flake (Figure 1.1.a). In the following, the most relevant microstructural and mechanical properties of natural snow will be described. The order of the properties in the following list was chosen in order to give a logical sequence of the necessary definitions. The properties were not arranged according to their relevance.

¹Between November and April, the avalanche bulletin is provided on a daily basis and available free of charge on the internet: <http://www.slf.ch/avalanche/bulletin-de.html>

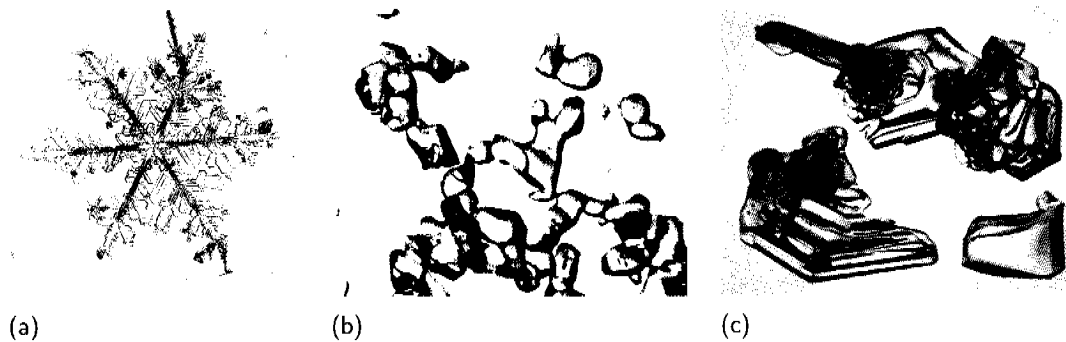


Figure 1.1: (a) Typical hexagonal snow flake, 1 mm in diameter. (b) Small rounded grains, 0.25-0.5 mm. (c) Depth hoar, 1-2 mm, (Pictures: archive SLF).

Highly temperature dependent: The temperature of the seasonal snow cover is close to its melting point $T_{snow} \geq 0.95 T_{melt}$ ($T_{melt} = 273.2\text{K}$) resulting in a strong temperature dependence of all mechanical properties. When the temperature increases in a snow slab, the microstructural stability tends to increase on a long term, because, due to the metamorphism, bonds grow more quickly (McClung, 1996). However, on a short term the stiffness or hardness of a slab decreases with increasing temperature favouring fracture processes in a slope (Schweizer and Jamieson, 2003). This shows that it is of great importance to control the temperature while performing mechanical experiments with snow. The use of a cold laboratory can guarantee the best possible control over temperature.

Sintering: Sintering is a thermal process in which particles are bonded together via mass transport events (German, 1996). Sintering is used in industry to form many objects out of powders. Snow and ice are probably the only natural materials that experience this effect without external force. This is a result of the existence of snow close to its melting point. If two snow blocks are brought into contact, even without pressure, they start to sinter together within seconds, or in other words, snow has the ability to "heal" after a fracture. The same happens when snow flakes touch the ground and get in contact with each other, they start to sinter and change from an almost cohesionless to a bonded, porous or foam like material with a complex, three-dimensional microstructure.

Complex micro structure: Natural snow is an ice-matrix filled with air and water vapour (Figure 1.2). When the snow temperature is around 0°C , the ice-matrix can also contain water. Very soft, newly fallen snow has a density (ρ_{snow}) of about 60 kg/m^3 . Well settled old snow has a density of about 550 kg/m^3 , above this density one speaks of firn. Hence, a relative density range (ρ_{snow}/ρ_{ice}) of 0.05 to 0.60 results, where the density of ice is $\rho_{ice} = 917\text{ kg/m}^3$. This corresponds to a porosity of 95% to 40%. At first sight snow seems to be comparable to other cellular solids such as wood, bone or industrial foams. Kirchner et al. (2000) suggested to describe snow as a foam of ice and to use the theory of cellular

Table 1.1: Snow compared to other porous materials. Data from Gibson and Ashby (1997).

Material	Density ρ (kg/m ³)	Relative density ρ/ρ_{solid}	Porosity	Tensile strength σ_c (kPa)
Snow	50–550	0.05–0.60	40%–95%	0.5–200
Cancellous Bone	95–1330	0.05–0.70	30%–95%	2'000–20'000
Wood	200–750	0.13–0.50	50%–87%	70'000–100'000

materials of Gibson and Ashby (1997) for interpreting mechanical data of snow. However, there is a difference between most cellular solids and snow: Snow includes a lot of ice structures protruding into space with no connection to the surrounding ice-matrix. Such structures contribute to the ice mass but they do not contribute to the overall strength of the material, because they can not take any load. This leads to the fragile nature of snow and to a low tensile strength (Table 1.1).

Brittle to ductile transition: The behaviour of snow under loading, depends very much on how fast it is loaded. For fast loading, i.e. for high strain rates ($\dot{\epsilon} > 10^{-3} \text{ s}^{-1}$), snow behaves brittle and can approximately be considered as linear elastic material. (Limitations will be discussed in Section 2.4). For low strain rates ($\dot{\epsilon} < 10^{-5} \text{ s}^{-1}$), snow behaves ductile and has to be considered as viscoelastic material. A transition from brittle to ductile behaviour can be found at a strain rate of approximately 10^{-4} s^{-1} depending on temperature and microstructure (Narita, 1980). Snow creep is a common phenomenon in the ductile range and the determination of snow creep forces on avalanche defence structures was one of the problems which prompted the study of snow mechanics in the first half of the 20th century (Bader et al., 1939). Avalanche formation however, involves fast loading processes and therefore the brittle range will be of relevance in this thesis.

Low specific strength: The very brittle nature of snow is manifested in its low specific strength, meaning the tensile strength divided by the density (σ_c/ρ). Jamieson and Johnston (1990) found a relation between tensile strength of snow and snow density of $\sigma_c = 79.7 (\rho/\rho_{ice})^{2.39} \text{ kPa}$, which might hold up to densities of about 350 kg/m^3 . As an example this relation leads to a tensile strength of 2.1 kPa for a snow density of 200 kg/m^3 . The density of ice ρ_{ice} is 917 kg/m^3 . Thus, for a very low snow density of 60 kg/m^3 a specific strength of 2 Nm/kg results. For 350 kg/m^3 the specific strength equals 23 Nm/kg . These are extremely low values compared to the specific strength of ice, $10'000 \text{ Nm/kg}$ ($\sigma_{ice} = 9 \text{ MPa}$), or aluminium, $30'000 \text{ Nm/kg}$. Even commonly used industrial foams have much larger specific strengths ranging from 1000 to $10'000 \text{ Nm/kg}$.

Metamorphism: Snow microstructure changes with time due to its existence close to the melting point. Ice sublimates in the snow cover and if a vapour pressure

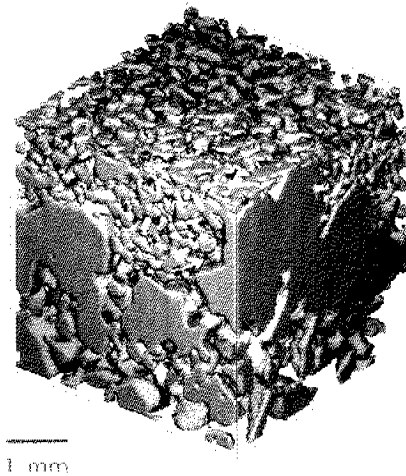


Figure 1.2: Three-dimensional reconstruction of a snow sample imaged by micro computer tomography. Fine rounded grains on top of an ice layer. Below the ice layer are faceted grains. (M. Schneebeli, SLF)

gradient is present, the vapour is transported upwards along the gradient and finally recondensates at a colder position in the ice-matrix (Arons and Colbeck, 1995). These processes have a time scale of hours to days. The ice-matrix is commonly divided in grains which are connected by bonds. The metamorphism changes the shape and the size of the grains. Formerly rounded grains (Figure 1.1.b) change to a more angular shape (Figure 1.1.c) and increase in size. The various grain shapes are classified in grain types (Colbeck et al., 1990). Although the mechanical properties of snow consisting of different grain types can vary strongly, snow of different grain types can have the same density. Therefore, density is not a sufficient criterion to characterize mechanical properties. Additional to the density, the grain type has always to be specified.

1.3 Snow avalanche formation

Snow avalanches are generally divided in two categories, loose snow avalanches and slab avalanches (e.g. McClung and Schaerer, 1993, p. 61). *Loose snow avalanches* start at a single point at the snow surface and move down the slope as a cohesionless mass spreading out to a triangular shape, comparable to the slipping of sand. Generally, only a cohesionless surface layer is involved. *Slab avalanches* consist of a cohesive snow slab that is released over a plane of weakness (Figure 1.3). During the release the slab breaks apart. Slab avalanches are far more dangerous than loose snow avalanches because they involve much larger snow masses and higher speeds. Slab avalanches can further be



Figure 1.3: Dry snow slab avalanche, released at Grialetsch, Switzerland in March 2006.

divided in dry snow and wet snow avalanches. While wet snow avalanches occur mainly in spring in the European Alps, when temperatures are rising, dry snow slab avalanches are endangering people and infrastructure during the whole winter season and can be attributed for most of the fatalities. In this thesis we concentrate on the formation of dry snow slab avalanches.

Snow avalanche formation is an interplay between several factors. The five most relevant formation factors and therefore the most contributing factors to avalanche danger are: *terrain* (a slope angle of more than 30° is required), *precipitation* (snow fall, occasionally rain), *temperature* (including radiation effects), *wind* and the *snow cover* (Schweizer et al., 2003).

The natural snow cover is vertically layered comparable to a sandwich. Each layer is the result of a snow fall or a wind transport event. Each interface between two layers was once the surface of the snow cover and was influenced by the atmosphere before it was buried by a new layer of snow. The layers can be characterized and distinguished according to the grain type, the grain size and the hardness. A critical situation occurs when two layers are badly connected, either because the bonds at the interface are weak or because in between is a small layer that is weaker than the adjacent layers below and above (Figure 1.4). A weak layer or an interface below a thicker cohesive slab within the snow cover is a prerequisite but not a sufficient condition for slab avalanche release.

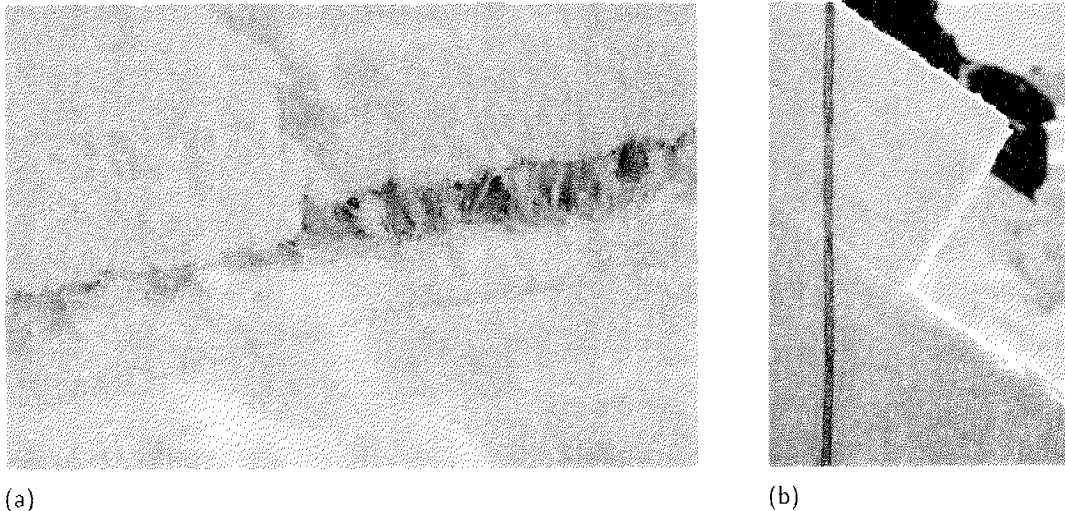


Figure 1.4: (a) A weak layer consisting of buried surface hoar crystals, collapsed on the left side and still intact on the right, from Jamieson and Schweizer (2000). (b) Crown fracture of an avalanche. A cohesive slab lays on top of a thin weak layer, from Schweizer et al. (2003).

The properties of the overlaying slab have also to be taken into account (McClung and Schweizer, 1999).

Up to now, there is practically no hard evidence about how a slab avalanche is released. This is due to the fact, that all essential processes occur in the snow cover and can not directly be observed. A closer look at the snow cover while a slab avalanche is released would simply be too dangerous. However, based on observations of slab triggering by persons or explosives, many of them recorded on videotape, there is indirect evidence that the release process can be divided in three successive steps (Figure 1.5): First, a fracture is initiated in a weak layer, then the weak layer fails progressively in a slope parallel direction and finally a tensile fracture occurs vertical to the slope which releases the avalanche.

The terms *fracture* and *failure* are used as follows in this thesis: The term *fracture* is used to describe an explicit fracture mechanical process in tension or shear. The more general term *failure* is used, when it is not clear from a macroscopic point of view, if the process can be treated in a classic fracture mechanical sense. However, from a microscopic point of view, any failure in snow will involve fracture of ice bonds, thus the distinction between fracture and failure is also a matter of scale.

1. **Failure initiation:** A failure in a weak layer can be triggered either artificially, by an abrupt stress increase due to a skier or the detonation of an explosive, or alternatively, the failure can be triggered naturally, by increasing stress due to a snow fall event or wind accumulated snow. The majority of dry slab avalanches

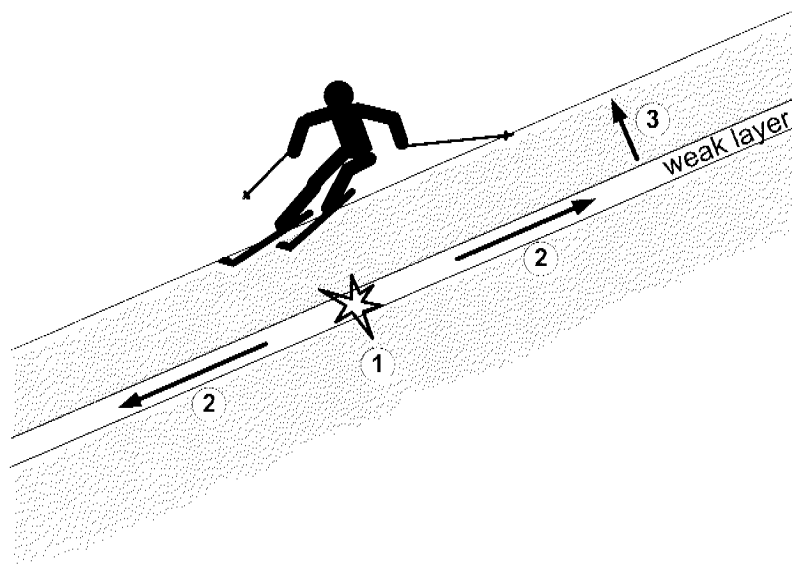


Figure 1.5: Schematic illustration of the slab release process in three steps: Triggering of a failure in a weak layer by a skier (1). Propagating failure along the weak layer (2). Tensile fracture of the slab (3).

release due to loading by new snowfall (McClung and Schaerer, 1993). Once an initial failure has reached a critical size, it leads to a progressive self-propagating failure.

2. **Progressive failure of weak layer:** After an initial failure has reached a certain size, a self-propagating failure spreads out in the weak layer in all directions, similar to the circular waves after a stone has been thrown into water. Self-propagating means that no further increase of the load is needed to propagate the failure. This failure was described as a fracture mechanical process where a crack in the weak layer is loaded in shear due to the inclination of the slope (e.g. McClung, 1979; Schweizer and Jamieson, 2003). However, observations show that the failure of weak layers include a vertical collapse (Figure 1.4a). Recently, the propagation velocity of a collapse in a weak layer was measured in flat terrain (Johnson et al., 2004). Measurements in inclined terrain showed that failures of the tested weak layers were accompanied by a slope normal displacement (van Herwijnen and Jamieson, 2005). The assumption that the failure of a weak layer includes a shear fracture *and* a compressive failure seems justified.
3. **Tensile fracture:** Once the loading due to the weight of the separated slab gets large enough a tensile or crown fracture crosses the overlaying slab layers (Figure 1.4b). The tensile fracture occurs upslope of the fractured weak layer area because tensile stresses are largest there. This fracture combined with two shear fractures on both sides of the slab and a compressive failure at the lower end of the slab

finally releases the slab which slips downslope over the plane of weakness (Figure 1.3).

One crucial question in the research of avalanche formation is how large an initial failure in a weak layer has to be to become critical, leading to failure propagation without further loading. This corresponds to the transition between step one and step two in Figure 1.5. A further question is, once a failure has occurred (step 1) and propagates (step 2), if it still can be arrested by spatial variations in the weak layer. If failure propagation would be arrested, then the failure would most possibly not lead to an avalanche release.

In the following, a summary of recent contributions to the research of avalanche formation is given. The contributions are divided in three groups according to their main focus. The division is meant to give a clearer picture of the topic by collecting contributions that base on similar ideas thereby highlighting interconnections between the contributions. However, the division shall *not* make the impression that the presented contributions and theories are contradictory, they simply approach the avalanche formation process from different directions.

Failure of weak layer: Focus on shear fracture

McClung (1979) started to apply fracture mechanical concepts to model dry snow slab avalanche release, because snow strength turned out to be not a sufficient criterion to determine if a snow slab can be released or not (McClung, 1979, 1981, 1987). He focused on ductile shear failure of the weak layer, followed by shear fracture and propagation. His two dimensional model is based on the work of Palmer and Rice (1973) which describes the growth of a slip interface in a clay mass. A slope parallel fracture in mode II and III is driven by the stress concentrations at the crack tip that form the boundary of the fractured area (Figure 1.6). The model will be discussed in detail in Section 2.6.2.

The numerical models of Bader and Salm (1990) and Stoffel and Bartelt (2003) base on a similar idea. They assume a shear crack propagation based on a linear elastic fracture energy approach. Bader and Salm (1990) assumed an a priori existing zone of weakness (deficit zone) in a weak layer of length $2a$ (Figure 1.6). Based on their model, Schweizer (1999) calculated the length of the deficit zone that is needed for brittle fracture propagation to be between 5 and 35 m, for typical slab properties. By reviewing the existing slab release models, Schweizer (1999) stated that in general a critical length of between 0.1 and 10 m can be calculated. The results of Stoffel and Bartelt (2003) imply that an existing deficit zone in a weak layer of more than 8 m is required to start brittle fracture propagation. McClung and Schweizer (1999) stated that for the case of rapid loading (e.g. induced by a skier) the critical length for fracture propagation would reduce to 0.1–1 m.

The models summarized above have in common that the existence of a deficit zone of a considerable size with zero or negligible strength is a prerequisite. However, nobody has

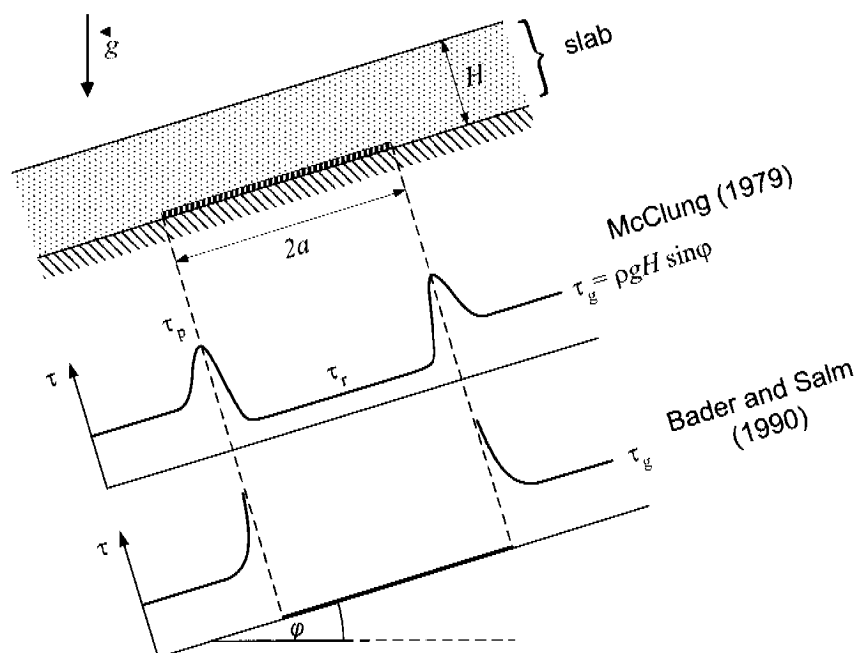


Figure 1.6: Snow slab release models with preexisting weakness (deficit zone). A two-dimensional slope inclined with a slope angle φ and slab height H including a deficit zone of length $2a$. Slope parallel shear stress distribution for two models: McClung (1979) in the middle and Bader and Salm (1990) at bottom, where τ_g is the shear stress due to the slab, τ_p the peak stress and τ_r the residual stress. After Schweizer et al. (2003).

ever observed such a pre-existing crack in a snowpack. And if such a crack or zone would exist, a most recent contribution by Birkeland et al. (2006) indicates that sintering processes would increase the strength between the fractured layers within minutes to hours.

Bazant et al. (2003) applied the model of McClung (1979) to formulate a size effect law for fracture triggering in dry snow slabs. Bazant et al. (2003) suggested that there is a strong thickness effect on the fracture toughness in mode II with the fracture toughness increasing as snow thickness to the power of 1.8 ($K_{IIc} \propto H^{1.8}$). They stated that by fitting the proposed size effect law to fracture data for various slab thicknesses would permit to identify material fracture parameters. This has been done by McClung (2005b). He combined field data with the cohesive crack model to yield estimates for the mode II shear fracture toughness. The values he found ranged from $0.02 \text{ kPa}\sqrt{\text{m}}$ to $13 \text{ kPa}\sqrt{\text{m}}$.

The above mentioned theoretical and numerical models base on the theory of fracture mechanics. However, it is only recently that experimental studies were carried out to determine fracture mechanical parameters of snow (Kirchner et al., 2000, 2002a,b; Faillettaz et al., 2002; Schweizer et al., 2004; Sigrist et al., 2005, 2006). Their findings will

be discussed in detail in Section 2.6 after the necessary background in fracture mechanics has been introduced.

Based on the findings of Wei et al. (1996) on ice-metal interfaces, Schweizer and Camponovo (2001) suggested that fracture propagation would depend on the difference in stiffness between the weak layer and the slab, more precisely the layer just adjacent to the weak layer. In fact, observations at fracture lines of slab avalanches showed that a significant difference in hardness and grain size existed between the layers adjacent to the fracture interface (Schweizer and Jamieson, 2003). Schweizer and Camponovo (2001) proposed that interfacial fracture mechanics should be used to describe these phenomena.

Failure of weak layer: Focus on slope normal collapse

Johnson et al. (2004) studied the fracture propagation of remotely triggered avalanches. They measured the speed of fracture propagating in flat terrain by capturing the characteristic "whumpf" sound with geophones, and found a speed of about 20 m/s. They observed a collapse of the weak layer of 1–2 mm and postulated that compressive fracture of the weak layer, initially triggered by an over-snow traveller on low angle terrain, would provide the work needed for fracture propagation, and that the velocity of the resulting flexural wave in the overlying slab that progressively fractures the weak layer, would depend on the stiffness of the slab.

Heierli (2005), motivated by the experiment of Johnson et al. (2004), proposed an analytical model for a solitary flexural wave, propagating in a layered snowpack including a collapsible weak layer. The energy for fracture propagation is delivered by the release of potential energy. This means that a collapsible weak layer with a defined vertical extension is a prerequisite, in contrast to the model for shear fracture propagation of McClung (1979) which assumes a weak layer with no slope normal extension. With this model it is possible to calculate propagation velocity of the wave, its characteristic length and maximum strain rate at the crack front of the wave. Heierli (2005) calculated a fracture speed of 20 m/s, for the conditions of the experiment performed by Johnson et al. (2004).

van Herwijnen and Jamieson (2005) recorded self-triggered fractures in weak snowpack layers with a high-speed camera. Independent of the slope angle, they observed slope normal displacement in all fractured weak layers. They measured an average propagation speed of 20 m/s. However, they could not determine whether the fracture was accelerating or not.

Most recently, Heierli and Zaiser (2006) proposed an analytical model on fracture nucleation in a collapsible stratification. The crack energy associated with a localized collapse of the weak layer is calculated. Thereby, size and energy of a critical crack can be evaluated as function of the material properties of the overlying slab and the fracture energy of the weak layer. This model will be discussed in detail in Section 2.6.3.

Spatial variability

Schweizer (2002), Kronholm and Schweizer (2003) and Kronholm et al. (2004) proposed that the spatial irregularity of the snow cover in respect to snow depth, layering, hardness and grain size – the so-called spatial variability of a snow slope – may also have an important influence on the fracture propagation potential and on avalanche formation in general. A high spatial variability on a small scale, that is within one square meter, may increase the probability of a fracture initiating in this area, whereas a high spatial variability on a larger scale, that is within a few square meters, may have a stabilizing effect on the snow slope, because a fracture cannot propagate far enough to release a slab avalanche. Consequently, scale effects have also a big influence on fracture propagation.

Zaiser (2004) and Fyffe and Zaiser (2004) formulated a theoretical model to investigate the influence of random variations in strength of the weak layer. They used a cellular automata model and modelled the weak layer as a displacement softening interface. No pre-existing crack is necessary in their model. They concluded that the critical flaw leading to failure is neither an extended shear band nor a point like deficit, but damage clusters of widely varying sizes.

Kronholm and Birkeland (2005) also considered the effect of spatial variation and used a cellular automata model as well. In contrast to Zaiser (2004) and Fyffe and Zaiser (2004), they did not use random variations of shear strength in the weak layer but used field data of spatial variability of weak layers (Kronholm, 2004) as input. They concluded that fractures through snowpack weak layers with large-scale spatial structure are much more likely to propagate over large areas than fractures through weak layers with smaller-scale spatial structure.

1.4 Dissertation outline

Before this study, there was only limited data available on fracture mechanical properties of snow (see also Section 2.6). Furthermore, the experimental studies that were made had the following restrictions:

- Tests have only been carried out on homogeneous snow samples.
- Field tests were performed with no adequate temperature control.
- A linear elastic fracture behaviour was assumed, although the specimen size requirements were not fulfilled.
- The mode I experiments were in fact mixed mode experiments (including mode I and II).
- A dependence of fracture toughness on the cantilever length could not be explained plausibly.

- The few available data for mode II fractures are based on an experimental setup which includes also a mode I component.

The aim of this thesis was to measure relevant fracture mechanical parameters of snow, assess the applicability of different fracture mechanical theories for snow and propose a conceptual model for the fracture processes involved in slab release. To achieve this aim, the following objectives were defined:

1. Assess the relevance of fracture toughness for fracture propagation / resistance in snow and for snow slab release in general. Relate fracture toughness to other mechanical properties.
2. Design a suitable experimental setup and determine snow fracture toughness in tension for homogeneous snow samples.
3. Design a suitable experimental setup and determine snow fracture toughness in shear for layered snow samples.
4. Quantify size and shape effects, so that the results of small scale experiments can be transferred to the slope scale.
5. Develop a conceptual model which relates measurable fracture mechanical properties of snow (objectives 1.-4.) to the fracture processes involved in slab release.
6. Design a field test, based on the experience with the different laboratory tests and determine in-situ fracture mechanical properties.

The thesis proceeds as follows: Chapter 2 gives the necessary background on fracture mechanics and points out what has been done so far to adapt fracture mechanical theories to snow. Chapter 3 explains the required common measurement techniques in snow and goes into detail on the experimental setups for the different fracture mechanical tests that were designed and tested in the laboratory and the field. In Chapter 4 the results of the fracture experiments are presented that were acquired with homogeneous snow samples for the tensile experiments and with layered samples for the shear experiments. A discussion of the results including some extrapolations of the laboratory results to the slope scale are given in Chapter 5. Overall conclusions are drawn in Chapter 6 and an outlook is given together with recommendations for future work.

Seite Leer /
Blank leaf

Fracture mechanics

The basic problem in fracture mechanics is to find the amount of energy available for crack growth and to compare it to the energy required to extend the crack. Although conceptually simple, the problem is far from trivial.

Bazant and Planas (1998)

2.1 Definition and history

A fracture is a process which partly or fully separates an originally intact body under external loading. The difficulty to describe fracture processes analytically originates in the fact that these processes take place in a very local area around the crack tip and are affected by non-linear effects. Therefore, the strength of materials theory is hardly suited to describe fractures. The description of such processes is part of a failure theory called fracture mechanics. The theory of fracture mechanics complements the strength of materials theory (e.g. Schindler, 2004).

The roots of fracture mechanics reach back to experiments of Leonardo da Vinci, who found that the strength of iron wires decreased with increasing length of the wire (Anderson, 1995). In the last century, Griffith (1921) was the first to formalize the basic equations for crack propagation based on a global energy balance criterion. However, the breakthrough of fracture mechanics took only place in the late 1950s, Irwin (1957) was the first to characterize the situation at the crack tip with the stress intensity factor. The resulting K -concept is a cornerstone of linear elastic fracture mechanics. From the

beginning of the 1960s linear elastic fracture mechanics was expanded to elastic-plastic problems and in the 1980s forms of fracture mechanics appeared that could be applied to so called quasi-brittle materials such as concrete. Despite the substantial progress that has been made in the past decades, the theory of fracture mechanics is by far not completed. Still intensive research takes place in many different fields of fracture mechanics. The author had the opportunity to experience this large effort on occasion of the 11th International Conference on Fracture in Turin, Italy in spring 2005, where more than 1'000 contributors were presenting their work.

2.2 Strength of materials vs. fracture mechanics

The problem of general interest in engineering is how a material macroscopically reacts when stresses or strains are applied. With the continuum mechanics the theoretical basis has been given to describe the mechanical behaviour of a material. When the question has to be answered if a material fails or not, load parameters, like the applied stresses or strains, are compared to material parameters, e.g. the tensile strength. The tensile strength indicates the critical stress that, if applied, will bring the material to failure.

However, the situation changes when cracks are present in a material. An example can be found in everyday life: Considering two sheets of paper, an intact one and one with a small crack in it. Much less force will be needed to tear the one with the crack in two pieces. Or in other words, for the same amount of applied stress, a completely different behaviour results: Material failure in one case, no failure in the other. This is a result of the stress situation at the crack tip. Stresses and strains can get singular at the crack tip and therefore these parameters are no longer suited for the description of material behaviour in presence of a crack.

To complement the strength of materials theory in cases where cracks are present, an additional theory – the theory of fracture mechanics – was developed. New parameters were introduced in fracture mechanics such as the stress intensity factor (SIF) K which is a measure of the "magnitude" of the stress singularity at the crack tip (Section 2.3.2) or the energy release rate G which describes how much energy is set free when a crack is extended a certain distance (Section 2.3.1).

In the concept of strength, *mechanical parameters* like stresses or strains are compared to *material parameters* like the tensile or compressive strength or the critical strain, in order to judge if a structure will fail or not. In analogy, in linear elastic fracture mechanics the fracture mechanical parameters K and G are compared to the critical stress intensity factor K_c , the so called fracture toughness, or the critical energy release rate G_c , which is also called the specific fracture energy. Both are material parameters and thus independent of size and shape of the material .

2.3 Linear elastic fracture mechanics

Linear elastic fracture mechanics (LEFM) deals with materials in which non-linear effects are restricted to small areas. In linear elasticity and under uniaxial loading the strain ε is proportional to the applied stress σ and the factor of proportionality is called the elastic modulus or Young's modulus $E = \sigma/\varepsilon$. Linear elasticity is the simplest form of material behaviour and therefore all mechanical theories were first developed for linear elasticity and later on extended to more complex material behaviour, such as elastic-plastic or viscoelastic behaviour.

Throughout this thesis a *quasistatic* fracture process is assumed. The focus is set on the point where the energy available for crack growth starts to exceed the energy required to extend the crack, or in other words the point where a crack starts to self-propagate. The dynamic fracture process that occurs once the required energy for fracture propagation is exceeded is not considered.

2.3.1 Energy release rate and specific fracture energy

Following the terminology of Bazant and Planas (1998), we consider a body of thickness w in which a crack of length a is present. The energy required to extend the crack a certain distance da can be written as the newly cracked area times a crack growth resistance, w_f :

$$dW_F = w da w_f. \quad (2.1)$$

The crack growth resistance w_f can also be associated as the specific fracture energy, where *specific* means an energy per unit area of crack growth.

All the energy supply to the body comes from the external work $dW = P du$, where P is the applied load and u the displacement of the loading point. The external work is stored fully or partly as elastic energy dU . When the only energy-consuming process is fracture, i.e. when no dissipation occurs, the residual energy is the available energy for a crack advance:

$$dW_R = dW - dU. \quad (2.2)$$

Generally, it is more convenient to work with a specific energy G (energy per unit area of crack growth), than directly with dW_R . G is called the energy release rate,

$$G w da = dW_R = dW - dU. \quad (2.3)$$

Accordingly, the criterion for crack propagation is:

$$G \geq w_f. \quad (2.4)$$

Thus, a crack can propagate when the energy release rate G reaches a critical level, the critical energy release rate G_c , which is equal to the specific fracture energy of the material:

$$G_c = w_f. \quad (2.5)$$

In cases in which it is not clear if the conditions for an application of linear elastic fracture mechanics are fulfilled, G_c will be notated as G_f . In such a case, the value of G_f might depend on the specimen size (see also Section 2.4).

The load P and the elastic strain energy U stored in the material are both functions of load point displacement u and cut length a . Thus Equation (2.3) can be written as

$$G w da = P(u, a) du - \left\{ \left[\frac{\partial U(u, a)}{\partial u} \right]_a du + \left[\frac{\partial U(u, a)}{\partial a} \right]_u da \right\}. \quad (2.6)$$

For an equilibrium situation with $da = 0$ one obtains the second Castigliano's theorem:

$$P(u, a) = \left[\frac{\partial U(u, a)}{\partial u} \right]_a. \quad (2.7)$$

For an equilibrium situation in which $du = 0$, Equation (2.6) reduces to

$$G = -\frac{1}{w} \left[\frac{\partial U(u, a)}{\partial a} \right]_u. \quad (2.8)$$

For a given displacement u , the energy release rate is thus the change in the stored elastic strain energy due to a change in the crack length a per specimen width w . By introducing the complementary energy U^* as $U^* = Pu - U$ (which is equal to U in case of a linear elastic behaviour) and substituting U with U^* in Equations (2.6) to (2.8) it can be shown that (Bazant and Planas, 1998, p.26)

$$G = \frac{1}{w} \left[\frac{\partial U^*(P, a)}{\partial a} \right]_P. \quad (2.9)$$

For a given load P , the energy release rate is thus the change in the complementary energy due to a change in the crack length a per specimen width w .

2.3.2 Stress intensity factor and fracture toughness

Depending on how a crack is loaded, three different crack opening modes are defined. The three modes are presented in Figure 2.1. *Mode I* is an opening in tension in the x - y plane. *Mode II* is an in-plane shear opening, where one crack plane slides on the other in x -direction. *Mode III* is an out-of-plane shear opening. The two crack planes slide in opposite z -directions.

When a crack in a homogeneous¹ and isotropic² material is loaded in one of the three modes a stress singularity occurs at the crack tip of the form $1/\sqrt{r}$, where r indicates the distance to the crack tip. A proportionality constant, k , and a function f_{ij} depend on the mode. It is convenient to replace k with $K = k\sqrt{2\pi}$, where K is called the

¹Homogeneous denotes a material whose microstructure does not change in any direction.

²Isotropic denotes a medium whose physical properties are independent of direction.

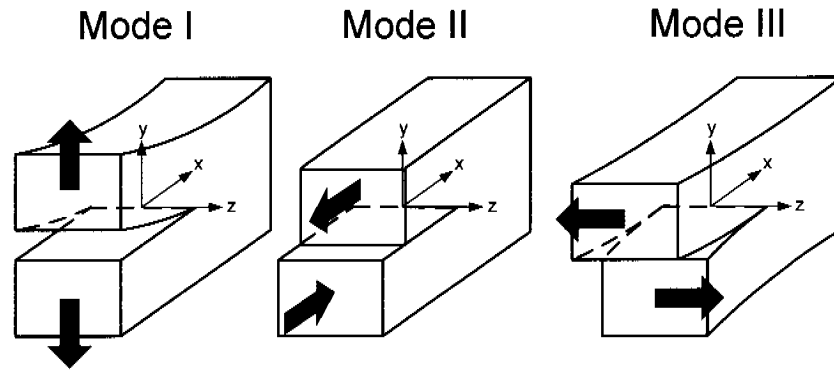


Figure 2.1: Crack opening modes.

stress intensity factor. Therefore, not the stresses themselves, but the magnitude of the singularity K is defined as the parameter which controls crack instability. When a crack is loaded in mode I, the stress field around the crack tip can be written as

$$\sigma_{ij}(r, \phi) = \frac{K_I}{\sqrt{2\pi r}} f_{ij}^I(\phi), \quad (2.10)$$

where r and ϕ denote a polar coordinate system with the origin in the crack tip. The stresses close to the crack tip for an arbitrarily loaded structure are the sum of the three components due to the three different modes (e.g. Bazant and Planas, 1998, p.89):

$$\sigma_{ij} = \frac{1}{\sqrt{2\pi r}} [K_I f_{ij}^I(\phi) + K_{II} f_{ij}^{II}(\phi) + K_{III} f_{ij}^{III}(\phi)]. \quad (2.11)$$

The K -concept is only useful when it is possible to determine K . If the stresses near the crack tip are known, K can be determined according to

$$K_I = \lim_{r \rightarrow 0} \sqrt{2\pi r} \sigma_y(\phi = 0). \quad (2.12)$$

For a few simple geometries a closed-form solution exists. For more complex structures K has to be determined numerically. For a crack in an infinite plate under tension the stress intensity factor is given by

$$K_I = \sigma_N \sqrt{\pi a}, \quad (2.13)$$

where σ_N is the nominal stress and a is the crack length. The nominal stress is defined as the load divided by the original cross section, i.e. the undeformed and uncracked cross section before loading. In a more general formulation the stress intensity factor in mode I can be described as

$$K_I = \sigma_N \sqrt{\pi a} Y(a/D), \quad (2.14)$$

where $Y(a/D)$ is a geometry function depending on the relative cut length a/D , where D is the specimen dimension. Similar expressions can be found for mode II and III.

The fracture toughness in mode I, K_{Ic} , can now be determined according to Equation (2.14) when a specimen is loaded up to failure and the failure stress is recorded σ_f . The measured failure stress σ_f can also be associated as the critical nominal stress. The value of the stress intensity factor at failure K_{If} – the critical stress intensity factor – coincides with the fracture toughness of the material for linear elastic fracture mechanics (LEFM):

$$K_{Ic} = K_{If} = \sigma_f \sqrt{\pi a} Y(a/d). \quad (2.15)$$

The criterion for crack propagation is similar to the criterion for the energy release rate (Equation 2.4):

$$K \geq K_c. \quad (2.16)$$

2.3.3 Energy release rate versus stress intensity factor

Whereas the energy release rate G is a global parameter providing information about the released energy of the whole structure due to a crack advance, the stress intensity factor K is a local parameter providing information about the stress field around the crack tip.

However, a relation exists between the local parameter K and the global parameter G . G can be written as

$$G = \frac{K^2}{E^*}, \quad (2.17)$$

where $K^2 = K_I^2 + K_{II}^2 + K_{III}^2$. For plain strain $E^* = E/(1 - \nu^2)$, where E is the Young's modulus of the material and ν the Poisson's ratio. For plain stress, E^* simplifies to $E^* = E$.

2.4 Non linear extensions

There are only few materials that have a purely linear elastic behaviour. Commonly, the materials are categorized according to their behaviour and one speaks of a linear elastic material or a viscoplastic material for example. But it is important to know that material behaviour might depend on the material size and the loading rate. For example, the failure behaviour of an extremely large concrete structure – such as a concrete dam – can be described by linear elastic fracture mechanics, whereas the failure behaviour of a small concrete element can not. Or the behaviour of a material such as snow can be described linear elastically under rapid loading and ductile (i.e. undergoes plastic deformation) when it is loaded with a low strain rate. The reason for these transitions will be given in the next section.

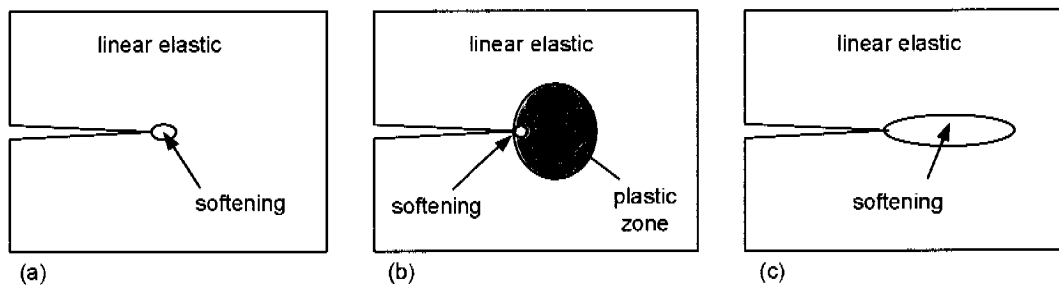


Figure 2.2: Types of fracture process zones: (a) brittle, (b) ductile, (c) quasi-brittle. In the ductile case, the nonlinear zone in the linear elastic material can be divided in a strain softening zone and a plastic deformation zone. Adapted from Bazant and Planas (1998).

2.4.1 Brittle, ductile and quasi-brittle fracture behaviour

The material behaviour in the case of fracture is mainly related to the size of the nonlinear zone that evolves in front of a crack tip. This nonlinear zone consists of a strain softening zone, for which the stress decreases at increasing deformation – the fracture process zone – and is in some cases (ductile materials) surrounded by a zone in which plastic deformation occurs (Bazant and Planas, 1998, p.104). In the following, three types of material behaviour are distinguished, which will be of importance in this work:

Brittle: In a material with a brittle behaviour the process zone is negligibly small compared to the structure size. The entire fracture process takes place almost at one point (Figure 2.2.a). The whole body behaves in good approximation elastically and linear elastic fracture mechanics can be applied without restrictions. Material examples are: glass, brittle ceramics, brittle metals.

Ductile: In ductile materials a zone evolves in which plastic deformation takes place. The nonlinear zone is no longer negligibly small compared to the structure size. The fracture process zone (strain softening) in which the breaking of the material takes place is still small. As it is shown in Figure 2.2.b, the extension of the nonlinear zone normal to the crack is similar to the extension in crack direction. This process can be described by elastic-plastic fracture mechanics. An example of ductile materials are tough alloys.

Quasi-brittle: In quasi-brittle materials the fracture process zone, in which softening takes place, is no longer small compared to the structure size. Its extension in crack direction is much larger than normal to the crack (Figure 2.2.c). Examples for quasi-brittle materials are materials with a granular structure such as concrete, rock, clay or ice (compare Dempsey et al. (1999a,b)). For quasi-brittle materials LEFM is no longer applicable. However, if the nonlinear zone is not very large

compared to the structure size, there are still possibilities to apply LEFM in an equivalent sense, see Section 2.4.3.

As it was mentioned already, the applicability of LEFM depends on the structure size. If for example a very small piece of a brittle metal is tested, it will behave quasi-brittle, because the size of the process zone is a material constant and if the size of the structure gets very small, the process zone is no longer negligible compared to the structure size. On the other hand, if a concrete dam is considered, LEFM can be applied without restrictions because the size of the dam is so large that the finite size of the process zone is negligibly small.

Depending on the strain rate, snow can behave either brittle or ductile. The transition between brittle and ductile behavior can be found at a strain rate of approximately 10^{-4} s^{-1} (Narita, 1980). The processes involved in avalanche release occur within seconds or even a fraction of a second. Therefore, snow can be assumed to behave brittle in avalanche release. But snow does also show strain softening when loaded (McClung, 1987; Schweizer, 1998). This implies that snow should be considered as a quasi-brittle material. This assumption will be justified in Chapter 4 and the question will be answered how large a snow specimen should be to behave brittle.

2.4.2 Fracture process zone

As it was described above, in the presence of a crack, a local non-linear zone evolves in any material due to the extreme stress concentration at the crack-tip. Although in linear elastic fracture mechanics this zone is assumed to be of no extension, in reality, this zone will have a finite size R . For a given load, the size of the process zone depends on the microstructural properties of the material and is therefore a *material constant* and independent of the structural size.

For plastic (ductile) materials R was estimated by Irwin (1958) to be

$$R = \frac{1}{\pi} \left(\frac{K_I}{\sigma_y} \right)^2, \quad (2.18)$$

where σ_y is the plastic yield strength. The maximum length of the fracture process zone R_c is obtained from Equation (2.18) by setting $K_I = K_{Ic}$, i.e. when the load is increased until the structure fails. For steel this equation results in $R_c^{steel} = 0.99 \text{ mm}$ and for aluminium $R_c^{alu} = 0.92 \text{ mm}$ (Bazant and Planas, 1998, p. 108). As long as the length R_c of this non-linear zone remains small compared to the crack length and the characteristic dimensions of the specimen, LEFM can still be applied (e.g. Anderson, 1995, p. 376). In fracture toughness testing of elastic-plastic materials, the applicable standards require R_c at crack instability to be about 8 times smaller than the crack length a or the ligament width $b = h - a$, whichever is smaller (ASTM E 399, 1983):

$$h, a, b > 2.5 \left(\frac{K_{Ic}}{\sigma_y} \right)^2 = 7.9 R_c. \quad (2.19)$$

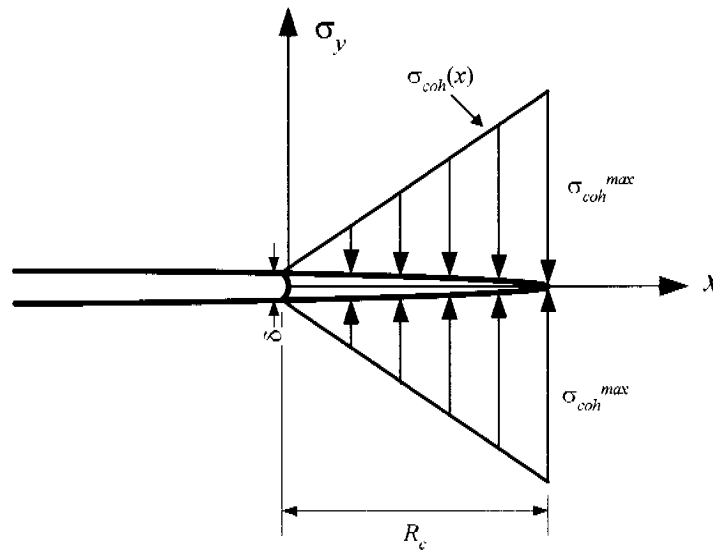


Figure 2.3: Cohesive crack model (Barenblatt, 1962) with a linear distribution of the cohesive stresses $\sigma_{coh}(x)$ acting on the virtual crack-faces. δ denotes the crack tip opening displacement (CTOD) and σ_{coh}^{max} the maximum cohesive stress, which is expected to be about the tensile strength σ_c of the material.

As snow is a non-ductile material at the strain rates applied in our tests, the non-linear zone is restricted to the fracture process zone at the crack-tip. In the fracture process zone the material behavior is characterised by strain softening, i.e. decreasing stresses with increasing deformation. This behavior can be described by Barenblatt's cohesive force model (Barenblatt, 1962). The strain-dependent strength of the material is interpreted as cohesive stresses $\sigma_{coh}(x)$ acting on virtual crack-faces in the range $0 < x < R_c$, i.e. the process zone (Figure 2.3). The distribution of $\sigma_{coh}(x)$ is usually unknown, but for physical reasons it has to be a decreasing function between the maximum at $x = R_c$ and zero at $x = 0$. By replacing the yield strength by the tensile strength of snow σ_c and by assuming, for the sake of simplicity, $R_c \ll a$ and a linear behaviour of the cohesive stress with x , this model yields (Schindler, 1996):

$$R_c = \frac{9\pi}{32} \left(\frac{K_{Ic}}{\sigma_c} \right)^2. \quad (2.20)$$

This is about three times the value given by Equation 2.18. Moreover, if the condition $R_c \ll a$ is not fulfilled, then R_c becomes dependent on the crack length and specimen geometry. Beyond LEFM, even Equation 2.20 can considerably underestimate the actual length of the non-linear zone. Concerning the size requirement which has to be fulfilled for an application of LEFM, there is only little experience on non-ductile materials in general and snow in particular. A simplified application of Barenblatt's model to a deeply cracked beam in bending (Schindler, 1996) indicates that the corresponding requirement should be at least as restrictive as the one given by ASTM E399 for elastic-plastic

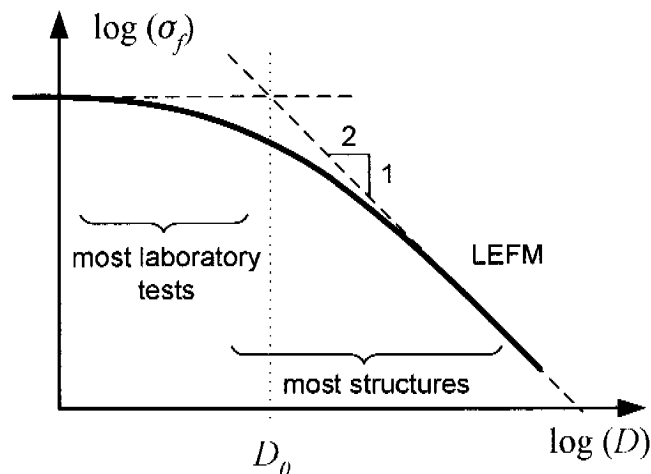


Figure 2.4: Fracture mechanical size effect on the strength of a material. Dependence of the nominal strength σ_N on the structure size D . According to Bazant and Planas (1998).

materials. For snow R_c was found to be in the order of several centimeters (Section 4.1.6).

2.4.3 Consequences of quasi-brittle behavior

If LEFM does not apply, the fracture process is no longer governed by the stress intensity factors only. This means that the critical stress intensity factor K_f , determined in an experiment, does not represent the actual fracture toughness K_c of the material, but an apparent fracture toughness that depends on the geometry and the size of the specimen used in the experiment. The difference between the two parameters is, that K_c is a material property, while K_f is not. If the size criterion for LEFM, Equation (2.19), is not fulfilled, then

$$K_f \neq K_c. \quad (2.21)$$

In this case, K_f is smaller than K_c and thus the measured K_f values have to be corrected, either to a sample size where LEFM applies to get the real K_{fc} or to the size of the problem which has to be solved to get a size corrected K_f value. Before a correction of the measured K_f values is possible, a scaling law has to be found.

Scaling law

It is known that fracture processes governed by nominal stresses or plastic collapse are scalable, whereas those governed by crack instability are not (Bazant and Planas, 1998). The reason is that for a larger structure, more energy is released at the crack

front by the same crack extension, Δa . Accordingly, there is no size effect in nominal strength σ_f for specimens which are smaller than a certain size. For large sizes a pure brittle behaviour is dominant and structures fail at a fixed stress intensity factor, which depends on the absolute crack length. This general behaviour is schematically shown in Figure 2.4 (Bazant and Planas, 1998), using a general size parameter D . Based on experimental data of tensile fracture, Bazant and Planas (1998) proposed the following general scaling law for the nominal strength

$$\sigma_f = \frac{Q}{\sqrt{1 + D/D_0}}, \quad (2.22)$$

where Q is a constant of the dimensions N/m^2 , and D_0 a characteristic size. In Figure 2.4, D_0 is the point where the line for linear elastic behaviour intersects with the horizontal line for plastic collapse. However, Equation (2.22) can only serve to predict the size effect in cases of short cracks or geometrically similar crack systems. For our snow experiments, the specimen sizes D were between 10 cm and 30 cm. D_0 was found to be around 30 cm, thus a ratio D/D_0 of about 1 results (Section 4.1.5).

Equivalent fracture toughness

According to Bazant and Planas (1998) it is possible to experimentally obtain an equivalent fracture toughness K_{Ic}^e , which is an estimate of fracture toughness K_{Ic} . By rearranging Equation (2.22) a linear dependence of the specimen size D is obtained:

$$\left(\frac{1}{\sigma_f}\right)^2 = c_1 + c_2 D, \quad (2.23)$$

with $c_2 = 1/(D_0 Q^2)$ and $c_1 = 1/Q^2$. D as well as σ_f are determined in experiments. If these data are then plotted as $(1/\sigma_f)^2$ versus D , D_0 and Q can be estimated from slope and intercept of a linear regression by

$$D_0 = \frac{c_1}{c_2} \quad (2.24)$$

and

$$Q = \frac{1}{\sqrt{c_1}}. \quad (2.25)$$

By substituting Equations (2.22), (2.24) and (2.25) into Equation (2.14), K_{If} can be written as

$$K_{If} = \frac{\sqrt{\pi a}}{\sqrt{c_1 + c_2 D}} Y\left(\frac{a}{D}\right). \quad (2.26)$$

For large D , c_1 can be neglected in Equation 2.26. According to Figure 2.4 the specimen behaviour is linear elastic for large D , i.e. K_{If} tends to K_{Ic}^e , and Equation (2.26) simplifies to

$$K_{Ic}^e = \sqrt{\frac{\pi}{c_2} \left(\frac{a}{D}\right)} Y\left(\frac{a}{D}\right) \quad D \gg D_0. \quad (2.27)$$

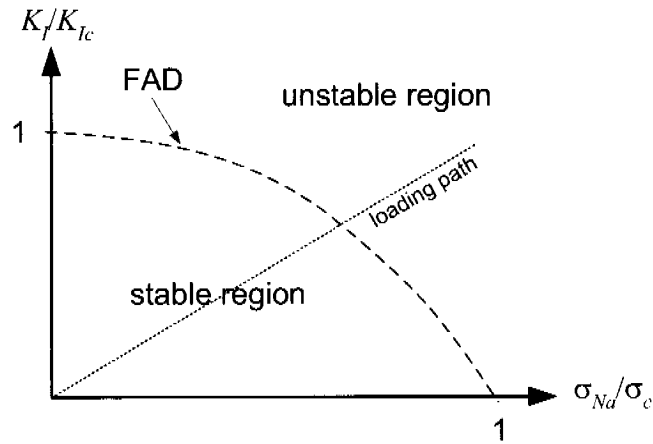


Figure 2.5: Theoretical failure assessment diagram (FAD) for brittle material behaviour.

If Equation (2.26) is combined with Equation (2.27), a correction of the measured K_{If} values to size independent equivalent fracture toughness values, K_{Ic}^e , is possible, as long as the characteristic size D_0 is known

$$K_{Ic}^e = \sqrt{1 + \frac{D_0}{D}} K_{If}. \quad (2.28)$$

The failure assessment diagram

Beyond LEFM, the fracture process is governed by the interaction of the stress intensity factors K_I and the effective stresses σ_{Na} acting in the region of the crack tip. A practical tool to cope with this complex situation of an interaction of local and global stresses is the so-called failure assessment diagram (FAD), which represents the interaction as a failure line in the plane $K_I - \sigma_{Na}$, as schematically shown in Figure 5 (British Energy Generation Ltd., 2001). FADs are often used to assess the stability of a cracked structural component in elastic-plastic fracture mechanics. The shape of the FAD depends on the material of the tested structure. Reversing the idea, the FAD might serve to estimate fracture toughness K_{Ic} from the apparent fracture toughness values K_{If} determined with specimens that did not fulfil the size requirement (Figure 2.5). In British Energy Generation Ltd. (2001) a universal FAD was given as

$$K_r = \frac{0.3 + 0.7 \exp(-0.6 L_r^6)}{\sqrt{1 + 0.5 L_r^2}}. \quad (2.29)$$

In the terminology of the present paper, $K_r = K_{If}/K_{Ic}$ and $L_r = \sigma_{Na}/\sigma_c$.

2.5 Failure of interfaces

There is an important difference between fracture behaviour of homogeneous materials and layered materials, i.e. materials that consist of two or more layers with different material properties. Whereas the crack propagation in a homogeneous material is normally not restricted to a defined direction, in layered materials cracks propagate in general along the interfaces between two layers. Due to this restriction, considerably different loading situations can occur. It is known that mode II experiments in homogeneous materials are difficult to perform, because cracks tend to change direction, resulting in a pure mode I situation (Anderson, 1995, p. 91). On the other hand, mode II failures are particularly a problem in layered materials (Hutchinson and Suo, 1992).

Interfacial fracture mechanics is of importance in many research areas dealing with modern layered materials such as laminates, fibers and composites. It has also been applied to study natural processes, for example, the icing of electrical transmission cables leading to ice/metal interfaces (Wei et al., 1996). Since snow is also a layered material and the layering is a precondition for slab avalanche release, an application of interfacial fracture mechanics seems self-evident and was proposed by Schweizer and Camponovo (2001).

2.5.1 The complex stress intensity factor

The phase angle of loading Ψ is a measure of the relative shear to tension loading. $\Psi = 0$ means pure tension and $\Psi = +\pi/2$ means pure shear. One important feature of bimaterial interface cracks is that Ψ is often non-zero even when the external loading is normal to the interface plane (Rice, 1988), i.e. even when the external loading is in pure tension or shear a mode-mixity can exist.

As a result, the crack tip field of an interfacial crack between two dissimilar solids has not the same shape as in a homogeneous material. It can be described with the complex interface stress intensity factor $K = K_1 + i K_2$. In this formulation, K_1 describes not only tensile stresses but also shear stresses, the same holds for K_2 , i.e. in a bimaterial crack the two modes are coupled and can not be easily separated. The normal and shear stresses of the singular field acting on the interface a distance r ahead of the crack tip are given by Rice (1988):

$$\sigma_{22} + i\sigma_{12} = \frac{K}{\sqrt{2\pi r}} r^{i\xi}. \quad (2.30)$$

The bimaterial constant ξ is defined as:

$$\xi = \frac{1}{2\pi} \ln \left(\frac{1-\beta}{1+\beta} \right), \quad (2.31)$$

where $\beta(\nu_1, \nu_2, \mu_1, \mu_2)$ is a function of the shear modulus and the Poisson's ratio of the two components (e.g. Erdogan and Sih, 1990). If $\xi = 0$ the complex stress intensity

factors K_1 and K_2 reduce to the corresponding stress intensity factors K_I and K_{II} . The energy release rate G is defined as (Malyshev and Salganik, 1965):

$$G = \frac{(1 - \beta^2)}{2} \left(\frac{1}{E_1} + \frac{1}{E_2} \right) |K|^2, \quad (2.32)$$

where $|K|^2 = K_1^2 + K_2^2$ and E_1 and E_2 are the elastic moduli of the two materials. In the following, we will focus on the energy release rate G of an interface crack rather than on the complex stress intensity factor K . As it is shown in Equation 2.32, from G the absolute value $|K|$ can be derived, but not the components K_1 and K_2 . In other words, the energy release rate contains no information about the mode I and II mixing. But as we will be primarily interested in whether a crack propagates or not, this additional information is not needed and would not be worth the much bigger effort.

2.5.2 Energy release rate for an interface crack

Due to the complexity of the interface problem, there are only a few analytical solutions for special geometries available. It is common, not only in interfacial fracture mechanics but in fracture mechanics in general, to determine fracture mechanical parameters numerically with the aid of a finite element model.

As an example for an analytical solution, the one by Suo and Hutchinson (1990), (Hutchinson and Suo, 1992) will be given. They described an analytical solution for a general interface crack problem. Their aim was to analyse interface cracks between thin films and substrates under fairly general loading conditions (Figure 2.6). Their model consists of two layers. The solution for the energy release rate G in plain strain is given by:

$$G = \frac{1}{2E_1} \left(\frac{P_1^2}{h} + 12 \frac{M_1^2}{h^3} \right) + \frac{1}{2E_2} \left(\frac{P_2^2}{H} + 12 \frac{M_2^2}{H^3} - \frac{P_3^2}{Ah} - \frac{M_3^2}{Th^3} \right), \quad (2.33)$$

where P_i are the applied loads per specimen width and M_i the applied moments per specimen width ($i = 1, 2, 3$). E_1 and E_2 are the elastic moduli of the two components and h, H their heights. $A = 1/\eta + \Sigma$ with $\Sigma = E_1/E_2$ and $\eta = h/H$. I is given as:

$$I = \Sigma \left[\left(\Delta - \frac{1}{\eta} \right)^2 - \left(\Delta - \frac{1}{\eta} \right) + \frac{1}{3} \right] + \frac{\Delta}{\eta} \left(\Delta - \frac{1}{\eta} \right) + \frac{1}{3\eta^3}, \quad (2.34)$$

with

$$\Delta = \frac{1 + 2\Sigma\eta + \Sigma\eta^2}{2\eta(1 + \Sigma\eta)}. \quad (2.35)$$

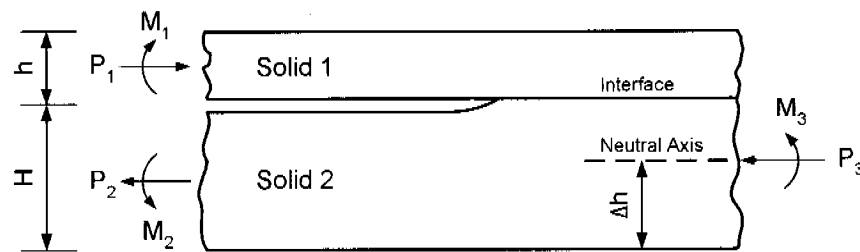


Figure 2.6: A bilayer material with a half-plane interface crack. After Hutchinson and Suo (1992).

2.6 Application of fracture mechanical concepts to snow

2.6.1 Experimental studies

Fracture mechanical experiments with snow were only performed in the last six years. Thereby, the focus was set on the determination of the fracture toughness of snow in mode I and mode II. However, most experiments were done in mode I because the experimental setup for a mode I test is simpler than for one in mode II, and their exist anyway only few tests that can be adapted to snow, due to its fragile nature. In the following, the contributions are listed in chronological order.

Kirchner et al. (2000) were the first to measure a critical stress intensity factor in mode I for snow. They performed cantilever experiments in the field and evaluated their data by applying fracture mechanical theories of foams by Gibson and Ashby (1997). They found a relation of

$$K_{Ic} = A (\rho_{snow} / \rho_{ice})^B, \quad (2.36)$$

with $A = 7.84 \text{ kPa} \sqrt{m}$ and $B = 2.3$. They suggested that with these extraordinarily low values of fracture toughness, snow would be one of the most brittle materials known to man. The data was recorded at temperatures near the melting point and for snow types that are not known in detail.

Kirchner et al. (2002a,b) used cantilever beam tests to determine fracture toughness in tension and shear. Notched cantilever beams of snow ($50 \text{ cm} \times 20 \text{ cm} \times 10 \text{ cm}$) were broken under their own weight. This time, all experiments were performed in a cold laboratory at SLF. A linear elastic approach was used to determine the critical stress intensity factor K_{Ic} which was directly associated with the fracture toughness K_{Ic} . They concluded that snow fracture toughness in shear is about the same as in tension.

Faillettaz et al. (2002) performed the same field experiments as Kirchner et al. (2000) had done and found fracture toughness values of the same order. They found that the fracture toughness values depend on the cantilever length and suggested that this could

be a result of a fractal branching pattern of the crack.

Schweizer et al. (2004) measured in the cold laboratory at a temperature of -10°C and found for Equation (2.36) values for A between $13.0 \text{ kPa} \sqrt{\text{m}}$ and $21.6 \text{ kPa} \sqrt{\text{m}}$, and for B between 1.9 and 2.1, depending on snow type. They proposed that this snow type dependence can be taken into account by including a microstructural parameter d_{max} , characterizing the grain size,

$$K_{Ic} = \frac{C}{\sqrt{d_{max}}} \left(\frac{\rho}{\rho_{ice}} \right)^{1.9}, \quad (2.37)$$

where d_{max} is the grain size and $C = 0.35 \text{ kPa} \cdot \text{m}$ is a constant. This lead to $K_{Ic} = 600 - 900 \text{ Pa} \sqrt{\text{m}}$ for a typical slab density of $\rho = 180 \text{ kg/m}^3$. Based on some experiments in shear (Kirchner et al., 2002a), they suggested that fracture toughness in shear is slightly smaller than fracture toughness in tension (Schweizer et al., 2004). Schweizer et al. (2004) showed that fracture toughness decreases with increasing temperature until it reaches a minimum between -10°C and -5°C . This means that fractures can propagate more easily with increasing snow temperature. However, for temperatures above this minimum the fracture toughness increases again towards 0°C .

So far, all attempts to determine snow fracture toughness in mode II were performed with *homogeneous* snow samples. However, as it was mentioned in Section 2.5, mode II experiments in homogeneous materials are difficult to perform and the cracks tend to change direction, resulting in a pure mode I situation. Therefore, it is essential to test *layered* samples in mode II.

McClung (2005b) estimated the shear fracture toughness, K_{IIc} from slab avalanche data to be between 0.02 and $13 \text{ kPa} \sqrt{\text{m}}$.

Most recently, Gauthier and Jamieson (2006) proposed a drop hammer test for layered snow beams on the slope. Thereby, they used a similar geometry to our field test. But instead of notching the isolated snow beams they applied a drop load at the upper end of the snow beam and assessed if they could trigger the propagation of a fracture in the weak layer or not.

2.6.2 A model for shear fracture propagation

McClung (1979, 1981) proposed a model for a shear fracture propagation in a thin, planar weak layer underneath a cohesive, strong slab. The model originates from Palmer and Rice (1973), who introduced the idea of a shear band in overconsolidated clay. Bazant et al. (2003) based their formulation of a size effect law for fracture triggering in dry snow slabs on this model.

The slope model consists of three layers including a rigid basal layer overlaid by an elastically behaving slab with height H (measured slope normal), and in between a weak layer (Figure 2.7). The slab is inclined by an angle φ . The weak layer is damaged on a

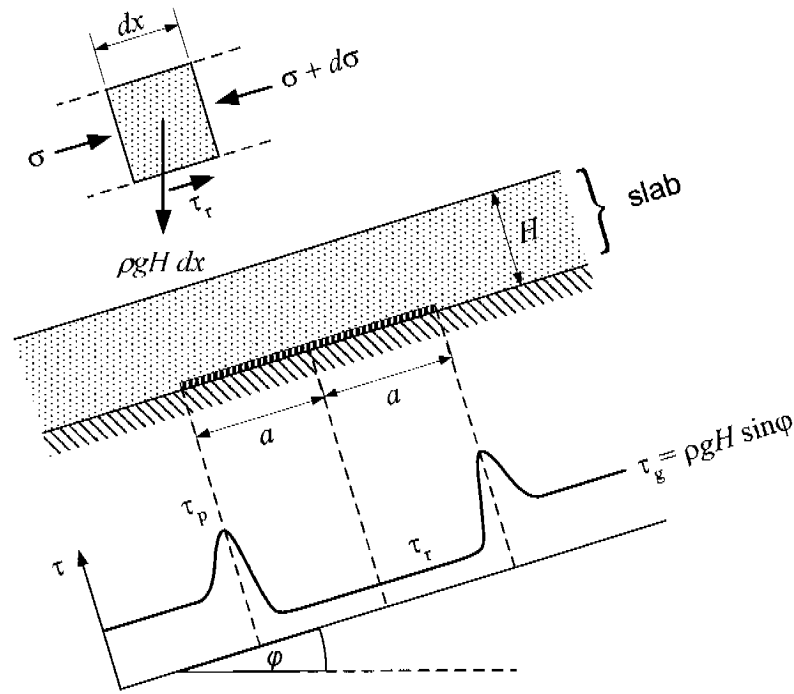


Figure 2.7: Geometry of a two-dimensional snow slab after (Bazant et al., 2003). $2a$ is the cohesive crack. Forces acting on an element of slab (top left). Typical shear stress distribution (bottom).

length $2a$. The Young's modulus of the slab E as well as the density of the slab ρ are considered as uniform over H . A crack is propagating symmetrically up and downwards along the weak layer.

The equilibrium condition for a unit element dx of the slab leads to (Figure 2.7)

$$(\sigma + d\sigma) = \sigma - \frac{(dx H \rho)g \sin(\varphi)}{H} + \tau_r, \quad (2.38)$$

where τ_r is the residual shear stress due to friction. As a first approximation no residual shear stress is assumed, $\tau_r = 0$. When integrating Equation (2.38)

$$\sigma = -\rho g x \sin(\varphi) \quad (2.39)$$

results. If $2a \gg H$ the transition zone of τ can be neglected. Calculating the complementary strain energy of one half of the sliding layer leads to

$$U^* = \int_0^a \frac{1}{2} \sigma \varepsilon H w dx = \int_0^a \frac{\sigma^2}{2E} H w dx = [-\rho g \sin(\varphi)]^2 \frac{H a^3 w}{6E} = \frac{\tau_g^2 a^3 w}{6EH}, \quad (2.40)$$

where E is the Young's modulus of the snow layer, w the lateral width and τ_g is the shear stress that is required to support the weight of the slab if no crack is present (no

tensile forces are acting):

$$\tau_g = \rho g H \sin(\varphi). \quad (2.41)$$

Bazant et al. (2003) state that the one dimensional solution of Equation (2.40) might even be acceptable as long as $a > H$. Furthermore, they point out that situations in which $a \ll H$ are of no practical interest, because small imperfections always exist in an alpine snowpack and thus a snow layer would never be stable on a slope.

The energy release rate, G , can be calculated according to Equation (2.9) and (2.40)

$$G(a) = \frac{1}{w} \frac{\partial U^*}{\partial a} = \frac{\tau_g^2 a^2}{2EH}. \quad (2.42)$$

Since we have set $\tau_r = 0$, the resulting energy release rate, G , is an upper boundary for the true energy release rate in case a residual friction would be present.

2.6.3 A model for a slope normal displacement of the slab

Heierli and Zaiser (2006) proposed an analytical model on the gravitational collapse of horizontal stratifications. In contrast to ordinary fracture dynamics, they assume an initially relaxed slab that quits its metastable equilibrium once the weak layer underneath the slab locally collapses. In this model, the energy functional associated with a localized collapse of the weak layer is calculated as the sum of the elastic energy V_e , the gravitational energy of the slab V_g and the energy that is required to fracture the weak layer over a given length, V_f :

$$V(u) = V_e(u) + V_g(u) + V_f(u), \quad (2.43)$$

where u is the displacement in direction normal to the slab. Explicitly, the total energy functional is (Heierli and Zaiser, 2006):

$$V(u) = \int \left\{ \frac{\mathfrak{D}}{2} \left(\frac{d^2 u(x)}{dx^2} \right)^2 + \rho H g u(x) + w_f \theta(-u(x)) \right\} dx, \quad (2.44)$$

where ρ is the density of the slab and H the slab thickness, g is the gravitational acceleration, \mathfrak{D} the flexural rigidity of the slab and θ the Heaviside step function ($\theta(u) = 1, u > 0$ and 0 else). The collapse has to be divided in three phases. Bending of the slab due to a localized collapse without contact to the slab underneath the weak layer, followed by a contact to this layer in one point, followed by a contact over a finite interval. However, they showed that only the first phase is relevant for fracture propagation because the first derivative of the total energy (Equation 2.44) becomes negative before the slab touches the substratum (Figure 2.8). The half length of a critical crack r_c can be evaluated in terms of the material properties of the overlaying slab and the fracture energy of the weak layer w_f :

$$r_c = \left(\frac{18\mathfrak{D}}{(\rho H g)^2} w_f \right)^{1/4}. \quad (2.45)$$

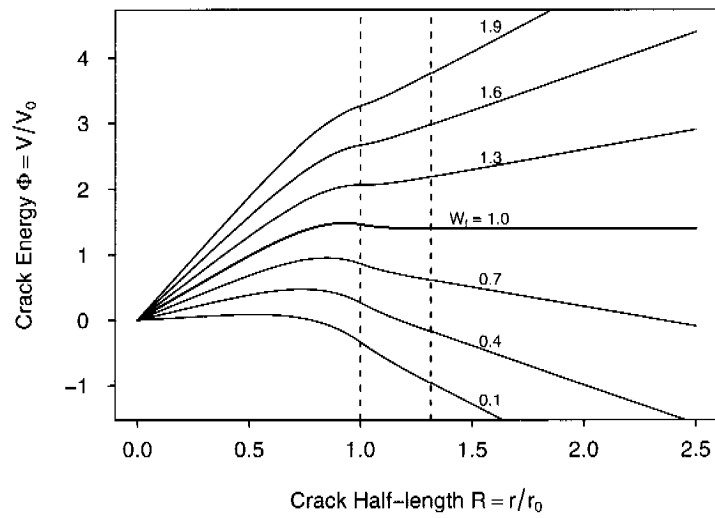


Figure 2.8: Scaled crack energy in function of scaled crack extension in dimensionless units (Heierli and Zaiser, 2006). Different weak layer fracture energies are displayed. A crack gets critical when the energy passes a maximum. (Source: Geophysical Research Letters, 33, L06501, 2006)

The flexural rigidity \mathfrak{D} can be evaluated using the expression for a uniform slab

$$\mathfrak{D} = \frac{EH^3}{12(1 - \nu^2)}. \quad (2.46)$$

Seite Leer /
Blank leaf

Methods

3.1 Standard measurement techniques for snow characterization

In comparison to most other materials, the microstructural and mechanical properties of snow are highly variable. Therefore, it is essential to characterize the microstructure of snow whenever experiments are performed. Standard measurement techniques for snow characterization have been developed in the past, which have now been successfully applied in snow science for many years. This section gives an overview of the techniques and procedures that were applied during the experimental work.

Snow classification: Each time when snow samples were collected in the field, the stratigraphy of the snow cover was characterized in stratigraphic snow cover profiles. Therefore, a snow pit was dug and the snow was analysed regarding its horizontal layering, the snow type, temperature and density. A snow layer is characterized by a given *snow type*. The separation of layers is based on visual and tactile variations in the snow type. The snow type includes the classification of three snow properties: the grain shape, the grain size and the snow hardness index. They are classified according to the International Classification of Seasonal Snow on the Ground (ICSSG) (Colbeck et al., 1990). The snow hardness index is a subjective classification with six classes of penetration resistance: Fist (F), Four-fingers (4F), One-finger (1F), Pencil (P), Knife (K) and Ice (I). In addition to the identification of the layering a temperature profile was recorded from the snow surface to the ground, the densities of the different layers were measured (see next item) and occasionally the ram hardness was measured. See Appendix B for examples.

Density measurements: The density of a snow layer or a snow specimen is measured by cutting out small samples with an aluminium cylinder or alternatively with a

small aluminium box and weighing it on a scale. A standard volume is 100 cm³ but there are also larger cylinders in use. It is common to average two to four measurements to reduce the effect of measurement errors.

Stability tests: To identify weak layers suited for sampling, stability tests were made. We used the compression test in which the top of an isolated column of snow (30 cm × 30 cm) is loaded by tapping on a shovel (Jamieson, 1999). The first ten taps are done with the fingertips moving the hand from the wrist. The next ten taps are done by moving the forearm from the elbow. Finally, ten taps are done moving the arm from the shoulder. Depending on the number of taps the ease of triggering can be estimated as: 0 = very easy, 1-10 = easy, 11-20 = moderate, 21-30 = hard.

Shear frame test: To measure the shear strength, the shear frame test was used. A steel frame with an area of 0.025 m² was placed about half a centimeter above a weak layer, then the frame was pulled with a force gauge smoothly and quickly, resulting in a planar failure of the weak layer (Jamieson and Johnston, 2001). Due to the scatter of the test results it is common to average 8 to 12 tests to get a reliable result.

Snow micro-penetrometer: The SnowMicroPen (SMP) is a high-resolution constant speed penetrometer. It records the penetration resistance of a small cone (diameter: 4 mm, cone angle 60°) which is pushed through the sample perpendicular to the layering of the snow cover or the snow specimen (Schneebeli and Johnson, 1998; Schneebeli et al., 1999). Due to the high resolution of the SMP, it is possible to resolve details in layers that are considered as homogeneous. The SMP resistance profile is especially qualified to assess the detailed layering of a snow specimen and allows to derive additional parameters, e.g. an index for the Young's modulus (Johnson and Schneebeli, 1999) as will be discussed in Section 3.4.

Sample characterization: Small snow samples of interesting snow layers, especially of weak layers were occasionally collected. The samples were cut out of the snow with small containers of the dimension 5 cm × 5 cm × 5 cm. Then, liquid and dyed black Diethyl-phthalate was added which filled up the pores in the snow sample. After freezing, the cube was sliced in a microtome and the surface was successively photographed with a digital camera. Finally, the image was binarized to distinguish between ice and pore-space (Good, 1987).

A further standard test in materials science is to measure the tensile and compressive strength of a material. However, no standard procedures exist to measure the tensile or the compressive strength of snow, up to now.

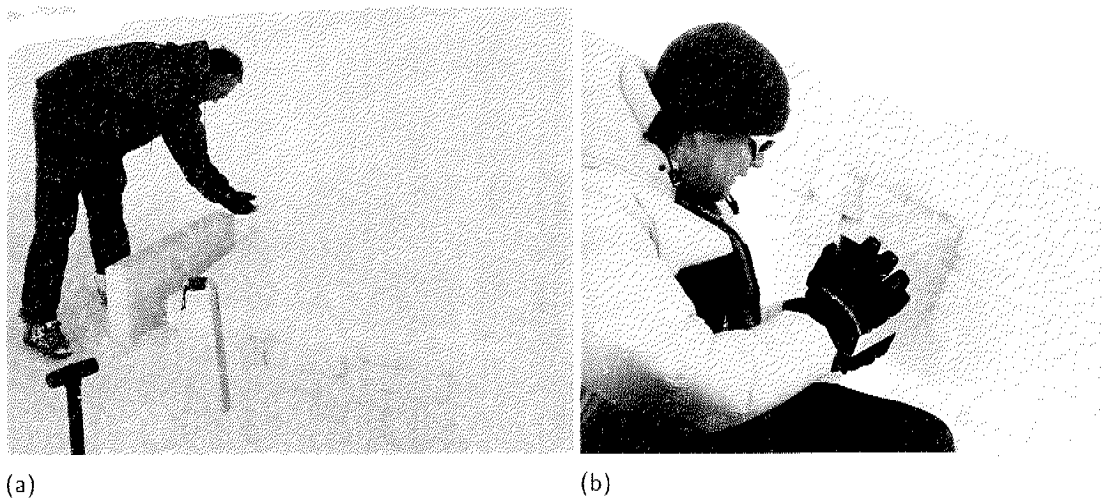


Figure 3.1: Homogeneous snow samples were collected by pushing the aluminium cases with the height parallel to the layering into a thick layer of the snow cover (a), while for layered samples the cases were used upright (b) in order to include more than one layer.

3.2 Laboratory tests

About 80% of all experiments were performed in the cold laboratory, the rest was performed in the field. For all laboratory tests the snow samples had to be collected in the field and transported to the laboratory.

3.2.1 Sample collection

All snow samples were collected in the field. They were either collected close to the building of the Swiss Federal Institute for Snow and Avalanche Research in Davos, Switzerland, at an altitude of 1562 m a.s.l., or close to the old institute building on the Weissfluhjoch, Davos, at 2668 m a.s.l. At both places a cold laboratory is available with a temperature range of -20°C to 0°C . The samples had to be carried to the cold laboratory one by one in order not to destroy the snow structure. Especially for layered snow samples the transport was delicate. Therefore, the collecting area for snow samples was restricted to a radius of a few hundred meters around the two institute buildings. After transport, the samples were stored at a temperature of -10°C for a maximum of two days before testing. The experiments were performed at a cold room temperature of -10°C , and occasionally at -15°C .

The specimen were cut out of the natural snowpack with beam-shaped aluminium cases. Four different sizes of aluminium cases were used to collect samples. The largest was close to the limit of what could be handled in the field and transported to the laboratory

Table 3.1: Snow specimen dimensions. The standard specimen size is marked in bold.

Height h (cm)	Length l (cm)	Width w (cm)
8	20	10
13	31	10
20	50	10
32	80	10

without destroying the natural snow structure. The other sizes were chosen such that a size range of 1:4 was achieved. The thickness w was the same for all specimen sizes – this is called "2D similarity", according to Bazant and Planas (1998, p.458) – in order to avoid a possible thickness effect. The dimensions are given in Table 3.1. In the standard size, nineteen cases were available, in all other sizes five. The standard size was already used by Kirchner et al. (2002a,b) and Schweizer et al. (2004).

For the laboratory tests two kind of samples were used: *homogeneous* snow samples consisting of only one layer (:= monolayer) and *layered* snow samples consisting of two or more layers (:= multilayer). Snow samples were defined to be homogeneous when no visible layering was present, i.e. when they consisted of one snow type. Homogeneous snow samples were taken out of the snow cover by selecting a thick enough snow layer ($w > 12$ cm) in which the whole aluminium case could be placed without any contact to adjacent layers. Suitable layers were previously defined in a snow profile. The aluminium cases were pushed into the snow cover horizontally with the height of the case parallel to the layering (Figure 3.1a), but later on tested upright. This was done, because even within one layer of the snow cover the density tends to slightly increase with increasing snow depth. By testing the specimens normal to the layering of the snow cover an influence of this density increase or a slight undiscovered layering was minimized. Schweizer et al. (2004) showed that tests are influenced by a layering parallel to the test direction. For the collection of layered snow samples the aluminium cases were pushed into the snow cover upright with the height of the case vertical to the layering (Figure 3.1b), so that the weak layer was caught in the middle of the case, resulting in snow specimens consisting of two homogeneous snow layers separated by a weak layer. Weak layers suited for sampling were identified previous to collection by applying compression tests.

3.2.2 Three-point bending test

The three-point bending test (3PB-test) is a common test configuration in material science to determine fracture toughness in mode I (e.g. Tada et al., 2000, p.58). A beam shaped specimen is notched on one side with a cut of a given depth (normally between 0.1 and 0.5 times the beam height), placed on two supportors and loaded in

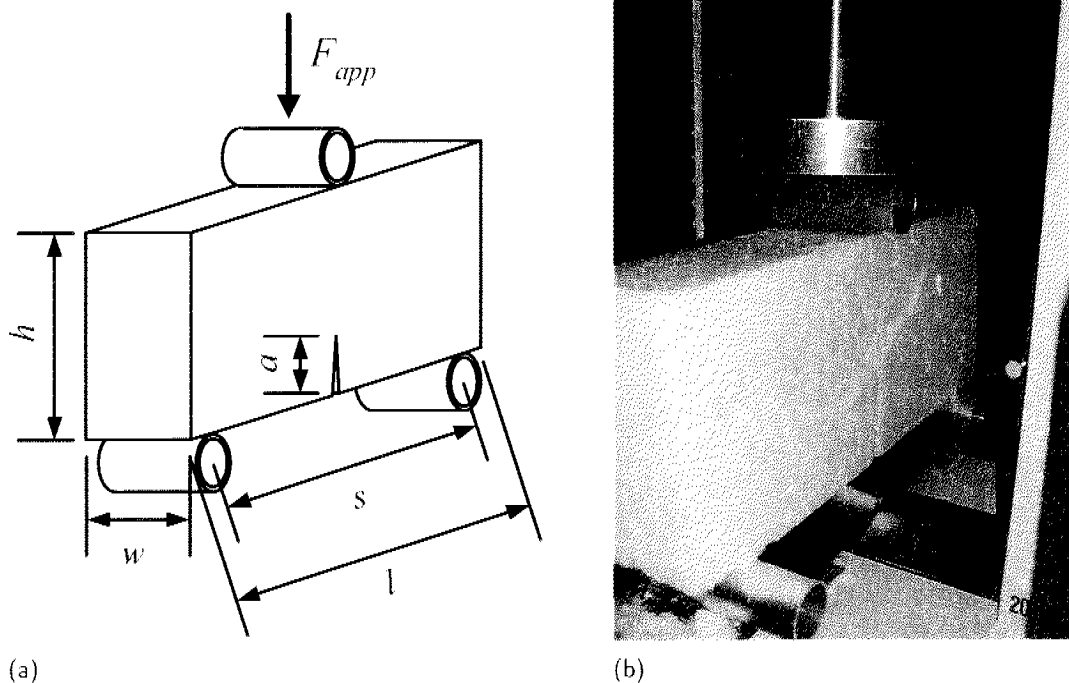


Figure 3.2: (a) Schematic diagram of the three-point bending test setup . (b) Snow specimen in place before testing. The aluminium plates on top of the cylindrical supports are missing in this image.

the middle of the opposite side with an increasing force until the specimen fails.

All 3PB-tests were performed with a standard material testing machine (ERICHSEN-Universalprüfmaschine 490). The machine has an upper force limit of 20 kN. After a first winter of testing (winter 2003/2004) it turned out that the force range was unnecessarily high for experiments with snow. In the tests, forces of a maximum of 200 N were achieved. On the other hand the force resolution was much too low. Therefore, the machine was upgraded during summer 2004 with a new sensor head including a new force sensor (Figure 3.3). Additionally, an improved data processing software was written, based on LabView. With the new force sensor the time resolution could be improved from 72 ms to 4 ms with a sampling rate of 2000 Hz where every 8 samples were averaged to decrease signal noise, resulting in an effective sampling rate of 250 Hz. The force sensitivity could be improved from 1 N to less than 15 mN.

The standard 3PB-test setup needed two slight modifications to be applicable to snow specimens. It was not possible to place soft snow on sharp triangular supporters without a considerable penetration of the supporters into the fragile snow specimen. Instead, aluminium cylinders were used to increase the contact area and to prevent local snow deformation at the loading points (Figure 3.2). The aluminium cylinders had a diameter of 6 cm. The diameter of the cylinders was expected to have only a minor influence on the test results. The load was applied in displacement control at a constant rate

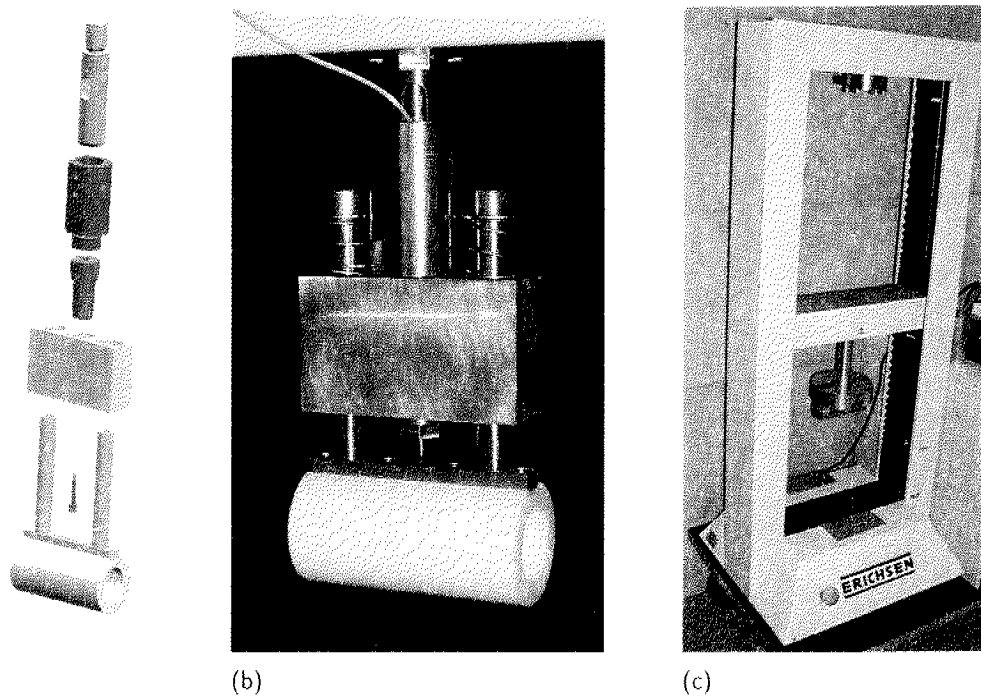


Figure 3.3: (a) Design drawing of the new sensor head including the more accurate force sensor (thin black bolt). (b) Image of the new sensor head. (c) Image of the ERICHSEN-Universalprüfmaschine 490 (height: ~ 1.5 m including the old sensor head).

of 200 mm/min through another cylinder with a diameter of 5 cm. The velocity was chosen high in order to cause a brittle fracture and to avoid viscous effects. As a second modification, small aluminium plates were placed between the cylinders and the specimen to prevent friction between the supporters and the specimen while testing.

The critical force, F_f , that had to be applied to break the specimens, ranged up to 200 N, depending on beam size and snow density. Due to this rather low force, the weight of the beam had to be taken into account in calculating the applied stress and stress intensity factor. The weight of a typical sample of a density of 250 kg/m^3 is about 25 N.

The bending moment in the center of a beam due to an applied force F per specimen width w is

$$M_F = \frac{F's}{4w}, \quad (3.1)$$

where s is the span, i.e. the distance between the two supporters. The bending moment in the center of the beam per specimen width due to the body weight can be written as

$$M_G = \frac{h\rho g}{8} [s^2 - (l - s)^2], \quad (3.2)$$

where ρ is the density of the specimen, h its height and l its length. g is the gravitational

acceleration. According to Tada et al. (2000) the nominal stress is given as

$$\sigma_N = \frac{6}{h^2} (M_F + M_G). \quad (3.3)$$

The nominal stress is defined as the load divided by the original cross section, i.e. the undeformed and uncracked cross section before loading. The effective stress, σ_{Na} , i.e. the load divided by the remaining cross section, will be defined in Section 4.1.7. The critical stress intensity factor or the apparent fracture toughness K_{If} can be calculated according to Equation (2.15) as a combination of the 3PB-solution and the pure bending case given by Tada et al. (2000):

$$K_{If} = \frac{6}{h^2} \sqrt{\pi a} [0.95 M_{F_j} Y_1(a/h) + M_G Y_2(a/h)]. \quad (3.4)$$

Here, M_{F_j} is the critical bending moment, i.e. the force at failure, F_j , has to be inserted in Equation (3.1). The functions $Y_1(a/h)$ and $Y_2(a/h)$ can be found in Tada et al. (2000):

$$Y_1(a/h) = \frac{1}{\sqrt{\pi}} \cdot \frac{1.99 - (a/h) [1 - (a/h)] [2.15 - 3.93(a/h) + 2.7(a/h)^2]}{[1 + 2(a/h)] [1 - (a/h)]^{3/2}}, \quad (3.5)$$

$$Y_2(a/h) = 1.122 - 1.40(a/h) + 7.33(a/h)^2 - 13.08(a/h)^3 + 14.0(a/h)^4. \quad (3.6)$$

Y_1 is valid for a span to height ratio of $s/h = 4$. Since in our experiments the specimens have a ratio of $s/h \approx 2$ a correction factor was necessary. According to Schindler (personal communication) a factor of 0.95 had been found in a numerical computation to account for the difference in the ratio s/h . For our 3PB-experiments the part due to the moment M_G in Equation (3.4), is about 60% of the part due to the force at failure ($F_j s/4w$).

3.2.3 Cantilever beam test

In addition to the 3PB-tests, cantilever beam tests (CB-tests) were performed. Thereby, the same setup was used that had previously been used by Kirchner et al. (2000), Kirchner et al. (2002a,b) and Schweizer et al. (2004). In the winter 2003/2004 CB-tests were done simultaneously to the 3PB-tests with specimens from the same snow layer. The aim was to acquire a data set with the CB-tests suited for a direct comparison with the above mentioned studies and thus to relate the 3PB-tests to previous CB-test results.

In the CB-test, one part of the specimen was supported while the other part with length L was protruding. L was chosen to be either 10 cm or 15 cm of a total specimen length of 50 cm. For the CB-tests the standard specimen dimensions of 50 cm \times 20 cm \times 10 cm were used (compare Table 3.1). A cut was made from the top, exactly above the line where the support ended, until the protruding part broke off under its own weight. This happened at a critical cut length $a = a_c$ (Figure 3.4).

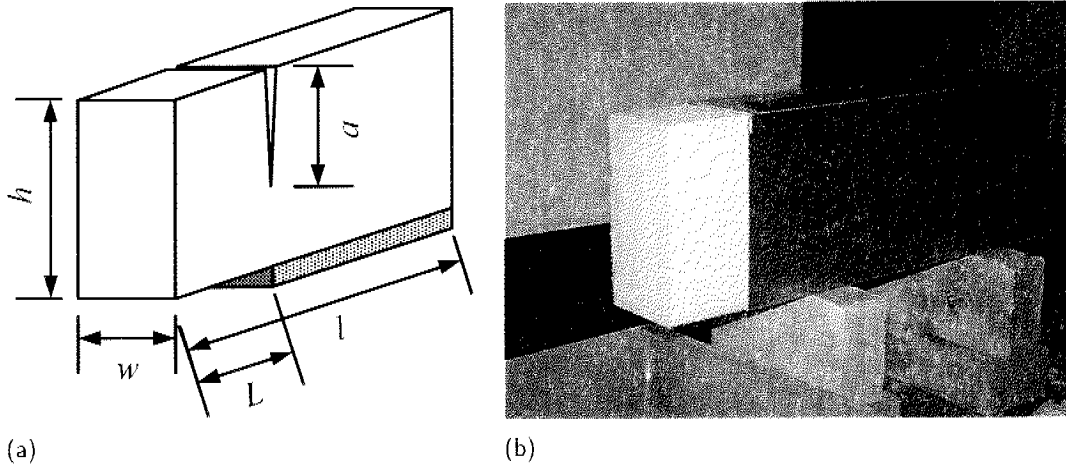


Figure 3.4: (a) Schematic diagram of the cantilever beam test setup. (b) Image of a cantilever beam test.

In a cantilever beam test the crack front is loaded in mixed mode. Therefore, the stress intensity factor in mode II, K_{II} , had to be taken into account

$$G = \frac{K_I^2 + K_{II}^2}{E}. \quad (3.7)$$

For $h - a < L$, the system is equivalent to the asymptotic case of a deep edge crack under a bending moment and a shear force. The corresponding stress intensity factors are given in Tada et al. (2000):

$$K_I = \frac{k_1 M_{CB}}{b^{3/2}}, \quad (3.8)$$

$$K_{II} = \frac{k_2 P_{CB}}{b^{1/2}}, \quad (3.9)$$

where M_{CB} is the moment per specimen width ($M_{CB} = Lh\rho g(L/2)$), b is the ligament length, $b = h - a$. P_{CB} is the cantilever weight per specimen width ($P_{CB} = Lh\rho g$). The constants k_1 and k_2 have to be determined by finite element modelling and were found to be

$$k_1 = 3.975, \quad k_2 = 1.463 \quad (3.10)$$

for homogeneous samples (Tada et al., 2000). In a brittle material like snow, the mode interaction is likely to be governed by the criterion of maximum hoop stress suggested by Evans et al. (1963), which leads approximately to the following failure criterion Schindler (2004):

$$\left| \frac{K_{II}}{K_c} \right| = \frac{\sqrt{3}}{2} \sqrt{1 - \frac{K_I}{K_c}}. \quad (3.11)$$

Rearranging Equation (3.11), and replacing K_c by the critical stress intensity factor for the combined mode I and mode II loading, K_f yields:

$$K_f = \frac{K_I(F_f)}{2} + \sqrt{\frac{K_I(F_f)^2}{4} + \frac{4}{3}K_{II}(F_f)^2}. \quad (3.12)$$

Equation (3.12) slightly deviates from the formulation for the critical stress intensity factor given by Kirchner et al. (2002a), $K_f = \sqrt{K_I^2 + K_{II}^2}$. Particularly for deep cuts, Equation (3.12) is the more appropriate approximation. Taking K_{II} into account in Equation (3.12) increases K_f for our experiments, compared to a pure mode I $K_{I,f}$, by about 6% for a density of 220 kg/m³ and 37% for a density of 335 kg/m³. The influence of K_{II} is thus more important for snow of high densities.

3.2.4 Shear fracture test

Mode II testing is primarily of importance in layered materials, see Section 2.5. Although, much less information is available on mode II than on mode I testing, there exist some standard test setups for mode II (e.g. Hutchinson and Suo, 1992, pp. 114): The end-notched-flexure test (ENF), a kind of 3PB test but with a horizontal cut at one end instead of a vertical cut in the middle, or the end-loaded-split test (ELS), which was adapted for snow by Kirchner et al. (2002a) but did not work satisfactory, because rather a tensile fracture of one part of the split beam was observed than a shear fracture. Due to the fragile nature of snow, these standard tests are not suited for snow. Furthermore, the handling of layered samples turned out to be even more delicate than the handling of homogeneous samples. Therefore, a simple cantilever beam experiment was developed.

The mode II fracture test consists of a notched cantilever beam that is fixed on one side. After the layered snow samples had been carried into the cold laboratory, they were frozen on one side to an aluminium bar. For testing, the bar was rotated 90° so that the horizontal snow layering was now vertical, see Figure 3.5. The height l of the specimen in Figure 3.5 corresponds to the length of the aluminium case with which the specimen was cut out of the snowpack (see Table 3.1). The aluminium bar with the upright snow beam was placed on a table, such that one part of thickness t_t was protruding and one part of thickness t_b was supported by the table. The weak layer was placed exactly above the edge of the table. The protruding layer of thickness t_t corresponds to the layer that was on top of the weak layer in the snow cover (index $t = \text{top}$) and the supported layer of thickness t_b was below (index $b = \text{bottom}$). On top of the protruding layer a mass of $m_{load} = 1 \text{ kg}$ was placed to increase the shear load at the crack tip and thus to decrease the cut length. With a thin metal saw blade a cut was made along the weak layer from the top of the specimen towards the bottom until the protruding part of thickness t_t broke off.

For the calculation of the energy release rate G for our test geometry, no analytical solution could be found. However, as a first approximation the cantilever deep crack solutions of Equations (3.7)-(3.9) could be used. This seemed justified because for our

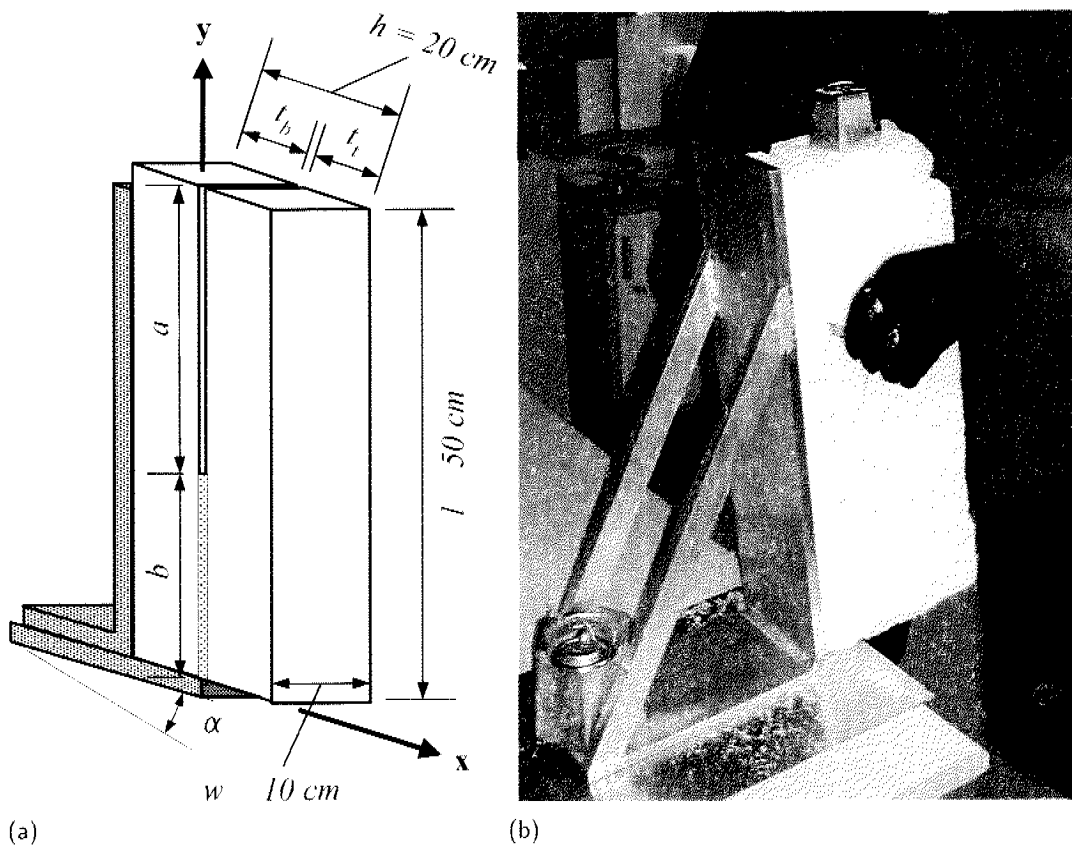


Figure 3.5: (a) Schematic diagram of the shear fracture test setup. (b) Image of the shear fracture test while cutting is in progress. A weight is placed on top of the protruding part.

tests the ligament length b was in the order of the total thickness $h \approx b$. As for the CB-test the loading of the crack tip was expected to be in mixed mode. The Young's modulus E in Equation (3.7) was set equal to E_t , the Young's modulus of the protruding part. The Young's modulus of the supported part was assumed to have only a minor influence, due to its fixation on two sides. This was confirmed in FE simulations. However, in case of two different materials, k_1 and k_2 may differ from the values given in Equation (3.9) depending on the material mismatch.

To maximize the shear component and minimize the tensile component the whole setup was tilted by an angle α . A minimum tensile load results when the opening moment equals the normal force at the location of the crack tip. Because the cut length varied from one experiment to the other and because the exact cut length was not known prior to a test, an exact determination of α was not possible. Instead, we looked at the mean cut length and estimated that for $\alpha = 5^\circ$ the tensile stress would be close to zero in most cases.

In a specimen fixed coordinate system, where the y -axis points along the interface (Figure

3.5) the torsional moment of Equation (3.8), \vec{M}_{CB} , with center of rotation ($x = 0, y = 0$), can be written as

$$\vec{M}_{CB} = \vec{r} \times m \vec{g} = \begin{pmatrix} r_x \\ r_y \\ 0 \end{pmatrix} \times \begin{pmatrix} mg \sin(\alpha) \\ mg \cos(\alpha) \\ 0 \end{pmatrix} = \begin{pmatrix} 0 \\ 0 \\ r_x mg \cos(\alpha) - r_y mg \sin(\alpha) \end{pmatrix}, \quad (3.13)$$

where \vec{r} is the position vector and m is the mass of the protruding snow layer per specimen width $m = t_l l \rho$ with t_l the length of the protruding layer and l its height. g is the gravitational acceleration. P_{CB} , the loading due to the body weight parallel to the interface, depends on α as well and can be written as

$$P_{CB} = mg \cos(\alpha). \quad (3.14)$$

Without any additional loading the center of mass is in the middle of the protruding layer and r_x and r_y can be set to $r_x = l_t/2$ and $r_y = l/2$. In a more general situation, i.e. when an additional weight m_{load} is added on top of the protruding part, the total mass is increased $m = (m_{snow} + m_{load})$ and the center of mass is lifted towards the additional weight. r_y transforms to

$$r_y = \frac{l}{2} \left(1 + \frac{m_{load}}{m_{snow} + m_{load}} \right), \quad (3.15)$$

where $m_{snow} = t_l l \rho$ is the mass of the protruding snow beam per specimen width. Accordingly, the additional mass m_{load} is also per specimen width. Consequently, the moment M_{CB} as a function of the rotation angle α and the additional weight is given as:

$$M_{CB} = (m_{snow} + m_{load})g \left[\cos(\alpha) \frac{l_t}{2} - \sin(\alpha) \frac{l}{2} \left(1 + \frac{m_{load}}{m_{snow} + m_{load}} \right) \right]. \quad (3.16)$$

3.2.5 FE model of shear fracture test

Since the available analytical solutions for a determination of the energy release rate G did not match our experimental set up, a finite element (FE) model of the experimental geometry was created. For the modelling the ANSYS workbench was used. The geometry was modelled consisting of two beams of two different materials, shown in Figure 3.6a. The weak layer was considered to have no extension.

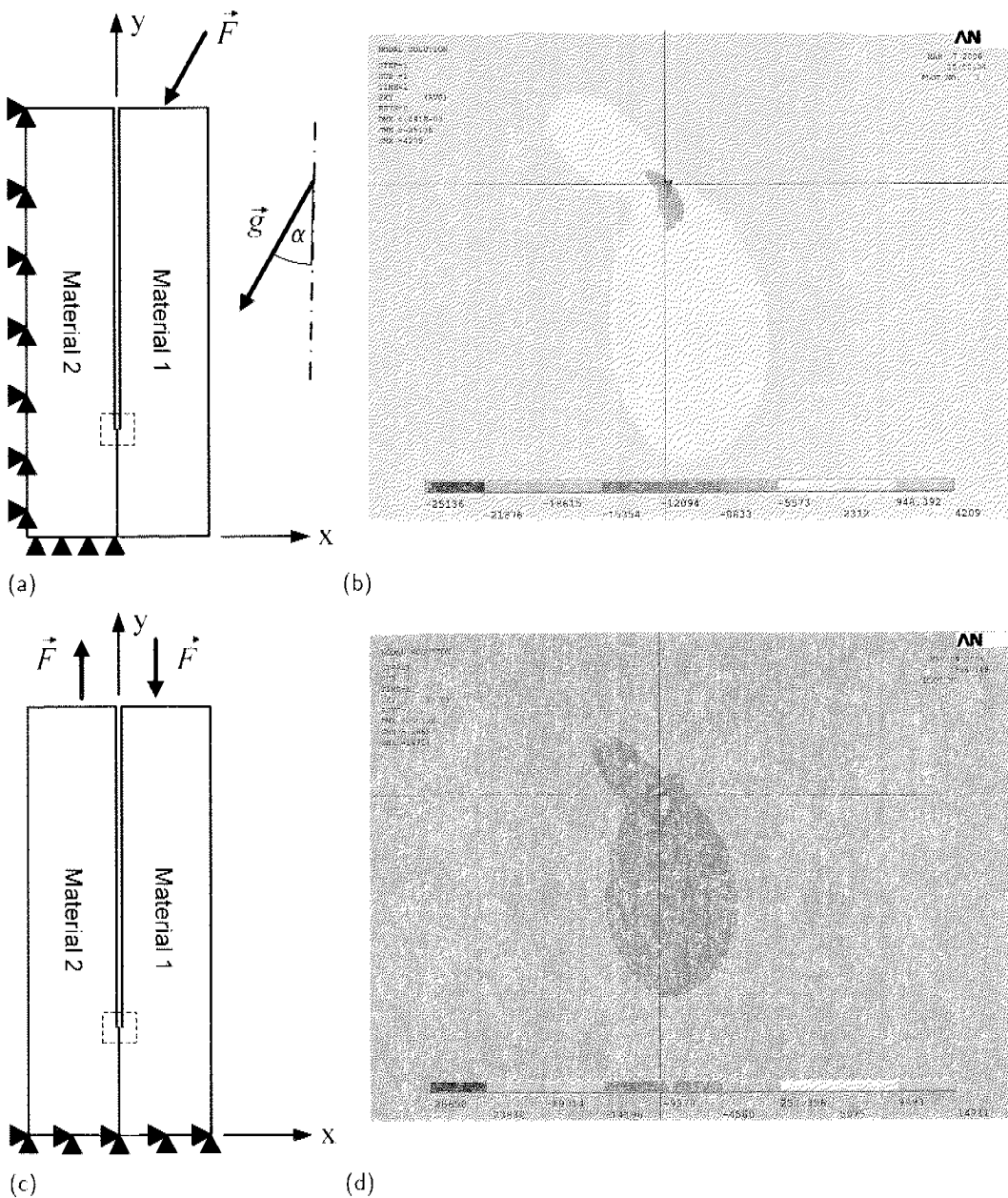


Figure 3.6: (a) Geometry of the FE model. Black triangles indicate the boundary conditions. Nodes are fixed in x and/or in y direction. (b) Detail of the shear stress pattern τ_{xy} acting around the crack tip (ANSYS output). The dashed square in the center of (a) indicates the magnification of (b). The crack tip is in the center of the crosshairs. The crack is coming down from the top. (Material 1: $\rho = 250 \text{ kg/m}^3$, $E = 5 \text{ MPa}$; Material 2: $\rho = 300 \text{ kg/m}^3$, $E = 20 \text{ MPa}$; $\alpha = 5.27^\circ$; $|\vec{F}| = 9.81 \text{ N}$.) (c) For comparison a pure shear stress case is simulated. (d) The material properties of material 1 and 2 are the same as for (b). ($|\vec{F}| = 20 \text{ N}$, no gravity is applied.)

In two steps the total strain energy $U(a)$ for a situation with a cut length a , and $U(a + \Delta a)$ for a cut length $a + \Delta a$ were calculated, where Δa is a small increase in the cut length. The energy release rate G could then be calculated according to Equation (2.9) as the difference of these two energies divided by the specimen thickness w and the cut length increment Δa :

$$G(a) = \frac{U(a + \Delta a) - U(a)}{w\Delta a}. \quad (3.17)$$

Δa must be chosen small enough for $G(a)$ to converge but large enough to avoid errors due to the limited precision of the FE model.

To verify the numerical model, the infinitely long thin film of Figure 2.6 was modelled ($l \gg l_b, l_t$) for which Suo and Hutchinson (1990) had derived an exact analytical solution (Equation 2.33). The difference between numerical results and analytical solution did not exceed 4% for various loading conditions. Subsequently, the model was adapted to our experimental geometry. The geometry, loads and boundary conditions are indicated in Figure 3.6a. Nodes on the left boundary were fixed in x and y direction, to model the icing of the snow block to the aluminium bar. Nodes on the bottom left boundary were fixed in y direction, corresponding to the support of the specimen on the table. The gravitational acceleration g was implemented, acting with an angle α to the vertical. The additional weight which was placed on top of the protruding snow layer was modelled as a point load. Figure 3.6b shows the shear stress τ_{xy} acting around the crack tip. The shear stress can be compared qualitatively to the simulation of a pure shear case (Figure 3.6c and d). The stress distributions looks qualitatively the same, although the stress amplitudes are different, what explains the different colour code. The similarity of the stress patterns should thus justify the assumed 5° for the inclination angle α .

3.3 Field test

As the name implies, weak layers are in general not suited for any kind of transportation. The shear fracture tests involved a highly delicate transport of some more robust weak layer specimen to the cold laboratory. However, for many weak layers a transport is not feasible. These weak layers are assumed to be the most relevant for slab avalanche release. Therefore the development of a field test was a major step towards more "realistic" experiments even though less accurate. More realistic means in this context that larger samples could be tested in-situ on slopes where avalanches potentially could occur.

The field test was designed to answer the following questions:

- Is it possible to determine the energy release rate of a weak layer directly in the field?
- Does the cut length depend on the specimen length?

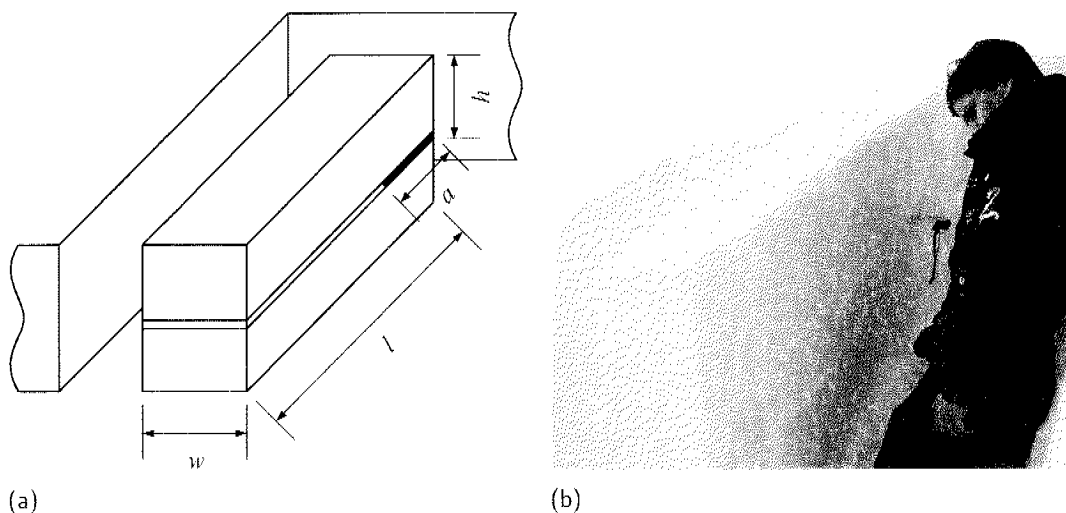


Figure 3.7: (a) Schematic diagram of the field test. (b) Cutting along the weak layer of an isolated snow block in a slope.

- Is a crack propagation possible in slopes less steep than 30° ?
- Can a field test be further developed into a standard field test for operational avalanche forecasting that would be useful to assess the potential for fracture propagation?

The field test consisted of snow beams with a width of 30 cm and a variable length of 60 cm, 120 cm, or 180 cm. The beams were isolated on all four sides on a slope (Figure 3.7). After the weak layer had been identified by compression tests, a cut was made along the weak layer with a snow saw (thickness 2 mm) until the crack length became critical and self-propagation of the crack started. The cut was usually made in downslope direction and occasionally in upslope direction.

In order to make the field experiments comparable to the laboratory tests, the width of the snow beams was kept short in relation to the length. For the laboratory tests the ratio of width to length was $w/l = 1/5$, for the field tests it was $w/l = 1/2, 1/4, 1/6$, depending on the beam length. The width was kept constant for all beam length as it was done for the different specimen sizes used in the laboratory for the fracture tests in mode I. The major difference between the field test and the shear fracture test is the inclination of the weak layer. Whereas in the laboratory α was set to 5° , corresponding to an inclination of the weak layer of $\varphi = 90^\circ - \alpha = 85^\circ$, the field tests were performed in slopes with an inclination of $25^\circ < \varphi < 35^\circ$.

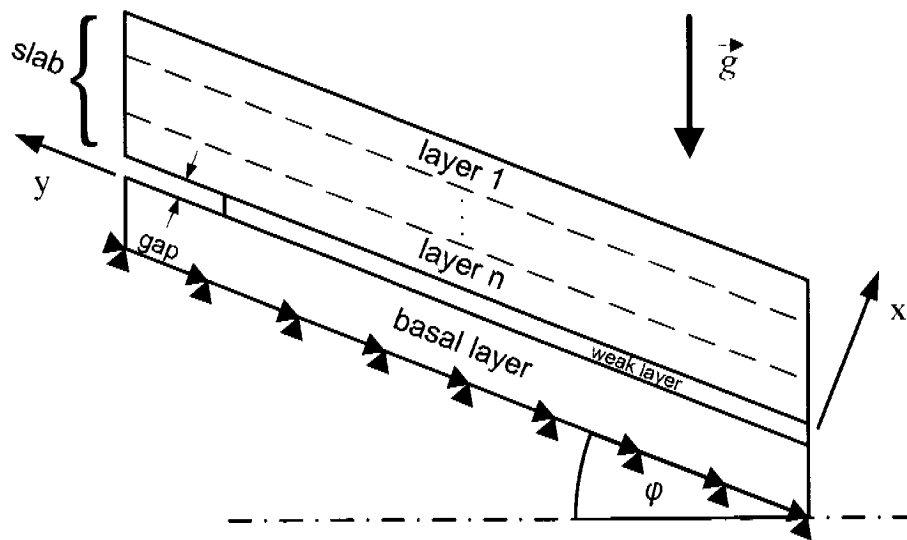


Figure 3.8: Geometry of the FE model. Black triangles indicate the boundary conditions. Nodes are fixed in x and y direction.

3.3.1 FE model of field test

As for the shear fracture experiments a FE model was generated for the geometry of the field experiments. The energy release rate was calculated according to Equation (3.17). A schematic diagram of the FE model can be seen in Figure 3.8. The model consisted of a basal layer which was fixed in x and y direction at the bottom (black triangles in Figure 3.8) overlaid by a slab consisting of n layers. For our experiments the slab was modelled as to consist of three layers $n = 3$, because in the SMP penetration resistance signals three layers could be clearly distinguished. For a future application the model could be adjusted to more layers by including additional layers in the input file for ANSYS.

Not only the length of the cut a_c , that was made with the snow saw, was modelled but also the cut thickness. The snow saw had a thickness of 2 mm and therefore this gap of 2 mm indicated as *gap* in Figure 3.8. The cut surfaces were modelled as contact and target areas, in case the two surfaces would get in contact due to bending. However, the results showed that for the measured critical cut length the slab was stiff enough so that the two crack surfaces did not get in contact (Section 4.3). The bending of the slab due to the cut length a_c was at maximum half of the gap size of 2 mm.

3.4 Young's modulus

The determination of the Young's modulus E of a given snowpack layer is of prime importance, since the calculation of fracture mechanical parameters, such as the energy

release rate or the critical stress intensity factor (in a layered material), requires the knowledge of the Young's modulus.

A precise measurement of the Young's modulus is still a difficult task and far from being a standard procedure. One reason for this is again the fragile nature of snow which makes standard measurement techniques very difficult and sometimes even impossible. Furthermore, the Young's modulus will depend on the direction of loading. A loading in lateral direction will result in a different modulus than a loading in vertical direction due to the vertical layering of the snowpack. Basically, four different approaches can be distinguished:

- **Quasi static:** The elastic modulus has traditionally been measured from the linear elastic region of a uniaxial tensile stress-strain curve, and is defined as the ratio of stress to strain during elastic loading (Mellor, 1975). Recently, Scapozza (2004) has made uniaxial compression experiments. His findings agreed well with the ones summarized by Mellor (1975) (see Figure 4.14).
- **Dynamic:** In dynamic experiments the snow specimen is activated with small displacements of a given frequency, normally between 10 Hz and 10 kHz. The pulse propagation, flexural vibration or the force response is measured from which the Young's modulus is calculated. Mellor (1975, p.257) reports that the results for a dynamic measurement can be a factor of 2 higher than quasistatic measurements. Camponovo and Schweizer (2001) performed dynamic torsional shear experiments at a frequency of 1 Hz with a stress-controlled rheometer and determined the shear modulus of snow for different snow densities and temperatures.
- **Derived from microstructural properties:** With the aid of computer microtomography (Schneebeli, 2002) the exact ice-matrix of a given snow sample can be modelled. By applying the mechanical properties of ice to the matrix, an elastic modulus for the snow sample can be calculated. This might be the method with the highest precision, however measurements are time consuming, can only be made for small samples with a volume of a few cubic centimeters and require an expensive equipment.
- **Derived from penetration resistance:** Probably the most promising method is to calculate an Young's modulus based on the penetration resistance signal of a SnowMicroPen (Johnson and Schneebeli, 1999). A resistance profile can be acquired directly in the field and within minutes. However, the conversion of the penetration resistance into an Young's modulus is rather complex and seems to need a calibration with field measurements first (Kronholm, 2004).

For our experiments we used a dynamic measurement method to evaluate the Young's modulus and compared the results to the results derived from the SMP penetration resistance signal.

3.4.1 Dynamic measurement with cyclic loading device

A prototype of a cyclic loading device, developed at SLF, was used to determine the Young's modulus (Hempel, 2004). Small cylindrical samples with a diameter of 48 mm and a height of 30 mm were cut out of the snow specimens after a fracture test. Then, the samples were mounted on a device where they were loaded and unloaded with a frequency of 100 Hz (Figure 3.9 a). The force response F due to the predefined displacement $\Delta h = 8 \mu\text{m}$ was recorded. A displacement of $\Delta h = 8 \mu\text{m}$ corresponds to a deformation of $\varepsilon = \Delta h/h = 2.7 \cdot 10^{-4}$ and with the applied frequency of 100 Hz a strain rate of $\dot{\varepsilon} = 2.7 \cdot 10^{-2} \text{s}^{-1}$ results. With the force-displacement information a dynamic Young's modulus was determined, according to the relation

$$E = \frac{\sigma}{\varepsilon} = \frac{F}{A} \cdot \frac{h}{\Delta h}, \quad (3.18)$$

where h is the height of the sample and A its cross sectional area. The calculated Young's modulus increases rapidly with increasing loading frequency between 0.1 Hz and 50 Hz and then successively flattens with a further increase in the frequency (Figure 3.9 b). At frequencies around 200 Hz a resonance was observed which influenced the measurements considerably. This resonance is believed to be either the result of a resonance frequency of the steel frame or the result of an improper icing of the snow sample to the sample holder or the pressure plate. The icing of the snow sample was a sensitive procedure. It happened that above a certain frequency, the contact between snow and pressure plate or snow and sample holder deteriorated.

From experiments with polycrystalline ice (Sinha, 1978) it is known that the Young's modulus increases with increasing loading frequency (Figure 3.10). For lower frequencies there is a steep increase which levels off between 100 and 200 Hz.

For our measurements a frequency of 100 Hz was chosen, to be as close to a flat region as possible but still far enough away from the resonance frequency.

3.4.2 Derived from penetration resistance

Kronholm (2004) was the first who used the penetration resistance signal of the SnowMicroPen to estimate the Young's modulus of different layers of the snowpack. According to Kronholm (2004), the values of the modulus derived from the SMP signal are too small by a factor of about 150 compared to the measurements of Mellor (1975).

The theory to calculate the Young's modulus from penetration resistance was developed by Johnson and Schneebeli (1999) and is based on mechanical theories for cellular solids (Gibson and Ashby, 1997). The Young's modulus E of a given snow layer can be calculated as a function of the average rupture force for the microstructural element within

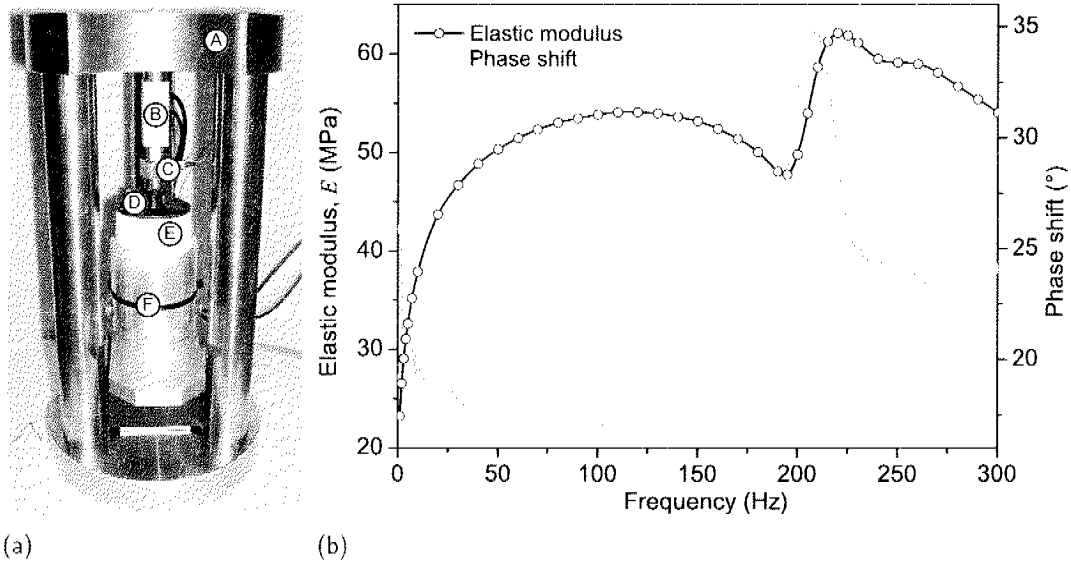


Figure 3.9: (a) Image of the cyclic loading device (F. Hempel, SLF). (A) solid steel frame, (B) piezo-actuator, (C) force sensor, (D) pressure plate, (E) snow sample, (F) sample holder (steel). (b) Young's modulus in dependence of the applied frequency. Measurements were performed in winter 2004/2005 by Felix Book for snow consisting of small rounded grains, 0.5 – 1 mm, 1F with a density of about 270 kg/m^3 .

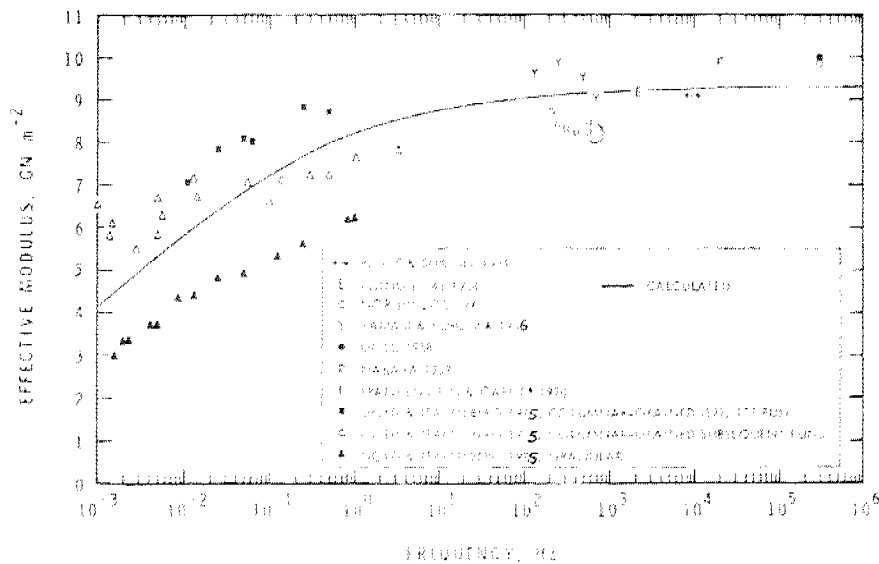


Figure 3.10: Frequency dependence of effective Young's modulus for polycrystalline ice at -10°C . From Sinha (1978).

the layer, \bar{f}_r , and the average microstructural element length in the layer, \bar{L}_n

$$E = \frac{\bar{f}_r}{\bar{L}_n^2 (\sin \theta + \mu \cos \theta)}, \quad (3.19)$$

where θ is half of the angle of the SMP tip (30°) and μ the frictional coefficient between the SMP tip and the snow grains. The frictional coefficient between ice and metal μ is assumed to be 0.25. L_n can be calculated as a function of the number of elements that fail n_{fail} when the SMP cone with area A_s travels over a distance of Δz

$$L_n = \left(\frac{\Delta z}{n_{fail}} A_s \right)^{1/3}. \quad (3.20)$$

3.5 High-speed photography

To document in detail the fracture process during the 3PB-tests and the shear fracture tests, several tests were captured with a high-speed camera. The Vosskühler HCC-1000 camera features a maximum of 462 pps (pictures per second) with an image resolution of 1024×1024 pixels. For lower image resolutions the image rate can even be increased up to 1825 pps.

The system consists of a camera and a laptop which controls the camera and on which the data are stored. First data analysis can be done on the laptop right after recording. The number of images that can be stored is limited to 512 images. Therefore, a higher image rate results in a shorter recording time. Tests were made with image rates of 115 pps, 230 pps and 462 pps, resulting in recording times of 4.5 s, 2.2 s and 1.1 s, respectively. Since the triggering of the camera was made by hand, the image rate could not be further increased without the risk of missing the fracture. For a further increase of the image rate an automatic triggering would be necessary. This would be, at least for the 3PB-tests, relatively easy to realize. In the data acquisition program for the 3PB-tests written in LabView, a trigger signal could be sent to the camera as soon as the recorded force signal exceeds a given threshold value. As long as the mean peak force is known for a given specimen size it would be possible to decrease the time between trigger signal and opening of the camera to approximately $100 \mu\text{s}$. A further decrease of the time would not be suitable because the threshold would then be too close to the mean peak force and, due to the scattering, some tests would fall below the threshold and would not trigger the camera.

Seite Leer /
Blank leaf

Results

During three winter seasons, 2003/2004, 2004/2005 and 2005/2006 experiments to determine fracture mechanical properties of snow were performed. In the first two winter seasons most of the experiments were performed in the cold laboratory. This had the advantage that precise measuring instruments could be used that would not have been transportable to the field. Furthermore, the temperature could be controlled and the experiments were independent of atmospherical conditions like wind, snowfall or radiation. All snow specimens that were tested in the cold laboratories were collected in the field and transported to the lab. In the third winter season experiments were performed in the field. Experimenting in the field had the advantage, that test conditions were representative for the conditions in which fracture processes occur in the snow cover on a slope. Very fragile weak layers could be tested that could not be transported to the laboratory without destroying the weak layer.

The chapter is divided in three sections according to the three main experimental focuses: In Section 4.1 the results of the experiments with homogeneous snow samples performed in the cold laboratory are presented. Section 4.2 summarizes the experiments with layered snow samples in the cold laboratory. In Section 4.3 the results of the field experiments will be given.

4.1 Fracture in homogeneous snow samples

Although a shear fracture in the layered snow cover occurs before the snow slab fails in tension, as explained in Section 1.3, we started to experiment with homogeneous snow samples for several reasons: Experiments in homogeneous snow were essential to improve the understanding of the general fracture mechanical behaviour of snow, to test and confirm previous results and to gain experience for the more difficult mode II experiments in layered snow samples. In addition, layered snow samples are in general

Table 4.1: Summary of type (3PB = three-point bending test, CB = cantilever beam test) and number of fracture experiments in mode I. Snow type is given as grain shape, grain size and hardness index according to ICSSG (Colbeck et al., 1990).

Series	Date of sampling	Type and (number) of experiments	Specimen size (l, h, w) (cm)	Snow type	Snow density = σ_{dev} (kg/m ³)	Snow temp. (°C)	Rel. cut depth a/h
A	6 Jan 04	3PB (7)	(50, 20, 10)	Small rounded, 0.25 – 0.5 mm, 1F-	254 ± 12	-6.5	0.3...0.55
B	27 Jan 04	3PB (12)	(50, 20, 10)	Decomposed and fragmented, partly faceted, 0.5 – 1 mm, F-4F	148 ± 3	-8.8	0.1...0.52
C	5 Mar 04	3PB (6) CB (11) ^a , (4) ^b	(50, 20, 10)	Small rounded and faceted, 0.25 – 0.75 mm, 4F	220 ± 7	-10.6	0.1...0.5 0.3...0.63 ^{a,b}
D	9/10/11 Mar 04	3PB (27) CB (13) ^a , (26) ^b	(50, 20, 10)	Small rounded and partly mixed forms, 0.5 – 1 mm, 1F-K	328 ± 17	-11.0	0.25...0.51 0.74...0.88 ^{a,b}
E	21 Apr 04	3PB (17)	(20, 8, 10) (31, 13, 10) (50, 20, 10) (80, 32, 10)	Decomposed and fragmented, small rounded, 0.5 – 1 mm, F-4F	186 ± 12	-14.5	0.1
F	27 Jan 05	3PB (53), (17) ^c	(20, 8, 10) (31, 13, 10) (50, 20, 10) (80, 32, 10)	Small rounded and partly decomposed and fragmented, 0.25 – 0.75 mm, 1F	310 ± 19	-9.3	0.1
G	2 Feb 05 2 Mar 05 3 Mar 05	3PB (30) ^c (3 density groups)	(50, 20, 10)	Decomposed and fragmented, 0.5 – 1 mm, F Mixed forms, 0.5 – 1.25 mm, 4F Small rounded and partly mixed forms, 0.25 – 0.5 mm, 1F-K	107 ± 22 221 ± 30 309 ± 13	-9.7	0
H	10 Feb 05	3PB (22), (6) ^c	same as F all 4 sizes	Small rounded and partly decomposed and fragmented, 0.5 – 1 mm, 4F	239 ± 9	-9.5	0.1
I	22 Feb 05	3PB (23)	same as F all 4 sizes	Small rounded and partly decomposed and fragmented, 0.5 – 1 mm, 4F-1F	256 ± 19	-9.1	0.1

^aCantilever beam test with cantilever length $L = 10$ cm

^bCantilever beam test with cantilever length $L = 15$ cm

^cUnnotched 3PB tests to determine the tensile strength

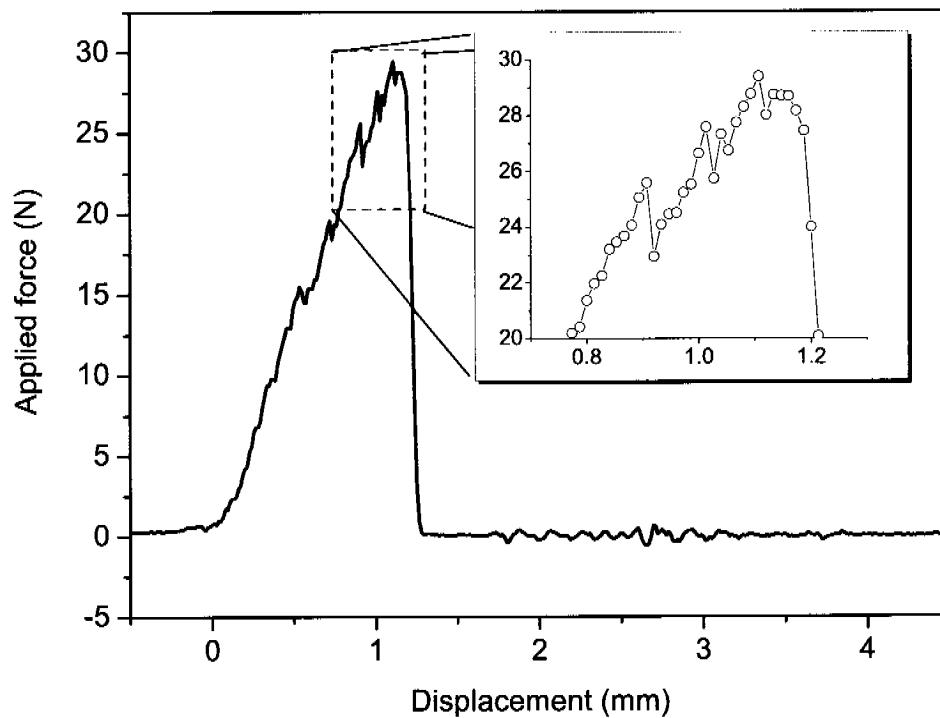


Figure 4.1: Load-displacement curve for a three-point bending fracture experiment with a snow specimen. The test was performed with a displacement rate of 200 mm/min and a sampling rate of 250 Hz. The inset shows the peak load and the single measurement points. (Specimen dimensions: 50 cm \times 20 cm \times 10 cm, density: 240 kg/m³).

even more fragile than homogeneous snow samples.

For the mode I experiments we focused on experiments in three-point bending (3PB-tests). Additionally, cantilever beam tests (CB-tests) were made in order to directly compare our results with previously published results obtained with similar cantilever tests. The 3PB-tests were performed with a standard material testing machine, described in Section 3.2.2, which recorded a force-displacement signal while testing.

4.1.1 Behaviour of snow under loading

In mechanics and engineering load-displacement or stress-strain diagrams play a crucial role for the characterization of material behaviour.

For each 3PB-experiment a load-displacement signal was recorded. This information was

used to determine the peak load at failure, F_f . Figure 4.1 shows one representative example of a force-displacement signal. At 0 mm the sensor head applying the load and including the force sensor touched the snow specimen. After getting in contact, the force increased approximately linear until the specimen failed at a displacement of about 1.2 mm and a peak load of $F_f = 29.4$ N. After failure, the force signal dropped down to 0 N. The inset in Figure 4.1 shows the force signal at peak load. The single measurement points are displayed. The time resolution between successive points was $4\mu\text{s}$. It can be seen that during the increase of the force several small drops of the force occurred. These drops became more pronounced and more frequent the closer they occurred to the specimen failure. Once the peak load was reached, the force signal dropped down to 0 N only after a further displacement of about $100\mu\text{m}$ or a time of 25 ms.

4.1.2 Tensile strength

Many field and laboratory experiments have been done in the past to determine the tensile strength of snow (e.g. Mellor, 1975; Narita, 1980; Jamieson and Johnston, 1990). Although we focus on fracture mechanical properties of snow, tensile strength is still an important parameter for the calculation of certain fracture mechanical parameters. We needed the tensile strength for the evaluation of the fracture process zone, R_c , Equation (2.20), and for the determination of the failure assessment diagram (FAD), Equation (2.29). First evaluations were made by using literature data for the tensile strength, but the results were not satisfactory, because the nominal stresses of notched specimen exceeded in several cases the tensile strength. This was most probably due to the fact that previous results were obtained with different test methods and sample sizes. Therefore, we decided to measure the tensile strength in a 3PB-test, to be able to directly compare 3PB fracture tests with 3PB tensile strength tests.

The tensile strength σ_c was calculated according to Equation (3.3). In contrast to the fracture experiments, the specimens were not notched. The specimens were taken from the same snow layers as for the fracture experiments.

The results are compiled in Figure 4.2. The tested snow consisted mainly of small rounded grains and mixed forms with densities between 80 kg/m^3 and 350 kg/m^3 . Details can be found in Table 4.1. The errors displayed in Figure 4.2 were calculated according to the elementary laws of error propagation. A detailed description of the error calculation and a list of the main contributory parameters can be found in Appendix A. The mean error was 7% and the errors did not exceed 13%. A power law relation $\sigma_c = A\rho^B$ was fitted to the data with $(A = 2 \times 10^{-5} \pm 5 \times 10^{-5})\text{ Nm/kg}$ and an exponent $B = 2.44 \pm 0.50$. The fit function had a coefficient of determination of $R^2 = 0.61$ (dash-dotted line in Figure 4.2). If one considers the relative density (ρ/ρ_{ice}) , as it is commonly done in literature, the resulting tensile strength to relative density function for our 3PB-tests can be written as $(\rho_{ice} = 917\text{ kg/m}^3)$

$$\sigma_c = 210 \left(\frac{\rho}{\rho_{ice}} \right)^{2.44} \text{ kPa.} \quad (4.1)$$

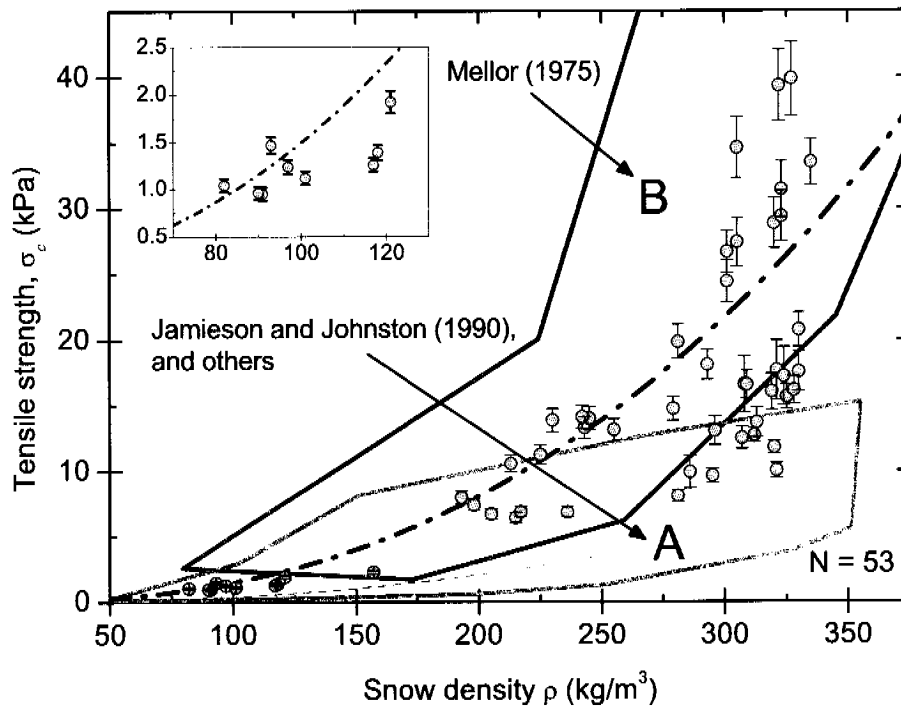


Figure 4.2: Density dependence of the tensile strength measured in 3PB-tests and comparison to literature data of Jamieson and Johnston (1990) and others (area A) and of Mellor (1975) (area B). The inset is a magnification of the diagram for low snow densities. The dash-dot line indicates the best power-law fit for our data (Equation 4.1), and the dashed line the power-law fit given by Jamieson and Johnston (1990).

Jamieson and Johnston (1990) found in their field experiments for similar snow types a relation of: $\sigma_c = 79.7 (\rho/\rho_{ice})^{2.39}$ kPa (dashed line in Figure 4.2). The data in Figure 4.2 are compared to the results of Jamieson and Johnston (1990) and others and to the data summarized by Mellor (1975). Our data fall within the range of these two studies.

4.1.3 Critical stress intensity factor in mode I from 3PB-tests

In 3PB-tests with pre-cracked snow beams the critical stress intensity factor, K_{If} , was evaluated according to Equation (3.4). Eight series were made in total, series A to I with exception of series G, with densities ranging from 150 kg/m³ up to 370 kg/m³. Detailed information of the series is given in Table 4.1. The results are compiled in Figure 4.3.

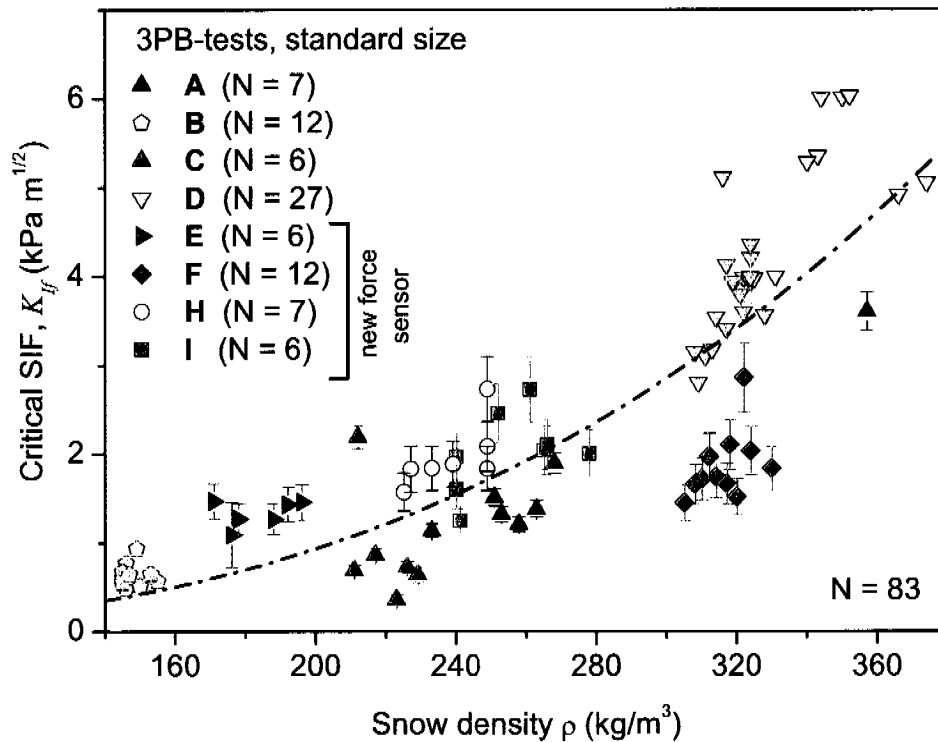


Figure 4.3: Dependence of the critical stress intensity factor in mode I, K_{I_f} , on snow density. Only three-point bending tests of the standard size 50 cm \times 20 cm \times 10 cm of series A to I are included. The series are colour coded and the number of experiments of every series is indicated. (Series E to I were performed with the new and better resolving force sensor). A power-law relation (Equation 4.2) was fitted to the data (dash-dot line).

Data were colour coded according to the experimental series.

The dependence of mechanical properties on density were analysed in the past and best fits have been achieved by assuming a power-law relation, $y = Ax^B$, where A and B are constants to be determined (Perla et al., 1982). (The choice of the fit function will be discussed in section 5.1.3). Our data were best fitted by a power-law with $A = (4.20 \times 10^{-7} \pm 6.56 \times 10^{-7}) \text{ kN m}^{3/2} \text{ kg}^{-1}$ and $B = 2.76 \pm 0.27$ with a coefficient of correlation of $R^2 = 0.70$:

$$K_{I_f} = 4.20 \times 10^{-7} \rho^{2.76} \text{ kPa}\sqrt{\text{m}}. \quad (4.2)$$

The errors of K_{I_f} in Figure 4.3 were calculated analogous to the errors in section 4.1.2 (Appendix A). The mean error was 10% and the errors did not exceed 15%.

Table 4.2: Mean critical stress intensity factor $K_{I_f}^*$ (normalized to the mean density) for the three experiment types (3PB = three-point bending; CB = cantilever beam). Series C was normalized to a density of 220 kg/m^3 and Series D to 330 kg/m^3 .

Type of experiment	Series C		Series D	
	Mean $K_{I_f}^*$ (kPa $\sqrt{\text{m}}$)	Deviation (%)	Mean $K_{I_f}^*$ (kPa $\sqrt{\text{m}}$)	Deviation (%)
3PB	0.64 ± 0.23		4.27 ± 0.66	
CB ($L = 10 \text{ cm}$)	0.42 ± 0.12	-34	2.69 ± 0.57	-37
CB ($L = 15 \text{ cm}$)	0.51 ± 0.13	-20	3.18 ± 0.53	-25

4.1.4 Critical stress intensity factor in mode I from CB-tests

In series C and D, 3PB-tests were made simultaneously to CB-tests. The aim was to acquire a data set with the CB-tests suited for a direct comparison with previous studies and thus to relate the 3PB-tests to previous CB-test results. Cantilever beams with two different beam length of the protruding part were tested, $L = 15 \text{ cm}$ and $L = 10 \text{ cm}$.

Since we aimed at a comparison of K_{I_f} obtained by different experimental methods and since the density of the specimens varied slightly, we had to normalize the data to a defined density.

Series C had a mean density of $220 \pm 7 \text{ kg/m}^3$ (Table 4.1). The data were thus normalized to a density of $\rho_0 = 220 \text{ kg/m}^3$ in order to eliminate the density dependence. The density converted value for the critical stress intensity factor $K_{I_f}^*$ was found by $K_{I_f}^* = K_{I_f} + (A\rho_0^B - A\rho^B)$, where A and B are the coefficients found in relation (4.2). The mean $K_{I_f}^*$ of the CB-tests with $L = 10 \text{ cm}$ were found to be 34% smaller than the mean $K_{I_f}^*$ for the 3PB-tests. The CB-tests with $L = 15 \text{ cm}$ were 20% smaller (Table 4.2). The deviations were within the standard errors of the $K_{I_f}^*$ values.

Series D, with a mean density of $328 \pm 17 \text{ kg/m}^3$, was normalized to $\rho_0 = 330 \text{ kg/m}^3$. The mean $K_{I_f}^*$ of the CB-tests with $L = 10 \text{ cm}$ were found to be 37% smaller than the mean $K_{I_f}^*$ for the 3PB-tests. The CB-tests with $L = 15 \text{ cm}$ were 25% smaller. In contrast to series C the deviations were no longer within the standard errors of the $K_{I_f}^*$ values.

Figure 4.4a shows the calculated $K_{I_f}^*$ values according to Equation (3.12) for series C and Figure 4.4b for series D. The CB-tests were distinguished according to the length of the protruding beam and compared to the 3PB-tests of series C and D.

Among the CB-tests, the ones with a cantilever length of $L = 10 \text{ cm}$ failed at smaller $K_{I_f}^*$ than the ones with $L = 15 \text{ cm}$. For the CB-tests, $K_{I_f}^*$ increased with increasing cantilever length L (Figure 4.4b). In contrast to the 3PB-tests, the CB-tests showed a significant dependence of $K_{I_f}^*$ on the relative cut length a/h (Figure 4.4b).

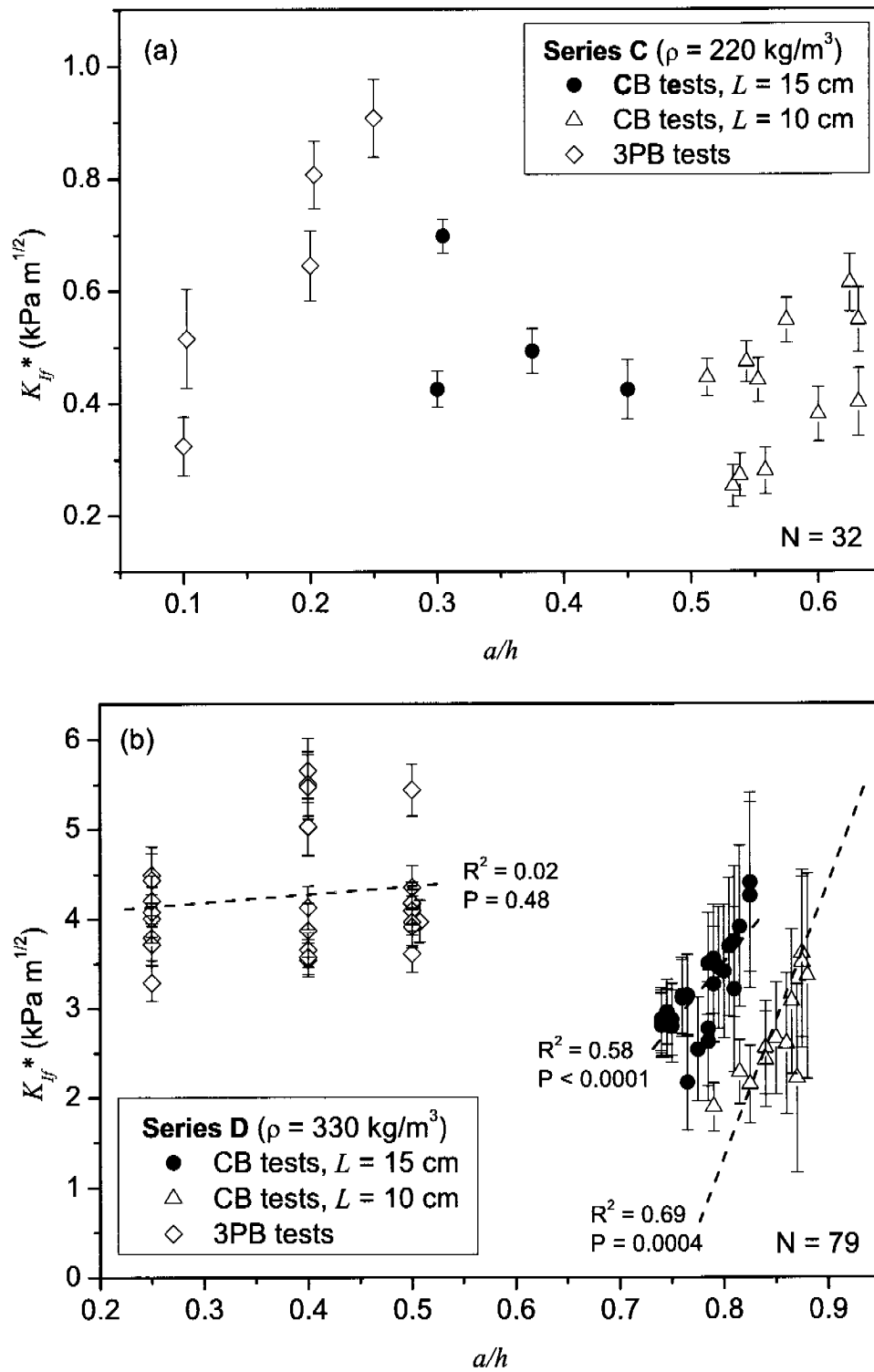


Figure 4.4: Dependence of the critical stress intensity factor $K_{I_f}^*$ (normalized to the mean density) on the relative cut depth a/h , (a) for series C and (b) for series D. Cantilever beam (CB) tests with two different length of the protruding beam are compared to three-point bending (3PB) tests.

4.1.5 Quantification of the size effect

This section summarizes the results of the experiments to determine the size dependence of the critical stress intensity factor, $K_{I,f}$. All experiments were performed in three-point bending. Four different specimen sizes were used for the tests (see Table 3.1), and four experimental series were performed (Series E, F, H and I, see Table 4.1).

As it was presented in Section 2.4.3 it is possible to experimentally obtain a characteristic size D_0 and an equivalent fracture toughness $K_{I,c}^e$ by plotting the inverse of the square of the nominal strength σ_f^{-2} against the specimen height h , and by determining intercept and slope of a linear regression (Bazant and Planas, 1998). The nominal strength can be determined according to Equation (3.3) as the nominal stress at failure. Therefore, the force at failure F_f has to be inserted. Figures 4.5 and 4.6 show the data for series E, F, H and I. Out of these four diagrams the parameters c_1 and c_2 were determined as intercept and slope of a linear regression line (Equation 2.23).

In the data of series I, Figure 4.6b, two points were excluded in the linear regression analysis. These two points are marked with an arrow. They were neglected because the SMP penetration resistance signal was in one case much higher and in one case very low compared to all other specimen, indicating that these two specimen had different snow properties.

The coefficients of determination R^2 were for all four series low (Table 4.3). However, if we judge linear regressions with a level of $P < 0.05$ as statistically significant, the linear regressions of series E and F were statistically significant and series H was even highly significant. Only the regression for series I was statistically not significant. The level of significance P is indicated in Table 3.1.

According to Bazant and Planas (1998), the characteristic size D_0 can be calculated out of the coefficients c_1 and c_2 . The results for series E, F, H and I are listed in Table 3.1. The mean characteristic size \bar{D}_0 was then calculated as mean of the results for the three statistically significant series E, F and H:

$$\bar{D}_0 = 0.29 \pm 0.08 \text{ m.} \quad (4.3)$$

If series I, which was statistically not significant, is also included, $\bar{D}_0 = 0.34 \pm 0.09 \text{ m}$ results.

In Figure 4.7 the logarithm of the nominal strength σ_f is plotted against the logarithm of the specimen height h for all four series (E, F, H and I). The diagram corresponds to the schematic diagram in Figure 2.4 showing the fracture mechanical size effect on the strength of a material (Bazant and Planas, 1998). A linear regression (dash-dotted line in Figure 4.7) resulted in

$$\log(\sigma_f) = 0.74 - 0.21\log(h), \quad (4.4)$$

with a level of significance $P = 0.0002$ and a coefficient of determination $R^2 = 0.12$. The slope of the linear regression of -0.21 ± 0.05 is significantly lower than the required slope

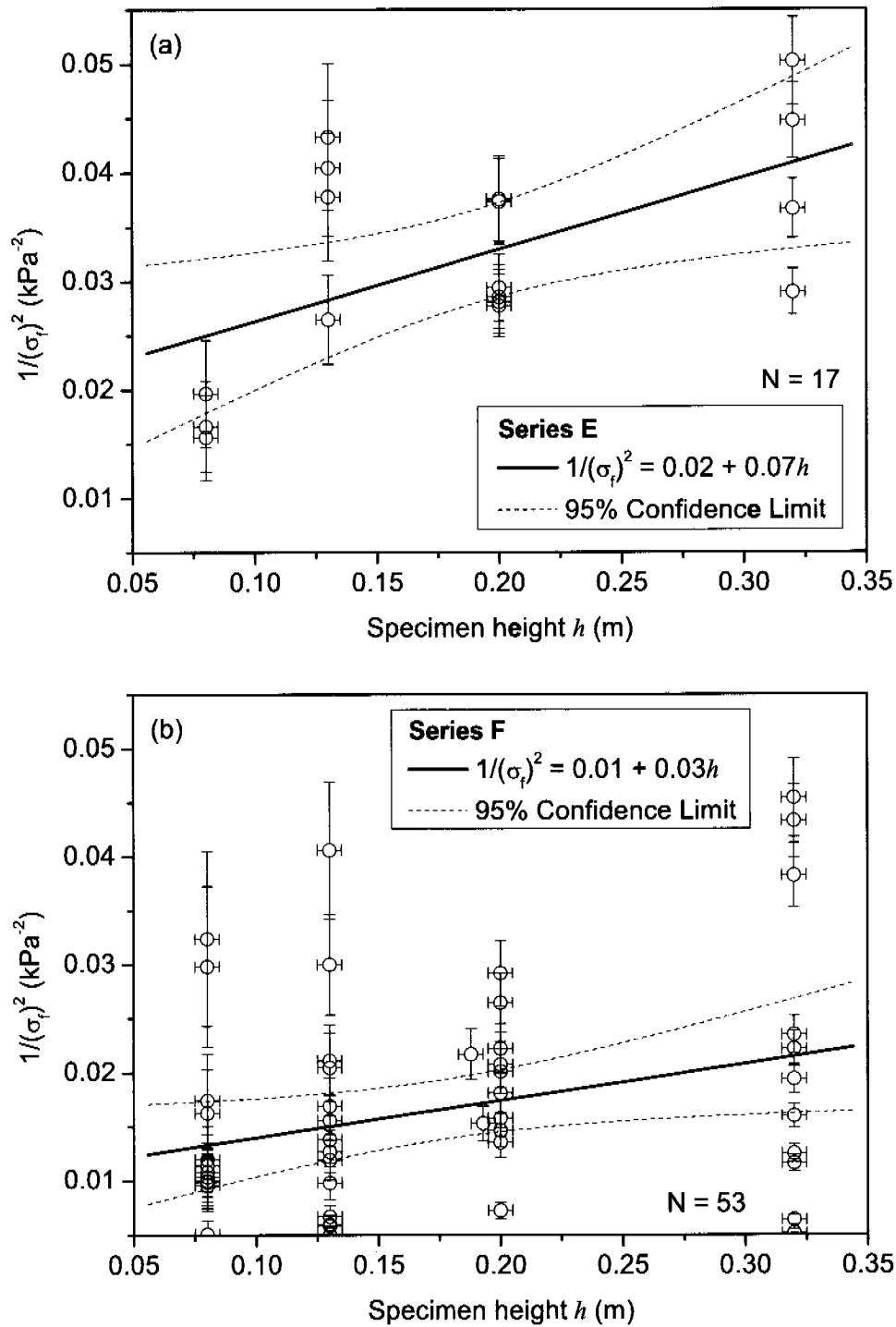


Figure 4.5: The inverse of the square of the nominal strength σ_f in relation to the specimen height (a) for Series E, and (b) for Series F.

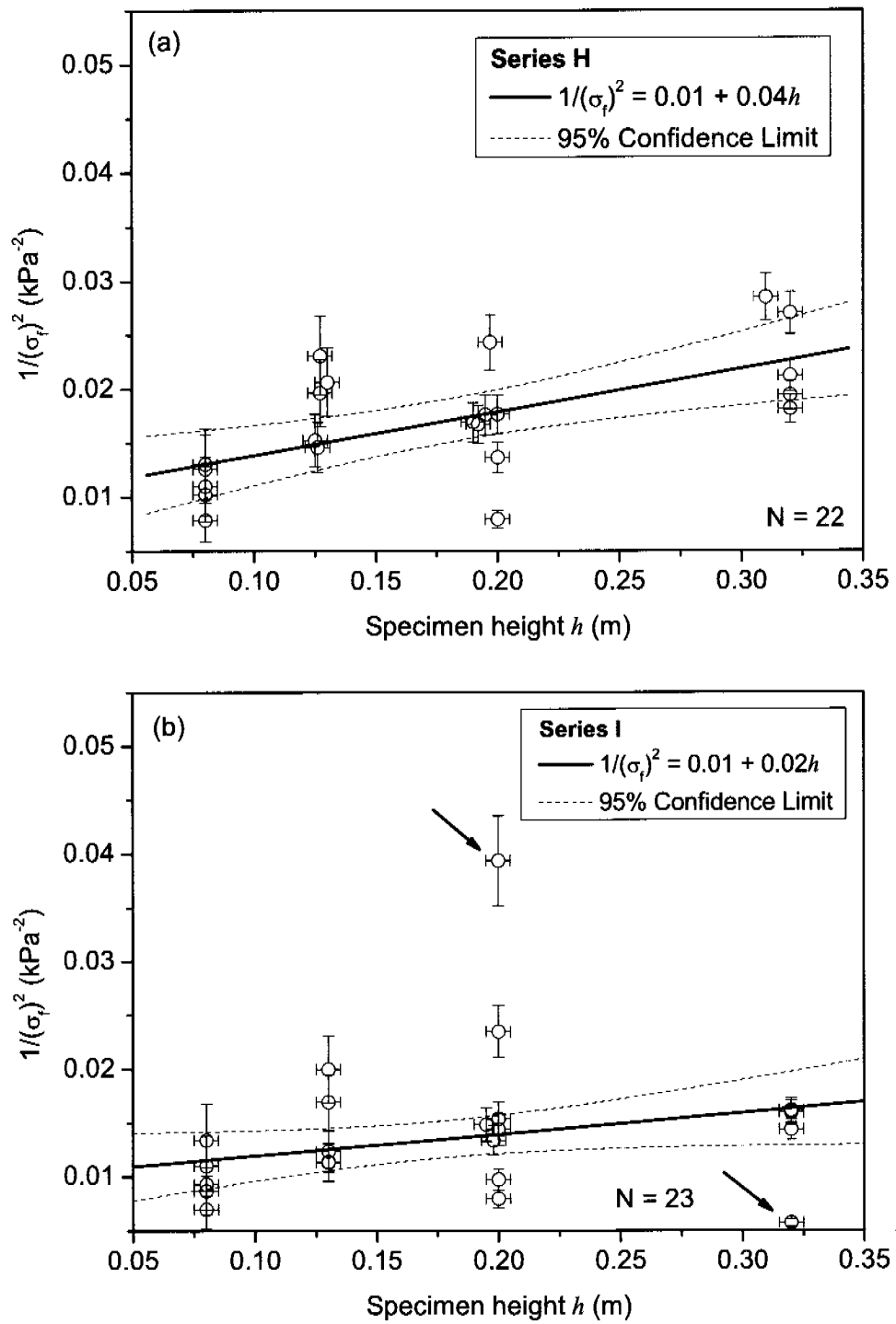


Figure 4.6: The inverse of the square of the nominal strength σ_f in relation to the specimen height (a) for Series H, and (b) for Series I.

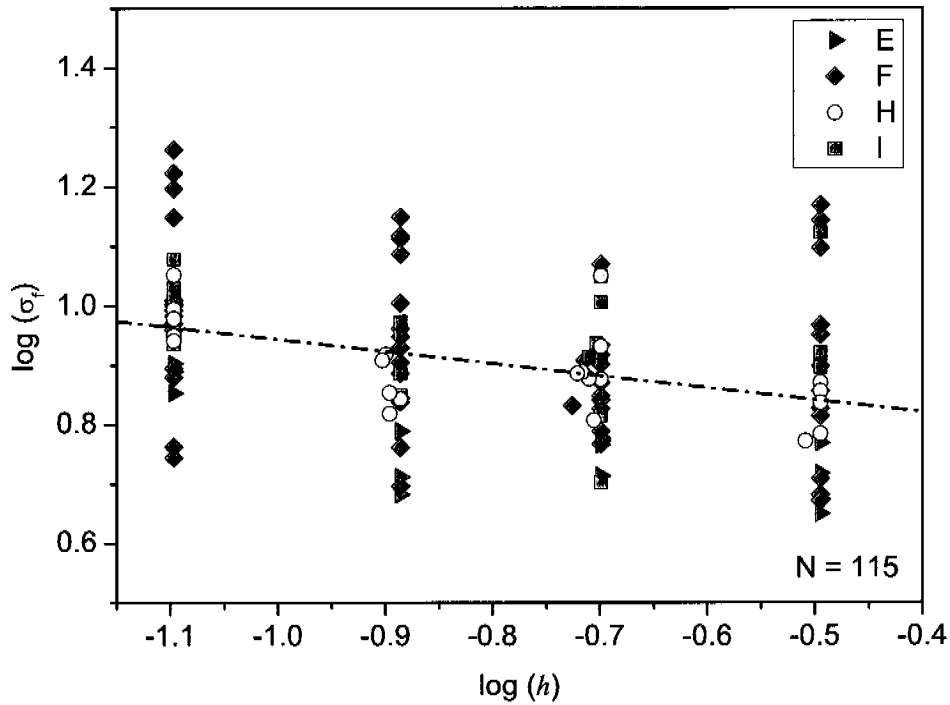


Figure 4.7: The logarithm of the nominal strength σ_f plotted against the logarithm of the specimen height h for series E, F, H and I. The dash-dotted line is a linear regression to the data.

of $-1/2$ corresponding to the specimen size range in which LEFM would be applicable (Figure 2.4).

With the mean value for the characteristic size \bar{D}_0 and Equation (2.28) a correction function can be found to determine the size independent equivalent fracture toughness K_{Ic}^e depending on the measured K_{If} values:

$$K_{Ic}^e = \sqrt{1 + \frac{0.29}{D}} K_{If}. \quad (4.5)$$

Using this function, the K_{If} results of the 3PB-tests of series A to I were corrected to the according K_{Ic}^e values. In Figure 4.8 the K_{Ic}^e as well as the K_{If} values are presented in relation to snow density. For the corrected data a power-law fit resulted in $A = (7.03 \times 10^{-6} \pm 7.25 \times 10^{-6}) \text{ kN m}^{3/2} \text{ kg}^{-1}$ and $B = 2.33 \pm 0.18$ with an $R^2 = 0.59$. The relation between K_{Ic}^e and density can thus be written as

$$K_{Ic}^e = 7.03 \times 10^{-6} \rho^{2.33} \text{ kPa}\sqrt{\text{m}}. \quad (4.6)$$

Table 4.3: The characteristic size D_0 for the four series E, F, H and I. The coefficients c_1 and c_2 are intercept and slope of a linear regression in a σ_f^{-2} versus h diagram. R^2 is the coefficient of determination and P is the level of significance of the linear regression.

Series	Number of tests	Snow density (kg/m ³)	c_1 (m ⁴ /N ²)	c_2 (m ³ /N ²)	D_0 (m)	R^2	P
E	17	186 ± 12	0.020 ± 0.005	0.066 ± 0.024	0.30 ± 0.13	0.34	0.015
F	53	310 ± 19	0.011 ± 0.003	0.034 ± 0.015	0.32 ± 0.17	0.09	0.031
H	22	239 ± 9	0.010 ± 0.002	0.040 ± 0.011	0.25 ± 0.09	0.39	0.002
I	23	256 ± 19	0.010 ± 0.002	0.020 ± 0.010	0.50 ± 0.27	0.18	0.059

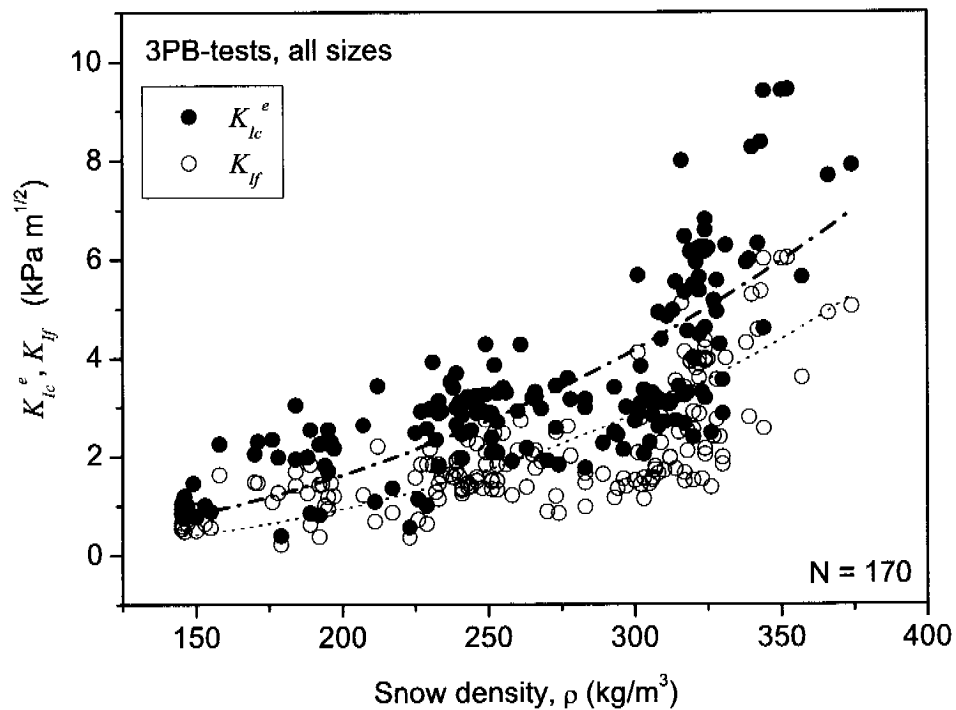


Figure 4.8: The critical SIF, K_{If} , and the critical SIF corrected to an equivalent fracture toughness, K_{Ic}^e , in relation to snow density. Only three-point bending (3PB) test are presented but the results for all four specimen sizes are included. The dash-dot line is the best fit for the K_{Ic}^e to density relation (Equation 4.6). The dotted line is the fit for K_{If} (Equation 4.2).

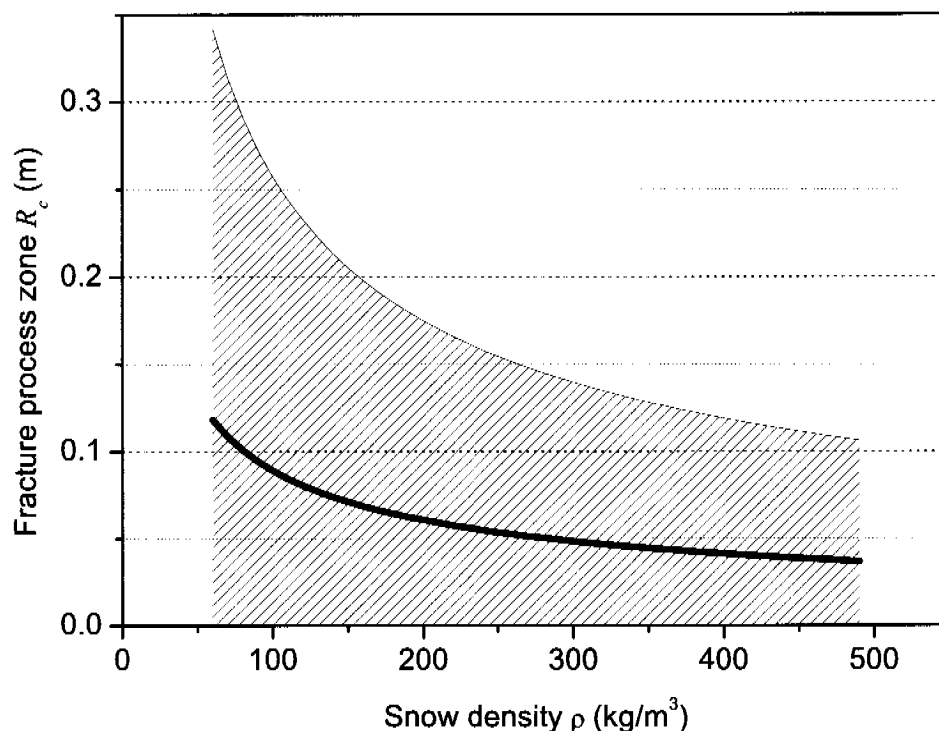


Figure 4.9: Size of the fracture process zone for snow in relation to snow density. The black line indicates the mean size for a given density and the dashed area the standard error.

4.1.6 Fracture process zone

If the tensile strength σ_c and the fracture toughness K_{Ic} are known, the size of the fracture process zone R_c can be estimated according to Equation (2.20). Since we have evaluated both, σ_c and K_{Ic}^e the size of the process zone can be calculated from the tensile strength to density relation (Equation 4.1) and the relation for the equivalent fracture toughness K_{Ic}^e to density (Equation 4.6). Figure 4.9 shows that the size of the fracture process zone R_c was between 12 cm and 4 cm depending on the snow density. The standard error can be calculated out of the errors for the fit parameters A and B according to the rules of error propagation. The standard error is indicated by the dashed area in Figure 4.9. A slight trend can be seen, that the size of R_c decreases with increasing density.

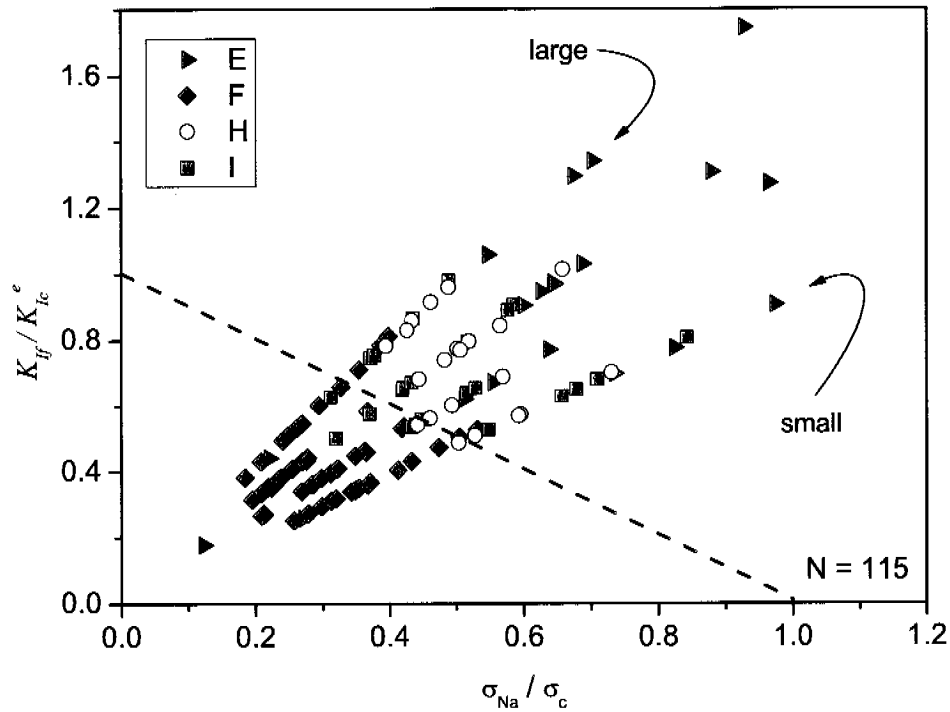


Figure 4.10: Failure assessment diagram (FAD) for the 3PB-test results for four different specimen sizes.

4.1.7 Application of the failure assessment diagram

With the measured tensile strength, σ_c , and the calculated equivalent fracture toughness values, K_{Ic}^e , a failure assessment diagram can be calculated (Section 2.4.3). The critical stress intensity factor, K_{If} , was divided by K_{Ic}^e and plotted against the effective stress σ_{Na} divided by the tensile strength σ_c .

The effective stress σ_{Na} of a 3PB-specimen is similar to the nominal stress σ_N (Equation 3.3) of the remaining cross section $(h - a)$. Assuming for the sake of simplicity – as common in FAD-application – an ideal plastic stress distribution in the ligament, the elastic stress given by Equation (3.3) is reduced by a factor of 2/3, thus

$$\sigma_{Na} = \frac{1}{(h - a)^2} \left[\frac{F_c s}{w} + \frac{1}{2} h \rho g [s^2 - (l - s)^2] \right]. \quad (4.7)$$

Figure 4.10 shows our data in a K_{If}/K_{Ic}^e over σ_{Na}/σ_c plot. For every 3PB experiment

Table 4.4: Fracture speed, captured with a high-speed camera in 3PB tests.

Test	Time resolution (pps)	Snow density (kg/m ³)	Specimen size (<i>l</i> , <i>h</i> , <i>w</i>) (cm)	Max. fracture speed $v_{I,max}$ (m/s)
1	115	266	(50, 20, 10)	8.4 ± 0.8
2	230	252	(50, 20, 10)	14.0 ± 1.6
3	460	278	(50, 20, 10)	13.6 ± 3.3
5	230	277	(80, 32, 10)	19.1 ± 1.6
6	460	255	(80, 32, 10)	22.7 ± 3.3

K_{I_f} and σ_{Na} were determined. Then the corresponding value of $K_{I_c}^e$ was calculated according to Equation (4.6) and the σ_c value according to Equation (4.1). Since the shape of a FAD curve – indicating the interaction between local and global failure of the structure – is not known for snow, the simplest version, a straight line between $K_{I_f}/K_{I_c}^e = 1$ and $\sigma_{Na}/\sigma_c = 1$ was assumed, indicated by the dashed line in Figure 4.10. The data points form four distinct lines. The four lines correspond to the data of the four different specimen sizes. The results of the largest specimen size form the most upper line, indicated as "large" in Figure 4.10, whereas the results of the smallest specimen size form the lowest line ("small"). Each line is the result of the large scattering of the experimental results. The points where the potential FAD (dashed line) intersects with the data lines coincide approximately with the mean value of each data line.

The larger the specimen is, the larger is the amount the crack front, i.e. the local processes acting at the crack tip, contribute to the failure of the whole specimen. The smaller the specimen, the more the global stresses contribute to specimen failure.

4.1.8 Fracture speed in mode I

Seven 3PB tests of series I were recorded with a high speed camera. Five of these seven image series could be evaluated. In the remaining two series, the point when fracture started was not captured. The results of the five experiments are listed in Table 4.4. Different image rates of 115 pps, 230 pps and 460 pps were used for recording. Best results were achieved with an image rate of 460 pps. However, high resolution resulted in a short recording time of approximately 1s, making it difficult to manually trigger the camera at the right time.

Figure 4.12 shows a sequence of six images recorded with an image resolution of 460 pps. Every third image was printed in Figure 4.12, this corresponds to a time difference of 6.5 ms between two images. The specimen size was 80 cm × 32 cm × 10 cm. On the first image (top left) the notch is visible that was made with a saw previous to testing. In image two to six a fracture is propagating from the notch upwards in direction of the loading cylinder which can be seen at the upper image boarder. The fracture speed

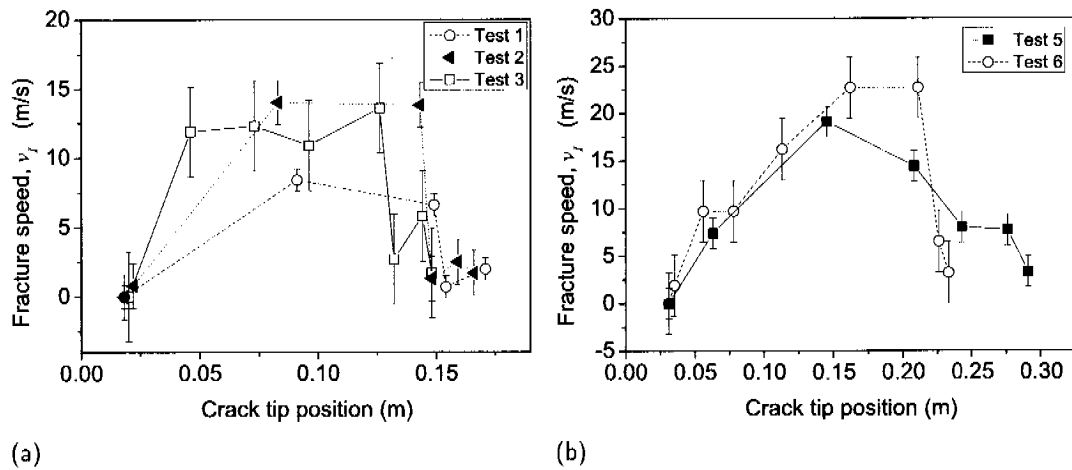


Figure 4.11: Evolution of the crack speed in relation to the crack depth for (a) Test 1 to 3 with a specimen size of 50 cm \times 20 cm \times 10 cm, and for (b) Test 5 and 6 with a specimen size of 80 cm \times 32 cm \times 10 cm.

for the mode I fracture, v_I , was measured by identifying the crack tip on successive images, calculating the crack advance between the two images and multiplying by the image resolution. Figure 4.11a shows the evolution of the crack speed in relation to the position of the crack in the specimen for the three tests with a specimen dimension of 50 cm \times 20 cm \times 10 cm and 4.11b for the two specimens with a dimension of 80 cm \times 32 cm \times 10 cm. The fracture speeds increase until a certain crack depth and decrease again after that point. The maximum fracture speeds $v_{I,max}$ are summarized in Table 4.4.

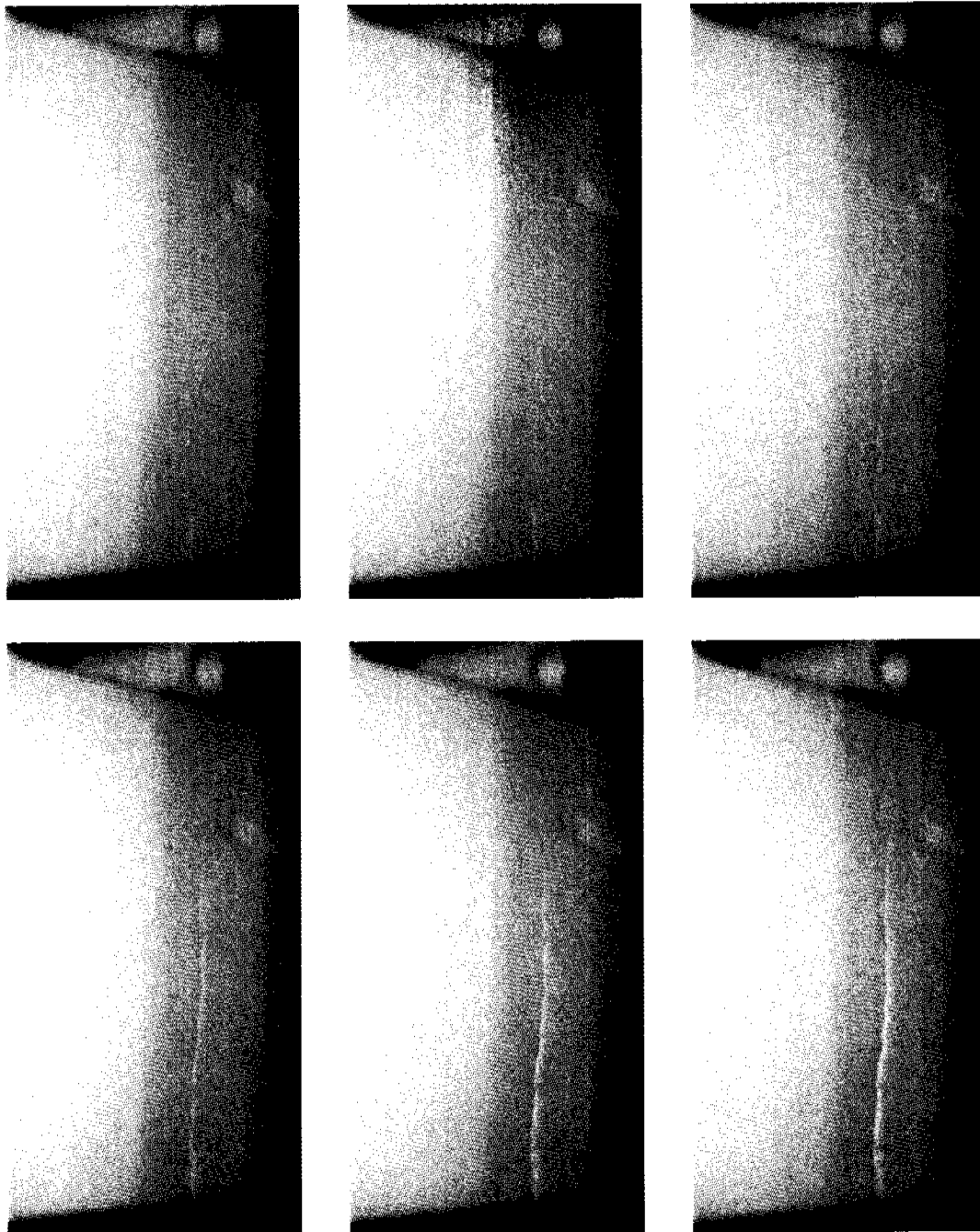


Figure 4.12: Crack propagation sequence recorded with a high-speed camera during a 3PB-test (Test 6, Table 4.4). The time difference between the images shown is 6.5 ms. The fracture process was recorded with an image rate of 460 pps.

4.2 Fracture in layered snow samples

After assessing the fracture behaviour of snow under tensile loading, we focussed on fracture mechanical experiments in shear. In contrast to previous shear fracture experiments by Kirchner et al. (2002a,b) who performed experiments with homogeneous snow samples, we focused on layered snow samples. First, because shear fracture processes in avalanche release always occur between different snow layers of different snow type and second, because shear fractures in homogeneous materials tend to kink off, resulting in a pure tensile failure (see Section 2.5). Because our main interest was to determine, if a fracture can propagate or not, and not the determination of the stress field around the crack tip, and in order to avoid the complexities of a determination of interfacial stress intensity factors $K^{int} = K_1 + i K_2$, the focus was set on the energy release rate G , instead (Section 2.5.1). Consequently, the determination of the Young's modulus, E , of a given layer in the snowpack was of prime importance, because the Young's modulus was used to determine the energy release rate G (Equation 2.32).

4.2.1 Tested weak layers

During winter 2004/2005 four series (2A-2D) of shear fracture tests were performed (Table 4.5). The specimens were fixed to an aluminium bar so that the weak layers could be tested vertically in a simple cantilever beam experiment (Section 3.2.4). In all series a weak layer was detected by compression tests, observed in a manual snow profile and recorded with the SMP. Figure 4.13 shows that weak layers corresponded to a local minimum in the SMP penetration resistance signal. Weak layers typically consist of snow types with low hardness, resulting in a low penetration resistance. In Figure 4.13 one example of the penetration resistance profile is given for each of the four series. With exception of series 2B, the tested weak layers correspond to the lowest penetration resistance in the profiles. The weak layers had in most cases a hand hardness index (Fist) that was one step lower than the adjacent layers (Four-fingers to One-finger). For series 2B, the weak layer was adjacent to a crust. Details on the different series and the weak layer types can be found in Table 4.5.

The mean critical cut depth a_c was 0.39 ± 0.05 m, resulting in a mean ligament size at failure, $b_c = (l - a_c)$, of 0.08 ± 0.03 m, where l was the specimen height. The mean thicknesses of the two layers t_1, t_2 were: $t_1 = 0.11 \pm 0.02$ m, $t_2 = 0.09 \pm 0.02$ m (Figure 3.5).

27 experiments were performed in total. The experiments were difficult to perform due to the fragile nature of the layered snow beams. Up to 20% of the experiments failed before the fracture test could be performed. The main failure sources were the transport to the laboratory, the fixation at the aluminium bar and the placing of the snow specimen attached to the aluminium bar in the test position. The failures that occurred involved either a failure of the weak layer or the breaking off of a part of the beam vertical to the

Table 4.5: Summary of shear fracture experiments. Snow type is given as grain shape, grain size and hardness index according to ICSSG (Colbeck et al., 1990). "Upper layer" denotes the layer above the weak layer and "lower layer" the layer underneath the weak layer according to their position in the snow cover.

Series	Date of sampling	Number of experiments	Snow temp. ($^{\circ}$ C)	Compression test results Number of tabs (rating)	Grain shape, grain size - upper layer - weak layer - lower layer	Hardness index	Snow density \pm sdev (kg/m^3)
2A	24 Feb 05	8	-9.1	12, 12, 12 (moderate)	Faceted crystals, 0.5 – 1 mm	4F-1F	267 \pm 5
					Faceted crystals and some surface hoar, 0.75 – 1.5 mm	F-4F	
2B	24 Feb 05	2	-8.7	12, 12, 14 (moderate)	Faceted crystals, 0.75 – 1 mm	1F	275 \pm 11
					Faceted crystals, 0.75 – 1 mm	1F	309 \pm 5
2C	15 Mar 05	10	-9.1	13 (moderate)	Small rounded and some faceted crystals, 0.5 – 1 mm	4F	234 \pm 10
					Mixed forms and some depth hoar, 0.75 – 1.5 mm	F	
2D	15 Mar 05	7	-9.1	21 (hard)	Mixed forms, 0.5 – 1 mm	4F	267 \pm 10
					Small rounded and mixed forms, 0.5 – 75 mm	1F	330 \pm 6
					Mixed forms and some surface hoar, 1 – 2 mm	F	
					Small rounded and mixed forms, 0.5 – 75 mm	1F-K	348 \pm 7

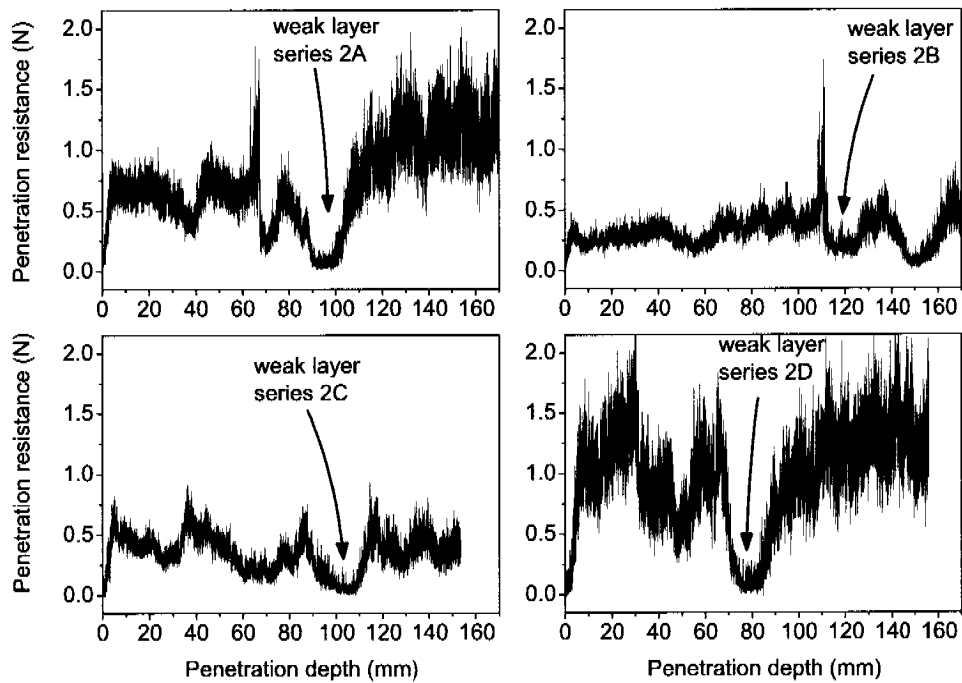


Figure 4.13: Penetration resistance recorded with a SnowMicroPen SMP. For each of the four tested weak layer types, series 2A to 2D, one example is given. With the exception of series 2B, the tested weak layers correspond to the lowest penetration resistances in the profiles.

layering.

4.2.2 Young's modulus

After performing fracture tests, small samples were cut out of the different layers of the tested specimens. A dynamic Young's modulus of these samples was then measured in a cyclic loading experiment (see Section 3.4.1). Due to the time consuming measurement technique, the Young's modulus could not be determined for each specimen that had been tested in fracture. Each specimen would have required two measurements, one for the upper layer and one for the lower layer. A selection of 27 measurements was made: 10 in series 2A, 2 in series 2B, 9 in series 2C and 6 in series 2D. The dynamic Young's modulus, E_{dyn} , of these 27 experiments are shown in Figure 4.14. E_{dyn} is plotted against

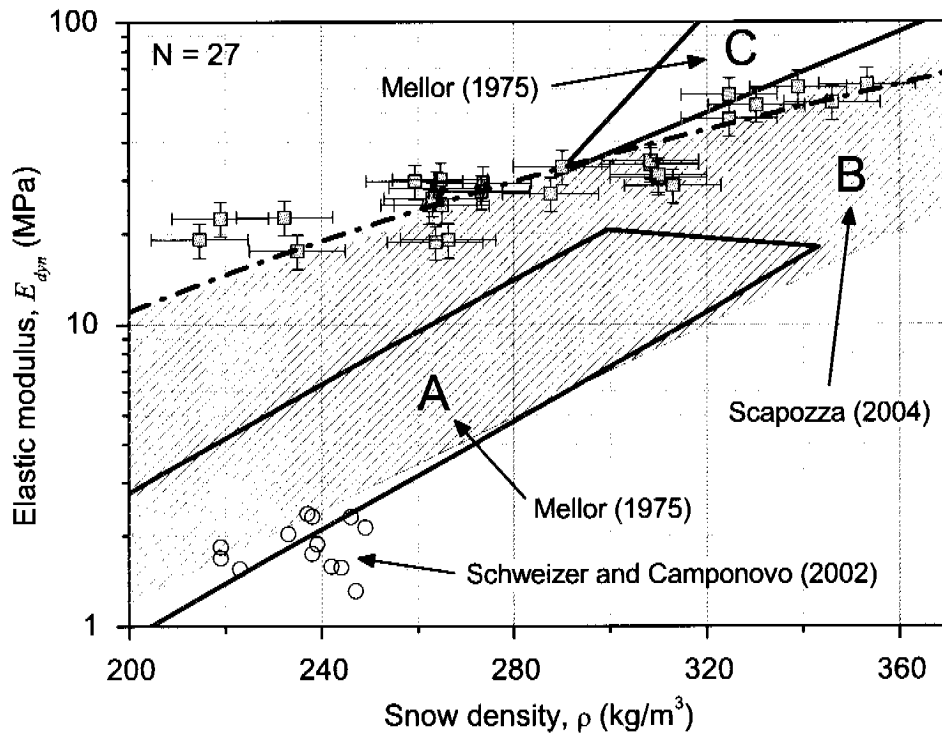


Figure 4.14: Dynamic Young's modulus in relation to snow density, measured at a frequency of 100 Hz (squares). The dash-dot line indicates the best fit of the data (Equation 4.9). The dashed area (B) indicates the range of the Young's modulus found by Scapozza (2004) in quasistatic compression experiments. (A) are uniaxial compression and tension experiments compiled by Mellor (1975) and (C) pulse propagation or flexural vibration tests at high frequencies, also compiled by Mellor (1975). Additionally, the results of the dynamic torsional shear experiments of Schweizer and Camponovo (2002) were converted to Young's modulus values (circles).

snow density. A power law relation can be fitted to the data:

$$E_{dyn} = 1.89 \times 10^{-6} \rho^{2.91} \text{ MPa}, \quad (4.8)$$

with a coefficient of determination of $R^2 = 0.80$. The power law relation is indicated as dash-dot line in Figure 4.14. (An exponential relation resulted in: $E_{dyn} = 2.71 e^{0.0085\rho}$ MPa, $R^2 = 0.78$). For comparison, the range of results summarized by Mellor (1975) (area A and C) and by Scapozza (2004) (dashed area B) are added to Figure 4.14. Furthermore, the results obtained by Schweizer and Camponovo (2002) are added. They determined the shear modulus, S , in dynamic torsional shear experiments

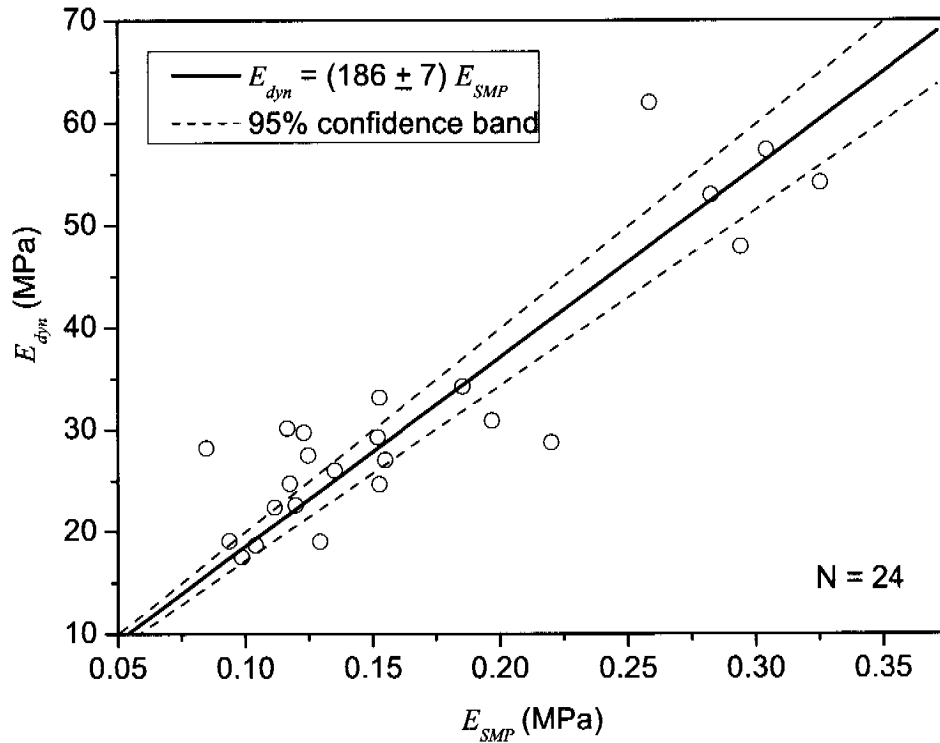


Figure 4.15: Correlation of the dynamically measured Young's modulus E_{dyn} with the index E_{SMP} derived from the penetration resistance signal, recorded with the SnowMicroPen SMP.

with a rheometer. The shear modulus results of Schweizer and Camponovo (2002) were converted to Young's modulus values according to the relation for linear elastic material behaviour: $E = 2S(1 + \nu)$. The Poisson's ratio ν was set to 0.17 for the snow densities of about 230 kg/m^3 they used for their experiments.

Alternatively, the SMP penetration resistance signal was used to estimate the Young's modulus. The big advantage of this method is that an SMP signal is easy and fast to acquire, the disadvantage is that the conversion from penetration resistance to Young's modulus is badly calibrated up to now. An IDL (Interactive Data Language) algorithm, developed by Kronholm (2004) and based on a theory of Johnson and Schneebeli (1999), was used to calculate an index for the Young's modulus as a function of the penetration resistance (Equations 3.19 and 3.20). However, according to Kronholm (2004), the values of the index derived from the SMP signal are too small and have to be corrected by a factor of about 150 to get an appropriate estimate for the Young's modulus.

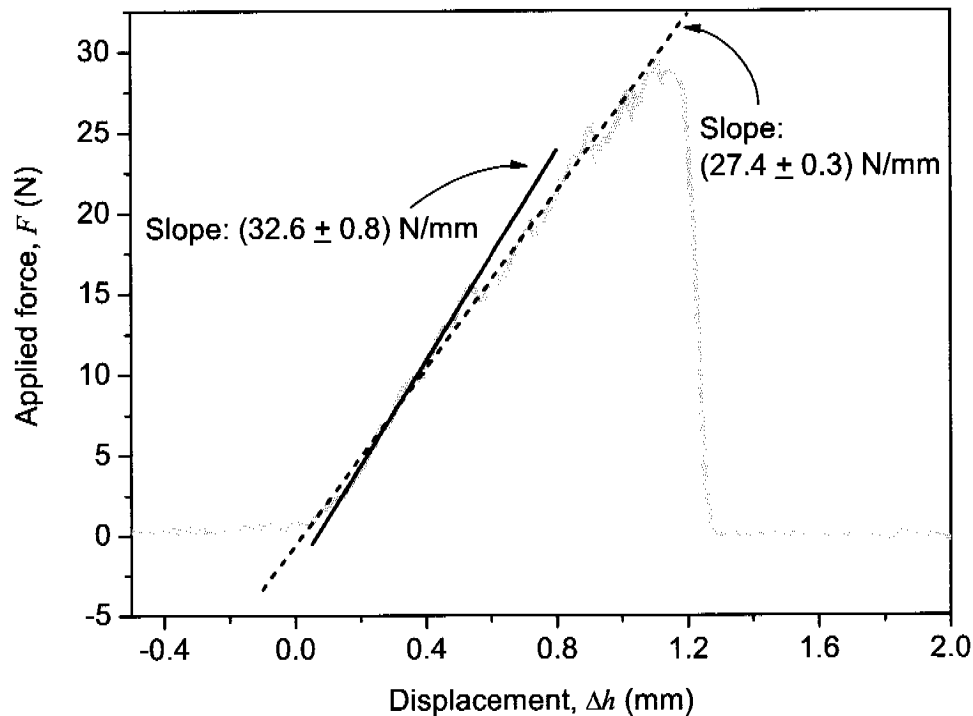


Figure 4.16: Force-displacement diagram of a three-point bending test. (Specimen dimensions: 50 cm × 20 cm × 10 cm, density: 240 kg/m³). Indicated are the slopes ($F/\Delta h$) of an initial tangent (black line) and of a tangent over the whole range where the force increases (black dashed line).

Correlating the index values derived from the SMP data, E_{SMP} , with the results from the cyclic loading tests, E_{dyn} , resulted in a correction factor of $E_{dyn} = (186 \pm 7) E_{SMP}$ with a coefficient of determination of $R^2 = 0.81$ and a level of significance $P < 0.0001$ (Figure 4.15). Of the 27 measurements with the cyclic loading device only for 24 an SMP signal was available. Therefore, Figure 4.15 includes only 24 data points.

A further possibility to estimate the Young's modulus would be to use the force-displacement signals acquired during the three-point bending tests. Out of a force-displacement diagram the slope of the force increase ($F/\Delta h$) can be determined (Figure 4.16). By multiplying this slope with h/A the elastic modulus can be determined according to

$$E = \frac{\sigma}{\varepsilon} = \frac{F}{A} \frac{h}{\Delta h}, \quad (4.9)$$

where h is the height of the specimen and A the area of contact of the force sensor. The height of the specimen in Figure 4.16 was 20 cm and the area of contact is given by the width of the beam (10 cm) times the width of the contact of the force cylinder. The contact width is assumed to be approximately 1 cm. The resulting Young's modulus for the indicated slopes of $F/\Delta h = 27.4$ N/mm and of $F/\Delta h = 32.6$ N/mm are

$E = 5.5 \text{ MPa}$ and $E = 6.5 \text{ MPa}$, respectively. The specimen in Figure 4.16 had a density of 240 kg/m^3 . Compared to the Young's modulus results compiled in Figure 4.14, the values are well within the range of the results of Mellor (1975) and Scapozza (2004).

However, in a three-point bending test the displacement Δh is a combination of compression of the specimen and bending of the specimen. Only the compression is relevant for the determination of the Young's modulus. Since in the above estimate both components are included the effective Young's modulus might be underestimated.

4.2.3 Energy release rate in mode II

To evaluate the critical energy release rate G_f for our experiments, no analytical solution was found. Therefore, G_f was determined numerically in an FE simulation (Section 3.2.5). The critical energy release rate is denoted as G_f in this work and not as G_c , as it is usually done in literature, because index f expresses that the energy release rate will most probably depend on the test specimen size (compare with K_{If} vs. K_{Ic} in Section 4.1.5).

For every single experiment an FE simulation was run based on the exact geometry of the experiment. The input parameters were: specimen length, thickness and width (l, t_t, t_b, w), elastic properties of the two layers (E_t, E_b, ν_t, ν_b), density of the two layers (ρ_t, ρ_b) cut length at failure (a_c), as well as angle of rotation (α) and the additional mass (m_{load}). The Poisson's ratio ν_t, ν_b were estimated from density according to

$$\nu = \nu_0 + (\rho - \rho_0) 5 \times 10^{-4} \text{ m}^3/\text{kg}, \quad (4.10)$$

with $\nu_0 = 0.2$ and $\rho_0 = 300 \text{ kg m}^{-3}$ according to Mellor (1975). The cut length increment Δa was set to 0.002 m resulting in $\Delta a/h = 0.004$. Changes in Δa did not change the energy release rate G . The Young's modulus of the slab (E_t) and the basal layer (E_b) as well as of the weak layer (E_{WL}) were derived from the SMP penetration resistance signal. This was done by dividing the penetration resistance signal (compare Figure 4.13) in three sections: slab, weak layer and basal layer. In the following the Young's modulus was derived as average over a whole section, even if the penetration resistance signal showed variations in one section. The results are compiled in Table 4.6.

Since the crack length a was set equal to the critical crack length a_c the energy release rate at the point of failure was assessed. The energy release rate at failure is equal to the critical energy release rate G_f , the energy that has to be overcome to propagate a fracture. G_f can thus also be seen as the specific fracture energy of the weak layer, the energy needed to fracture a weak layer over a unit area.

The results for the critical energy release rate G_f for the different series (2A-2D) are shown in Figure 4.17. G_f is plotted against various elastic properties of the specimen. Only for the correlation of G_f with the elastic mismatch between slab and basal layer, E_t/E_b , a slight trend to increase with increasing elastic mismatch could be observed

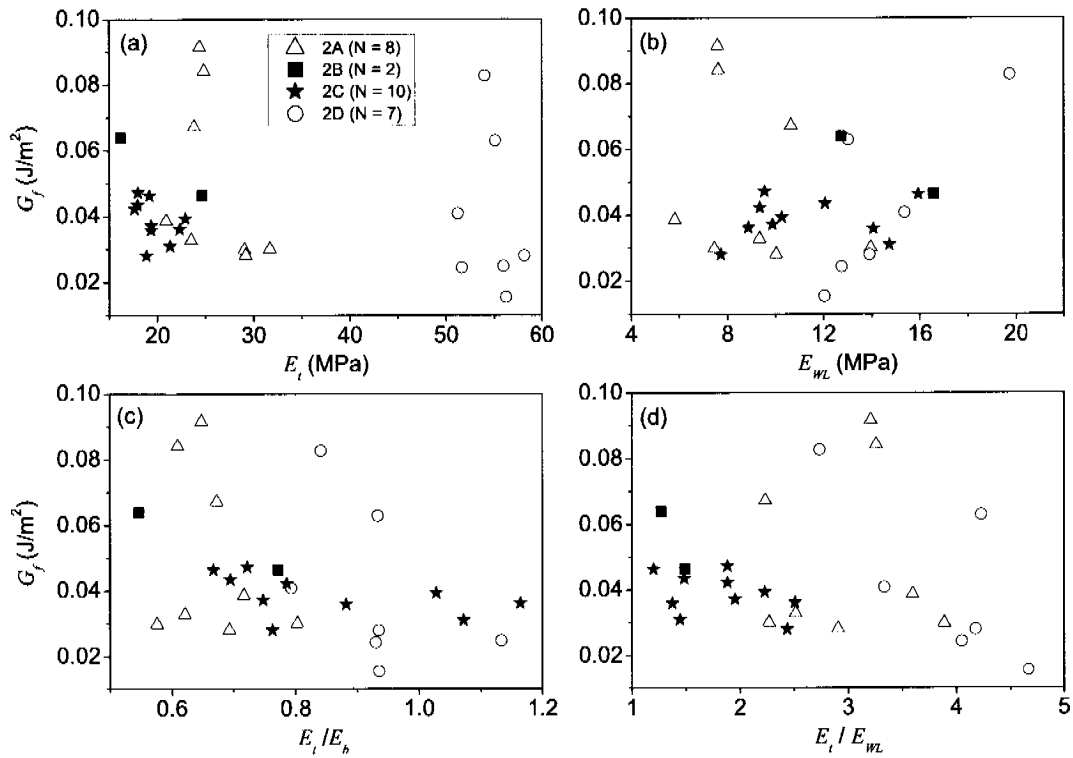


Figure 4.17: Critical energy release rate G_f in relation to the elastic properties of the specimen: (a) G_f in relation to the Young's modulus of the slab E_t , (b) in relation to the Young's modulus of the weak layer E_{WL} , (c) in relation to the elastic mismatch of slab and basal layer E_t/E_b , (d) in relation to the elastic mismatch of slab and weak layer E_t/E_{WL} . The results are coded according to the four series of winter 2004/2005 (Table 4.5).

Table 4.6: Details of the shear fracture experiments.

Series	Relative cut length, a_c/l	Thickness ratio, t_t/t_b	Young's modulus			G_f (mJ/m ²)
			E_t (MPa)	E_{WL} (MPa)	E_b (MPa)	
2A	0.85 ± 0.05	0.96 ± 0.15	25.9 ± 3.6	9.1 ± 2.5	39.1 ± 6.0	50 ± 26
2B	0.80 ± 0.08	0.88 ± 0.01	20.4 ± 6.0	14.6 ± 2.7	30.8 ± 1.7	55 ± 12
2C	0.78 ± 0.07	1.21 ± 0.53	19.7 ± 1.9	11.2 ± 2.8	23.6 ± 2.9	39 ± 6
2D	0.82 ± 0.08	1.26 ± 0.63	54.6 ± 2.5	14.5 ± 2.8	59.3 ± 5.4	40 ± 24

($P(4.17a) = 0.49$, $P(4.17b) = 0.04$, $P(4.17c) = 0.61$, $P(4.17d) = 0.49$). However, if the four data points in Figure 4.17c were excluded, for which the Young's modulus of the slab was bigger than of the basal layer $E_t/E_b > 1$ no statistically significant correlation could be observed ($P = 0.36$). The exclusion of these four points from a correlation is justified because the elastic mismatch starts to increase again for $E_t/E_b > 1$, after decreasing in positive x -direction for $E_t/E_b < 1$. Figure 4.17b suggests that the energy release rate does not depend on the Young's modulus of the weak layer. However, the range of the Young's modulus for the weak layers tested in our experiments was relatively narrow, since the properties of the weak layers were similar for all series (Table 4.5). A multiple regression for G_f and the Young's modulus of E_t , E_b and of the weak layer E_{WL} did not reveal any statistically significant correlation ($R^2 = 0.15$, $N = 26$, $P = 0.15$).

The mean critical energy release rate for all series was

$$G_f = 0.044 \pm 0.020 \text{ J/m}^2. \quad (4.11)$$

4.2.4 Comparison of analytical approaches to FEM results

To determine the energy release rate G for our experimental geometry no analytical solution was available. Therefore, we adapted two general analytical approaches to determine G . To overcome some of the limitations of the analytical solutions we compared them to a numerical approach. In the following, the two approaches are described: (1) The analytical cantilever beam approach is valid for deep cracks but assumes a homogeneous material, see Section 3.2.4. (2) The analytical bilayer approach assumes two different materials, but an infinitesimally extended specimen, see Section 2.5.2. An analytical solution is of importance, even if it is an approximation, because it can render FE modelling unnecessary for future experiments.

Figure 4.18a compares the cantilever deep crack approach with the FEM results. Energy release rates were calculated according to Equations (3.7)-(3.9) and Equation (3.16) for different geometry and material properties. The cantilever results were larger than the FEM results, but the values were highly correlated ($R^2 = 0.93$, $N = 21$, $p < 0.0001$). The slope was 0.49 ± 0.03 . The value of the slope slightly depends on the elastic mismatch between slab and basal layer, E_t/E_b (Figure 4.18c). A linear regression showed a level of significance of $P = 0.003$.

The analytical solution of Suo and Hutchinson (1990) for an interface crack between thin films, Equation (2.33), was adapted to our geometry. For our geometry and loading situation $h = t_t$, $H = t_b$ and we assume P_1 to be the force due to the body weight plus the additional weight that was placed on top of the protruding part, therefore, $P_1 = P_3 = P_{CB}$ in Equation (3.14). P_2 was zero, M_1 was equal to M_{CB} (Equation 3.16). M_3 was zero because the specimen was placed on the table at the point where M_3 would act. With these assumptions Equation (2.33) simplified to

$$G = \frac{1}{2E_t} \left(\frac{P_{CB}^2}{t_t} + 12 \frac{M_{CB}^2}{t_t^3} \right) + \frac{1}{2E_b} \left(-\frac{P_{CB}^2}{At_t} + 12 \frac{M_2^2}{t_b^3} \right). \quad (4.12)$$

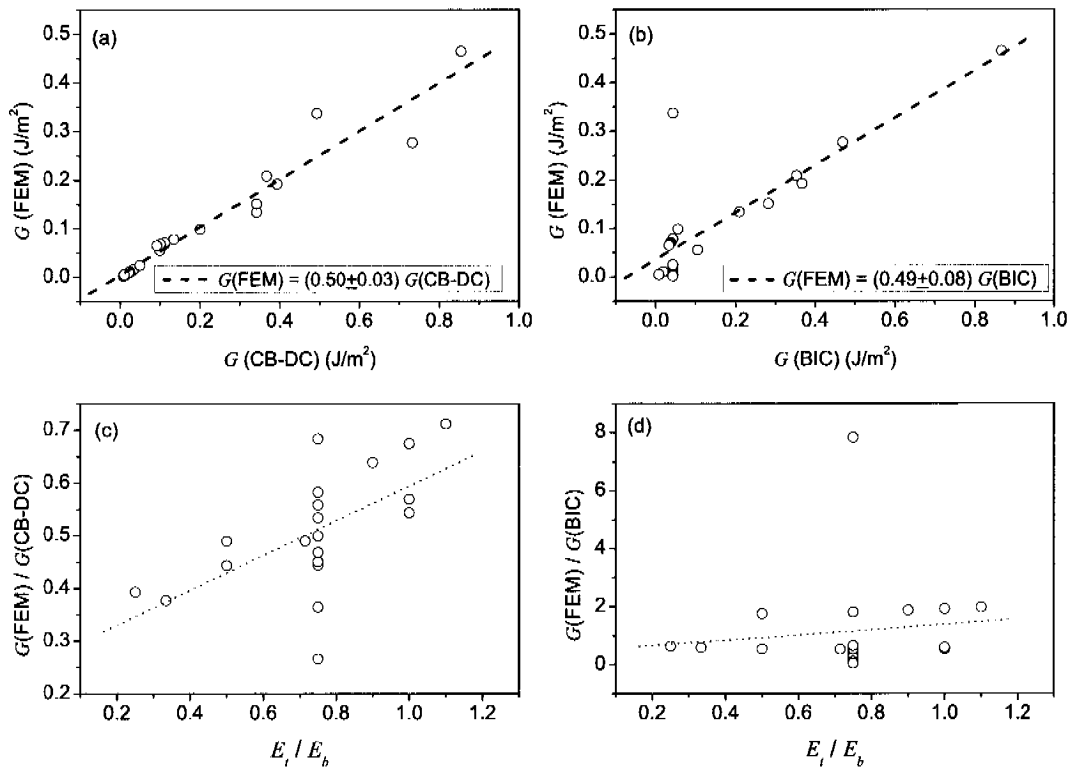


Figure 4.18: Comparison of the energy release rates obtained with the FE model and (a) the analytical deep crack cantilever approach, and (b) the analytical bilayer with an interface crack approach. Figures (c) and (d) show the ratio of the energy release rates in relation to the elastic mismatch E_t/E_b for the two analytical solutions. ($N = 21$).

Overall equilibrium of moments provides a constraint so that the moment M_2 can be calculated:

$$M_2 = P_{CB} \left(\frac{t_t}{2} + t_b - \Delta t_t \right) + M_{CB}. \quad (4.13)$$

M_2 compensates for the fixed side of the beam in our experiments.

In Figure 4.18b the adapted analytical solution for a bilayer material (Suo and Hutchinson, 1990) is compared with the FEM results. The analytical results were larger than the FEM results. A linear regression resulted in a slope of 0.49 ± 0.08 ($R^2 = 0.69$, $N = 21$, $p < 0.0001$). Consequently, for the bilayer approach the slope did not depend on the elastic mismatch between slab and basal layer, E_t/E_b ($P = 0.62$), because E_t as well as E_b are included in the bilayer approach. (Figure 4.18d).

If the analytical solutions are multiplied with the according correlation factors, they are valuable solutions to replace the finite element modelling.

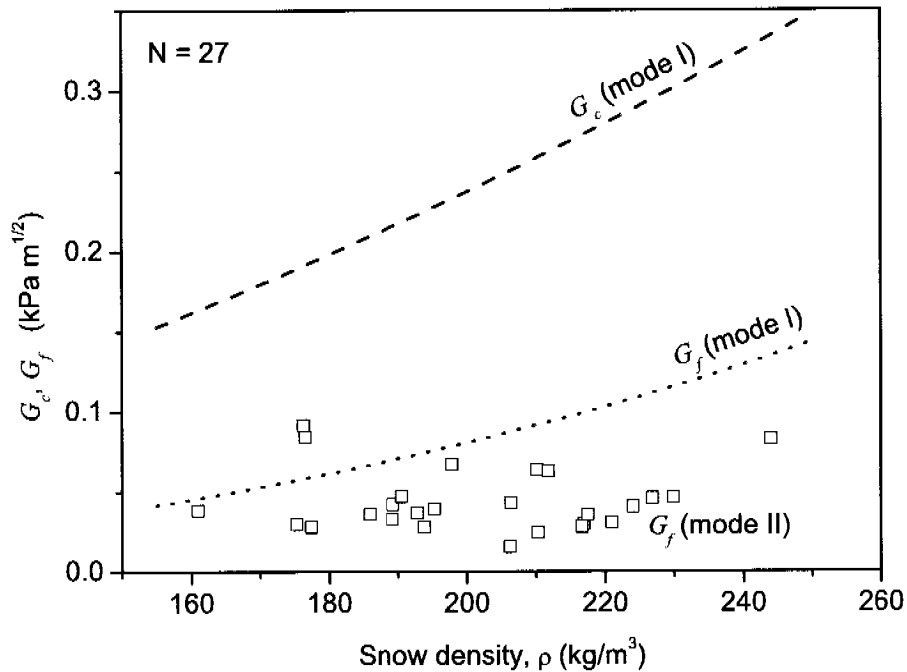


Figure 4.19: Critical energy release rate G_f of the mode II experiments (squares) in comparison to the critical energy release rate for the mode I experiments (dotted line) and the effective critical energy release rate in Mode I G_c (dashed line).

4.2.5 Comparison of mode I and mode II results

In order to compare the energy release rate of the mode I experiments and of the mode II experiments, Equation (2.17): $G = K^2/E$, can be used to transform the critical energy release rate results in mode I into an energy release rate in mode I. To get the critical energy release rate in mode I, $G_f(\text{mode I})$, in relation to the density, Equation (4.2) was used for the critical stress intensity factor K_{I_f} and Equation (4.9) for the Young's modulus. Figure 4.19 shows the resulting relation (dotted line). To get the specimen size independent effective critical energy release rate in mode I, $G_c(\text{mode I})$, in relation to the density, Equation (4.6) was used for the equivalent fracture toughness $K_{I_c}^e$ (dashed line). For the mode II experiments the density of the weak layer was estimated by converting the Young's modulus E_{WL} into a density for the weak layer by using Equation (4.9). The mode I critical energy release rate is on average 2.2 times higher than the critical energy release rate in mode II for the same density of snow. The effective critical energy release rate G_c is on average 6.5 times higher than the G_f in mode II.

On the other side, Equation (3.7) can be used to get a rough estimate of the magnitude

of the fracture toughness for our weak layer type: $\sqrt{G E_{WL}} = \sqrt{K_{I}^2 + K_{II}^2}$. The average weak layer Young's modulus E_{WL} of our samples was 11.6 MPa (Figure 4.17b). Corresponding to a density of about 200 kg/m³ if Equation (4.9) is used. The mixed mode interfacial critical stress intensity factor for a shear fracture along a weak layer, K_{II}^{int} , resulted in

$$K_{II}^{int} = 0.49 \pm 0.36 \text{ kPa m}^{1/2} \quad (4.14)$$

which is about a factor of 1.9 lower than the critical stress intensity factor in mode I, K_{I}^{int} , for samples of similar snow density (see Figure 4.3).

4.3 Fracture of weak layers on slopes

Field experiments were performed during three days between 25 January and 3 February 2006. For the test a snow beam including a weak layer was isolated on all four sides and then a cut was made along the weak layer with a snow saw until the specimen failed (Section 3.3 and Figure 4.20). An east-facing slope was selected with a slope angle close to 30° at Strela-Schönenboden, Davos, Switzerland (779 920 / 186 365). In this slope a weak layer was present in a depth of about 30 cm which consisted of faceted crystals and partly depth hoar. The weak layer was formed under a 2 mm thick crust during a period of fine weather in January 2006. Three test series were performed with this weak layer at intervals of 2 days and 7 days, respectively. Details of the tests can be found in Table 4.7 and in the stratigraphic snow cover profiles for the three days in Appendix B. 33 experiments were performed in these three days.

The tests can be divided in two groups according to their failure behaviour. The first group of snow beams failed along the entire weak layer plane after a critical cut length a_c was reached with the saw. Because most of our experiments were performed at a slope angle of about 30° , the detached part of the beam (the slab) did not slide down over the failed weak layer plane, but a noticeable displacement of the whole slab could be observed. A displacement of the upper part of the beam (slab) of approximately 5 mm can be observed in Figure 4.20c. The weak layer can be identified in the image as darker area due to higher porosity. In the second group, a fracture propagated along the weak layer when reaching a_c but the weak layer did not fail entirely. The crack was arrested after a certain distance. In some cases a vertical tensile crack could be observed through the overlying slab. Of the 33 experiments, the weak layer fractured entirely in 22 or two-thirds of all tested specimens and in 11 tests the crack was arrested.

Tests that were made on slopes steeper than 30° showed that the slab slid down over the plane of weakness. Tests on slopes with an inclination of about 25° showed that a similar displacement could be observed as in tests at 30° . Results of the tests with an other inclination than 30° are not further considered, because only few tests were made and the weak layers are not comparable to the other data set.

4.3.1 Shear strength of the tested weak layer

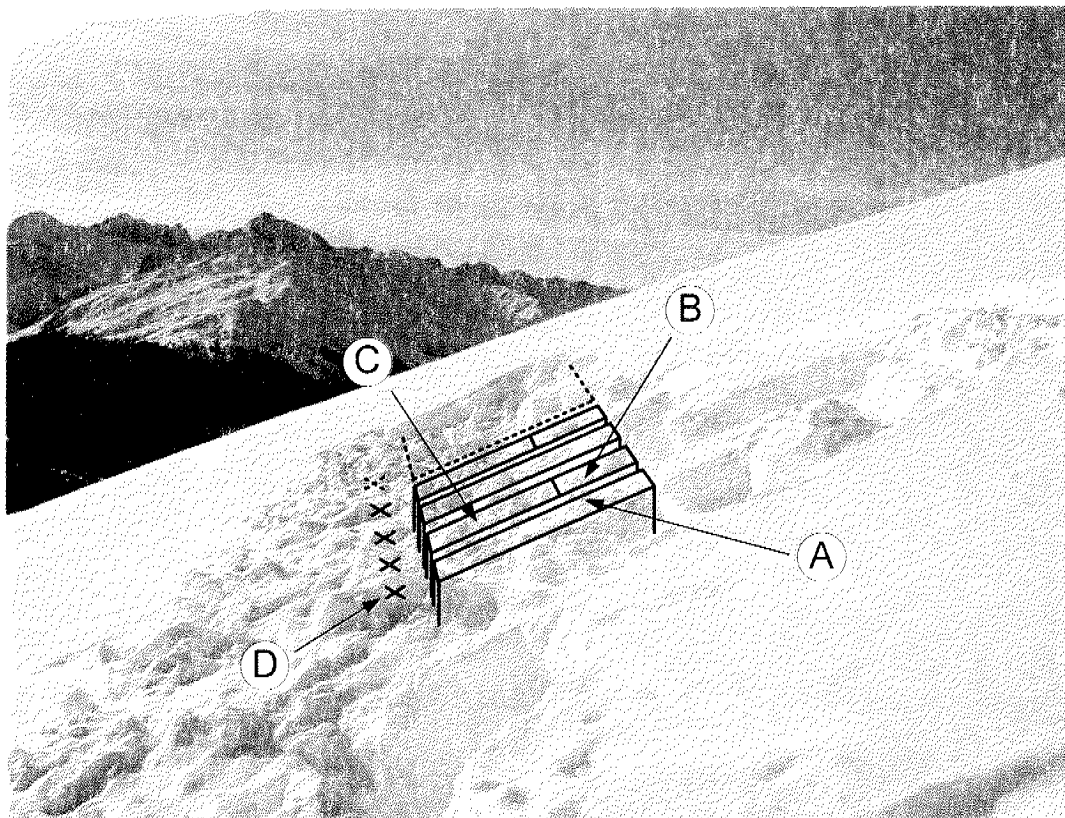
The shear strength measurements were performed with the shear frame (Section 3.1). The shear strength is calculated as the measured force divided by the shear frame area and multiplied with a correction factor (Jamieson and Johnston, 2001). The results of the shear strength measurements are summarized in Table 4.8.

The mean shear strength was between a factor of 3.4 and 5.4 higher than the effective shear stress. The effective shear stress is calculated as the slope parallel component of the load due to the weight ($m_{slab} g \cos(\varphi)$) divided by the base area of the isolated beam reduced by the area that had been cut with the snow saw ($w(l - a_c)$).

Table 4.7: Summary of the field experiments. Date of the field day and number of test are given. Snow type is given as grain shape, grain size and hardness index according to ICSSG (Colbeck et al., 1990).

Series	Date of testing	Number of experiments	Snow type of weak layer	Compression test results Number of tabs (rating)	Mean slab density (kg/m ³)	Mean slab thickness (slope normal) (m)	Snow / Air temperature (°C)
3A	25 Jan 06	5 (4/1) ^a	Faceted crystals and partly depth hoar, 1 – 3 mm, F	11, 11, 12 (moderate)	173	0.27	-6.9 / -3.2
3B	27 Jan 06	21 (13/8) ^a	Faceted crystals and partly depth hoar, 1 – 2 mm, F	13,13; 13,13; 14,12; 13,13; 15,14; 15,13 (moderate)	187	0.26	-7.4 / -9
3C	3 Feb 06	7 (5/2) ^a	Faceted crystals and depth hoar, 1 – 2.5 mm, F	14,15; 15,15; 16,17; 17,15,15 (moderate)	202	0.21	-6.3 / -3.5

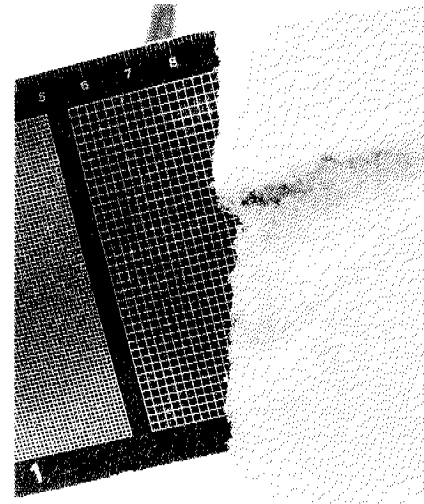
^a(Number of test in which the beam failed completely / Number of tests in which the crack was arrested)



(a)



(b)



(c)

Figure 4.20: (a) Image of the study site at Strela-Schönenboden, Davos after testing. It is schematically indicated how a row of field test beams was located. (A) Test specimen with length of 1.8 m followed by a beam divided in a (B) 0.6 m and a (C) 1.2 m beam. (D) Downslope of every test beam a SMP penetration resistance profile was taken. (b) Field test setup. Cutting along the weak layer of a field test specimen with length 1.2 m and width 0.3 m. (c) Lower edge of a test specimen. The failure of the weak layer resulted in a slight downslope displacement of the upper part of the beam (the slab) of about 5 mm.

Table 4.8: Data of shear frame measurements compared to the effective shear stresses.

Series	Number of shear frame tests	Mean force (N)	Mean shear strength (Pa)	Effective shear stress (Pa)
3A	11	51 ± 6	1540 ± 180	284 ± 16
3B	10	35 ± 6	1080 ± 170	315 ± 61
3C	8	49 ± 4	1440 ± 100	282 ± 11

4.3.2 Energy release rate for the tested weak layer

A finite element model (FEM) was used to determine the energy release rate for the tested weak layer (Section 3.3.1). Every field test was modelled with finite elements according to its specific geometry and snow properties. The following parameters were required as input for the model: length l and width w of the beam, thickness, density and elastic properties of the different layers of the slab (h_i, E_i, ρ_i) for $i = 1, \dots, n$, as well as for the basal layer ($h_{base}, E_{base}, \rho_{base}$), cut length at failure a_c , and the slope angle φ . The Poisson's ratio ν_i was estimated from density according to Equation 4.10. The cut length increment Δa was set to 0.002 m resulting in $\Delta a/h \leq 3 \times 10^{-3}$.

The Young's modulus for a given layer was determined by converting the SMP penetration resistance signal into an index for the Young's modulus and multiplying it by a factor of 186, the factor that had been found in Section 4.2.2. Series 3B was the only series for which SMP profiles were acquired. Therefore, it was the only series that could be evaluated in respect of G_f , because a precise modelling was only possible if the Young's modulus of the different layers were known. The SMP signals of series 3B indicated that the slab should be subdivided in three layers with different material properties (see also the snow profiles in Appendix B).

Figure 4.22 shows the critical energy release rates G_f determined from FEM for the test day on 27 January 2006 (Series 3B) in relation to the beam length. Three different beam length were tested: 0.6 m, 1.2 m and 1.8 m (Figure 4.20a). Figure 4.22 confirms what would be expected for a fracture mechanical process: The critical energy release rate for fracture propagation is independent of the length of a test beam ($N = 21, P = 0.31$). The mean G_f of series 3B resulted in:

$$G_f = 0.066 \pm 0.014 \text{ J/m}^2. \quad (4.15)$$

The critical energy release rate of the weak layer tested in the field was about 65% higher than the mean critical energy release rate of the weak layers tested in the laboratory ($G_c = 0.04 \pm 0.02 \text{ J/m}^2$). However, the tested weak layers as well as the tested slabs in the field were not the same as the ones that were tested in the laboratory.

Figure 4.22 shows the dependance of the energy release rate G on the cut length a . The statistically significant correlation ($N = 21, R^2 = 0.76, P < 0.0001$) is a result of

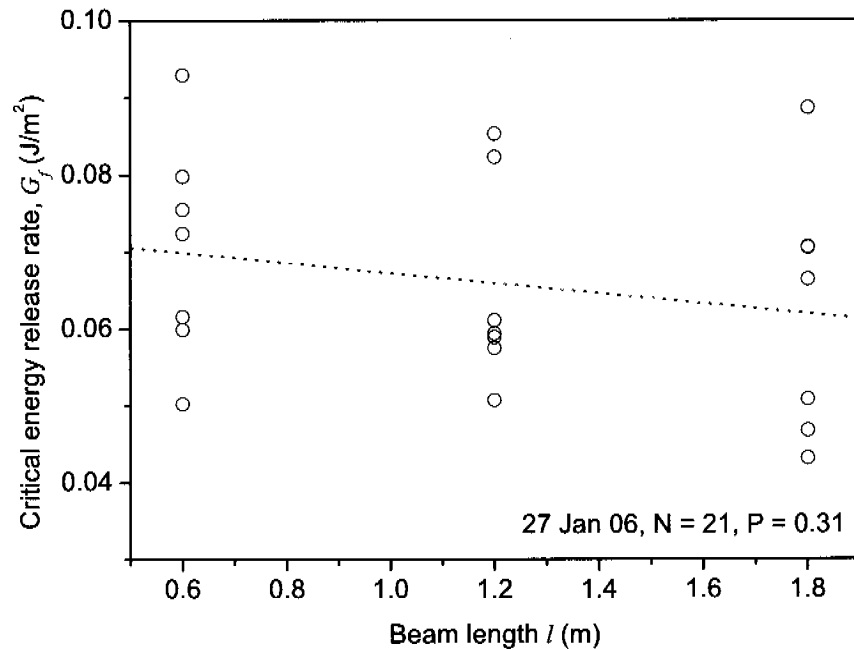


Figure 4.21: Critical energy release rate G_f determined with FEM in relation to the beam length for the field tests of 27 January 2006. A linear regression (dotted line) was statistically not significant, i.e. G_f does not depend on the beam length.

the fact that for the different test beams the geometry and the elastic properties were approximately the same. Thus, if the cut length is increased, the energy release rate increases too. However, the scattering of the data points represents the fact that the elastic properties of the various test were not exactly the same.

Figure 4.23 shows a box plot which shows the distribution of the critical crack length a_c for the three testing days. In statistics, the box plot is a convenient way to display a summary of five numbers which describe the distribution of a parameter. It consists of the smallest observation, lower quartile, median, upper quartile and largest observation. The height of the box, defined by the upper and lower quartile is known as the interquartile range (IQR) and includes 50% of all values. The position of the median in the box gives information of the skewness of the distribution. The cross indicates the mean value and the circles indicate the largest and smallest observation. The so called whiskers indicate the 5% and 95% level. Figure 4.23 shows that between the three measurement days the critical cut length tended to increase, although, the mass of the slab did not increase because there was no snow fall event during this period.

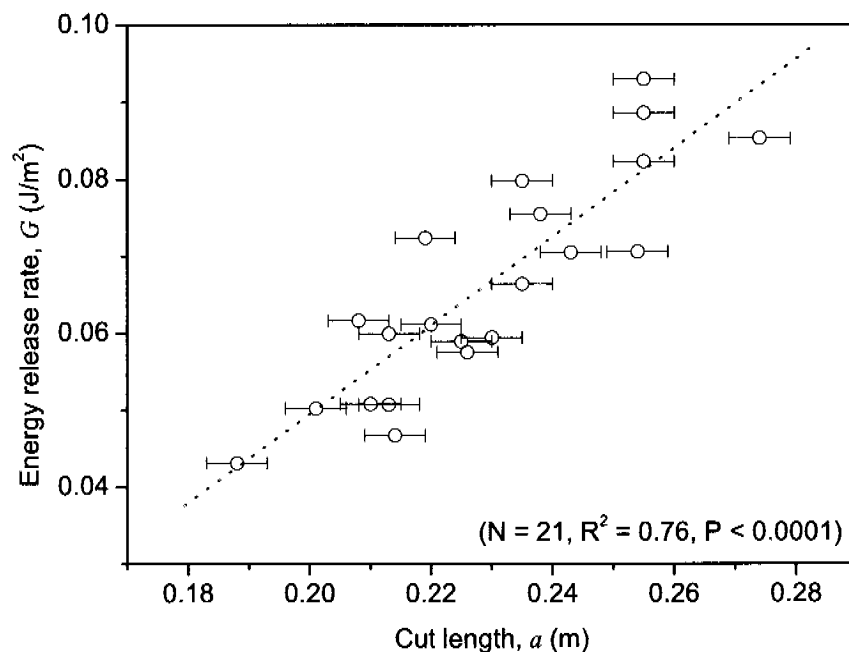


Figure 4.22: Energy release rate G in dependance of the cut length a . All tests were made with the same weak layer on 27 January 2006. A linear regression (dotted line) was statistically significant.

4.3.3 Influence of bending

In this section additional results based on the FE model of the field experiment will be presented.

Although the thickness of the cut that was made in the weak layer was only 2 mm, corresponding to the 2 mm thick snow saw, the cut surfaces were far from getting in contact to each other for our cut length $a_c < 30$ cm. Simulations showed that a cut length of more than 50 cm would have been required to bring the slab in contact with the basal layer for the elastic properties of the tested slabs. For our cut length, the vertical displacement of the slab due to bending did never exceed 50% of the gap size of 2 mm and was in most cases much less than 50% (Figure 4.24).

First simulations were made with a model which included a slab consisting of only one layer. However, the penetration resistance signals of the slab suggested that the slab should rather be modelled as to consist of three different layers. In the following the model was extended to a slab consisting of three layers (see Figure 3.8). Figure 4.25 shows the resulting tensile stresses in slope parallel direction σ_y for a model with a one

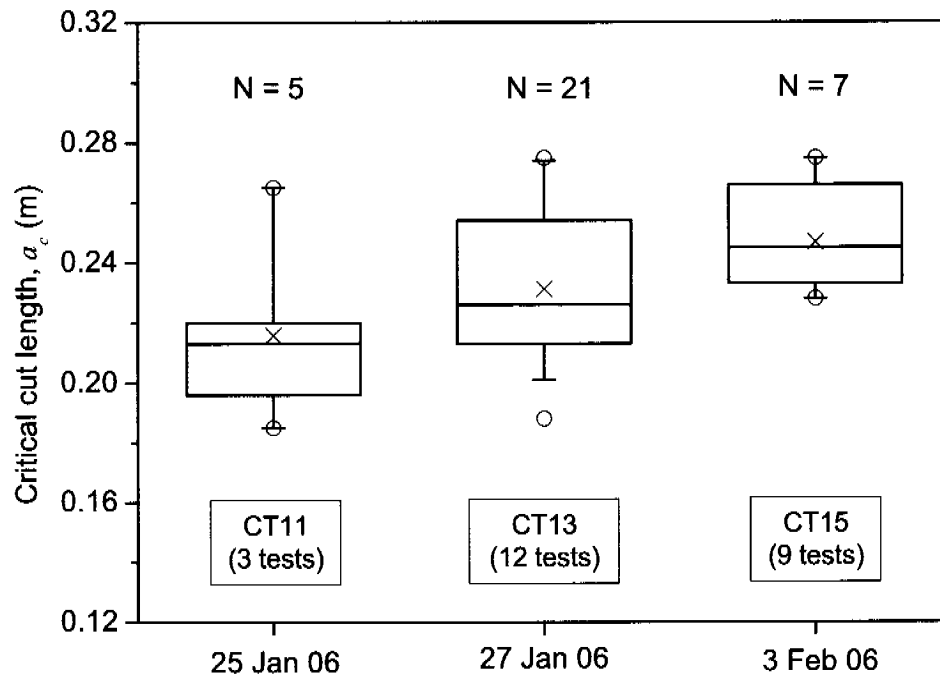


Figure 4.23: The distribution of the critical cut length a_c in a box plot for the three test days. Mean compression test (CT) results and number of compression tests are indicated at the bottom.

layer slab and for a model with a slab consisting of three layers with different material properties. Both beams had a length of 1.2 m and a width of 0.3 m. The basal layer had a slope normal thickness of $h = 13.6$ cm, a density of 246 kg/m^3 and a Young's modulus of $E = 12.2$ MPa. The slab properties are indicated in the caption of Figure 4.25.

Whereas for the one layer slab no stress concentrations can be seen, a different stress pattern is visible for the three layer slab (Figure 4.25). The stress concentration was not located where it would have been expected for a bending case, right above the crack tip, but a certain distance ahead of the crack tip. Obviously this stress concentration was a result of the combination of different layers with different material properties. However, results showed that the existence of stress concentrations depended very much on the properties and thicknesses of the three slab layers.

Finally, the influence of an existing gap on the energy release rate was tested. Therefore, a beam with rectangular shape was modelled, in contrast to the beam shape in Figure 4.25 in which the left and right face are always vertical, independent of the slope angle. The rectangular shape was chosen to be able to model also high slope angles up to

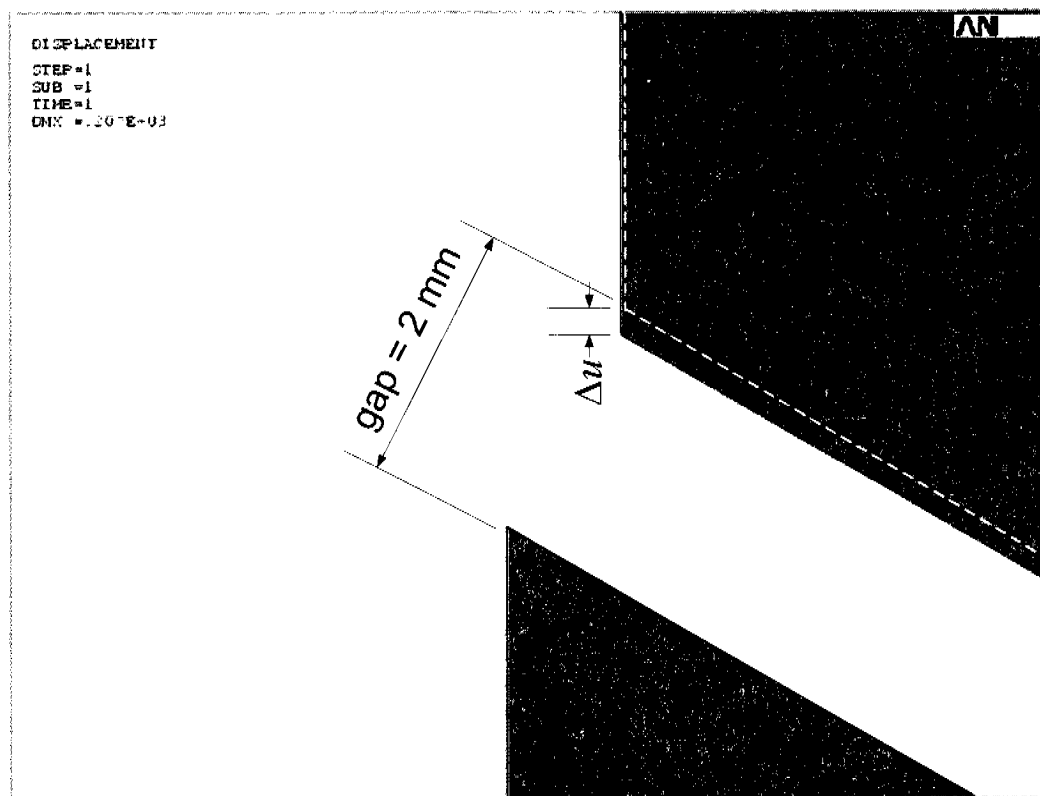


Figure 4.24: Detail of the upslope end of a test beam simulation (ANSYS output). The upper part (slab) bends due to gravity. The vertical displacement is indicated as Δu . The horizontal displacement between slab and basal layer has modelling reasons.

80°. The model had the following dimensions: beam length = 1.2 m, beam width = 0.3 m, slab thickness = 0.3 m, height of basal layer = 0.1 m, cut length = 0.2 m, slab density = 250 kg/m³, basal layer density = 300 kg/m³, Young's modulus of the slab $E_{slab} = 20$ MPa, Young's modulus of the basal layer $E_{base} = 30$ MPa. (This time the slab was again modelled as only one layer). The values for the Young's modulus correspond approximately to what can be found by Equation (4.9). With this model the energy release rate G was calculated for different slope angles φ for the case when a cut thickness or gap of 2 mm was included, and for the case when the cut thickness was set to zero. The cut surfaces were modelled as contact and target area, so that no penetration of the upper cut surface (the slab) was allowed into the lower cut surface (the basal layer). Therefore, in case the gap size was set to zero no bending of the slab was possible. No slope parallel friction between the cut surfaces was assumed. The results are presented in Figure 4.26a. For a slope angle of 30°, the energy release rate due to the combined bending and shearing was about 6 times the energy release rate due to pure shearing.

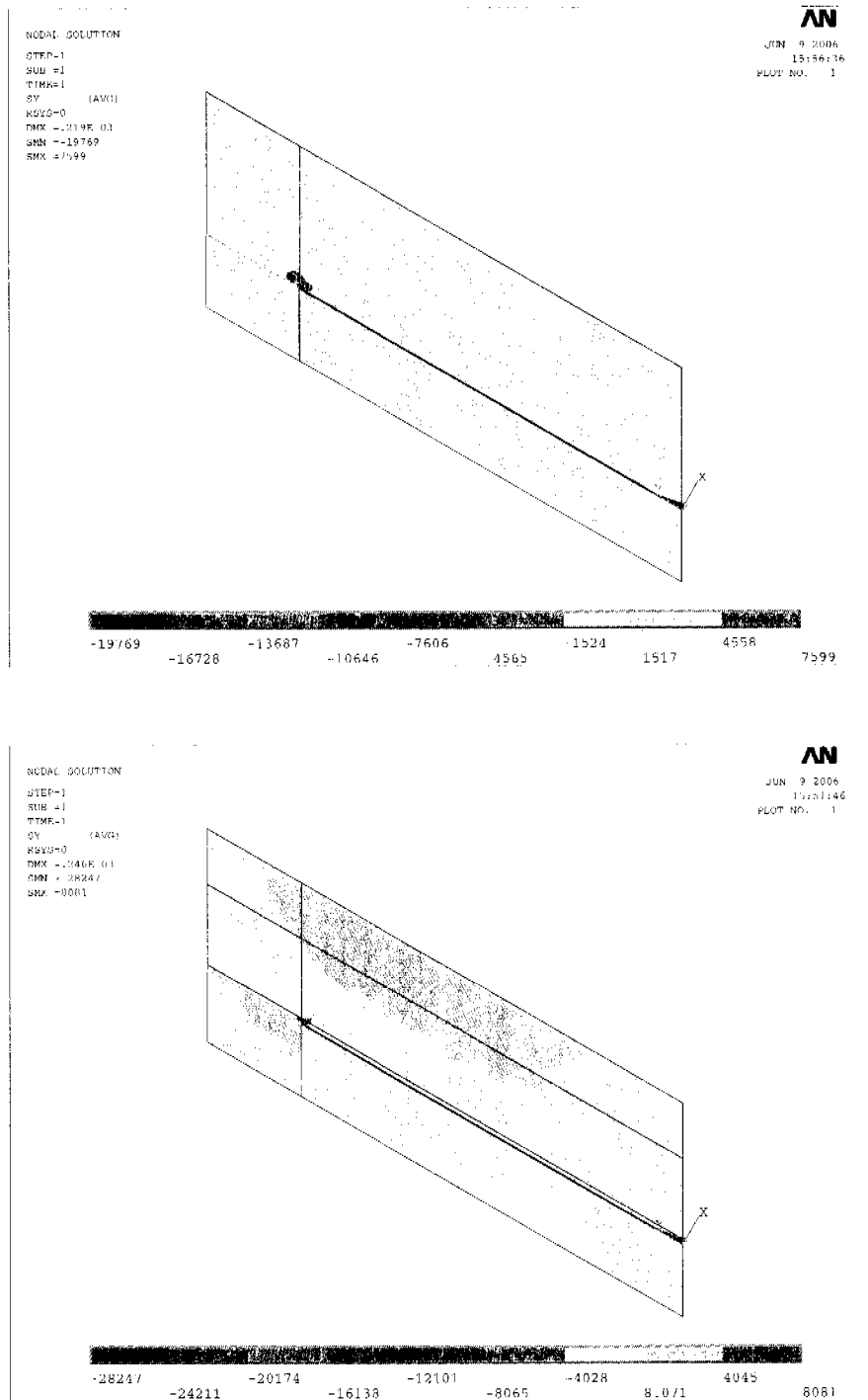


Figure 4.25: Top: Tensile stresses in slope parallel direction σ_y for the modelled geometry with slab consisting of $n=1$ layer. (Slab properties: $h = 26.6$ cm, $\rho = 167$ kg/m³, $E = 6.24$ MPa). Bottom: σ_y for a slab with $n=3$ layers. (Slab properties: $h_1 = 10.5$ cm, $\rho_1 = 120$ kg/m³, $E_1 = 3.72$ MPa; $h_2 = 15.2$ cm, $\rho_2 = 190$ kg/m³, $E_2 = 6.01$ MPa; $h_3 = 0.9$ cm, $\rho_3 = 273$ kg/m³, $E_3 = 10.5$ MPa).

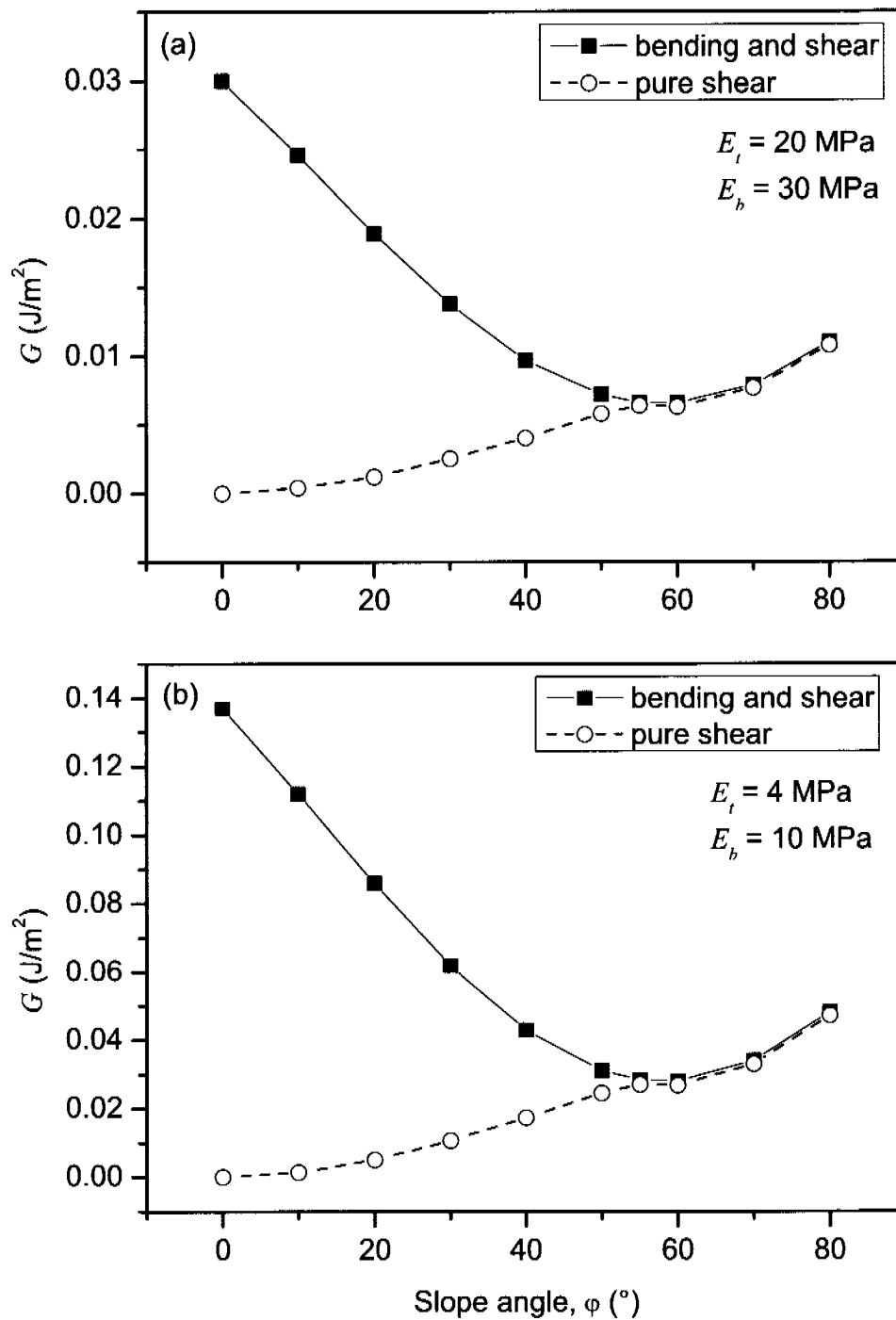


Figure 4.26: Finite element calculation of the energy release rate in dependence of slope angle for a model including a gap of 2 mm (squares), so that bending is possible, and for a model with a gap of zero extension (circles). The material properties for the calculation (a) were: $\rho_{slab} = 250$ kg/m³, $\rho_{base} = 300$ kg/m³, $E_{slab} = 20$ MPa, $E_{base} = 30$ MPa; and for (b): $\rho_{slab} = 250$ kg/m³, $\rho_{base} = 300$ kg/m³, $E_{slab} = 4$ MPa, $E_{base} = 10$ MPa.

In a second simulation the Young's modulus of slab and basal layer were reduced to 4 MPa and 10 MPa, respectively. These values correspond to what could be assumed from the results summarized by Mellor (1975) (Figure 4.14). The result is shown in Figure 4.26b. The energy release rates G were higher for the lower Young's modulus. This would be expected from the theory. However, the shape of the curves stayed the same. Again, the combined bending and shearing was about 6 times the energy release rate due to pure shearing for a slope angle of 30° .

4.3.4 Analytical approach for the field experiments

An analytical approximation for the calculation of the critical energy release rate for our field experiments was searched, in order to test if adequate results for G_f could be obtained without the precise but time consuming finite element simulation.

The findings in Section 4.3.3, that the slab was bending over the length of the cut a_c without a contact to the layer underneath the 2 mm thick cut, suggested to concentrate on a bending model rather than on a shear force model.

An analytical model for collapse in horizontal stratifications from Heierli and Zaiser (2006) can be used for the determination of the fracture energy of a weak layer in relation to the crack half length r_c due to a slope normal collapse (Equation 2.45). The model must be adapted for the asymmetric situation in our experiments and for the slope angle. Instead of an internal collapse of the weak layer on the length $2r_c$ (resulting in bending of the slab), a collapse at one edge of the beam with length $r_c = a_c$ was assumed.

The solution space for the displacement in slope normal direction (Heierli and Zaiser, 2006) is given by

$$U(X) = -X^4 + c_3X^3 + c_2X^2 + c_1X + c_0, \quad (4.16)$$

where U and X are dimensionless and defined by: $U = u/h_{WL}$ where h_{WL} is the collapse height, and $X = x/r_0$ where $r_0^4 = 24h_{WL}\mathfrak{D}/\rho Hg$, with \mathfrak{D} the rigidity of the slab (Equation 2.46) and H the slab thickness. The four coefficients c_i had to be reevaluated with new boundary conditions. The new boundary conditions for a beam fixed at $X = R$ and free bending a $X = 0$ are: $U(R) = 0$, $U'(R) = 0$, $U''(0) = 0$ and $U'''(0) = 0$. Equation (4.16) becomes

$$U(X, R) = -X^4 + 4R^3X - 3R^4. \quad (4.17)$$

The total energy of Equation (2.44) in dimension-less form can be written as (Heierli and Zaiser, 2006)

$$\Phi(U) = \int \left\{ \frac{1}{48} \left(\frac{d^2U(X)}{dX^2} \right)^2 + U(X) + W_f \theta(-U(X)) \right\} dX, \quad (4.18)$$

with $R = r/r_0$, $\Phi = V/V_0$ where $V_0 = \rho Hghr_0$ and $W_f = w_f/\rho Hgh$.

By substitution of Equation (4.17) into Equation (4.18), the result for the energy in dependence of the dimension-less crack extension R is obtained:

$$\Phi(R) = -\frac{3}{5}R^5 + W_f R. \quad (4.19)$$

The energy gets critical when it reaches a maximum, as it was explained in Section 2.6.3. Thus Equation (4.19) yields

$$\frac{d\Phi_1(R)}{dR} = 0 = -3R^4 + W_f. \quad (4.20)$$

By rearranging Equation (4.20) and re-transformation of the dimensionless variables, a relation between the fracture energy of the weak layer w_f which corresponds to the critical energy release rate G_f (Equation 2.8) and the critical cut length a_c can be found:

$$G_f \hat{=} w_f = \frac{3}{2} \frac{(\rho g)^2}{EH} a_c^4. \quad (4.21)$$

Equation (4.21) is still for a horizontal situation (slope angle $\varphi = 0$). Since our experiments took place on a slope with a given angle we have to correct for that by $g \cos(\varphi)$. Furthermore, the cut length a_c has to be corrected, because our beam geometry is not rectangular but a parallelogram with angle φ (see Figure 3.8). The corrected cut length $\tilde{a}_c = a_c + H/2 \tan(\varphi)$ compensates for the additional weight due to the geometry difference. Thus, for our experimental situation, Equation (4.21) transforms to

$$G_f = \frac{3}{2} \frac{(\rho g \cos(\varphi))^2}{EH} \tilde{a}_c^4. \quad (4.22)$$

The resulting critical energy release rate G_f in relation to the cut depth a_c are presented in Figure 4.27. The data are compared to the numerical FEM results of Figure 4.22. On average, the analytical results are a factor four lower than the numerical results. If for comparison G_f is calculated according to the pure shear approach proposed by McClung (1979), Equation (2.42), the results differ from the numerical results by a factor of 60 up to a factor of 150 (Figure 4.27).

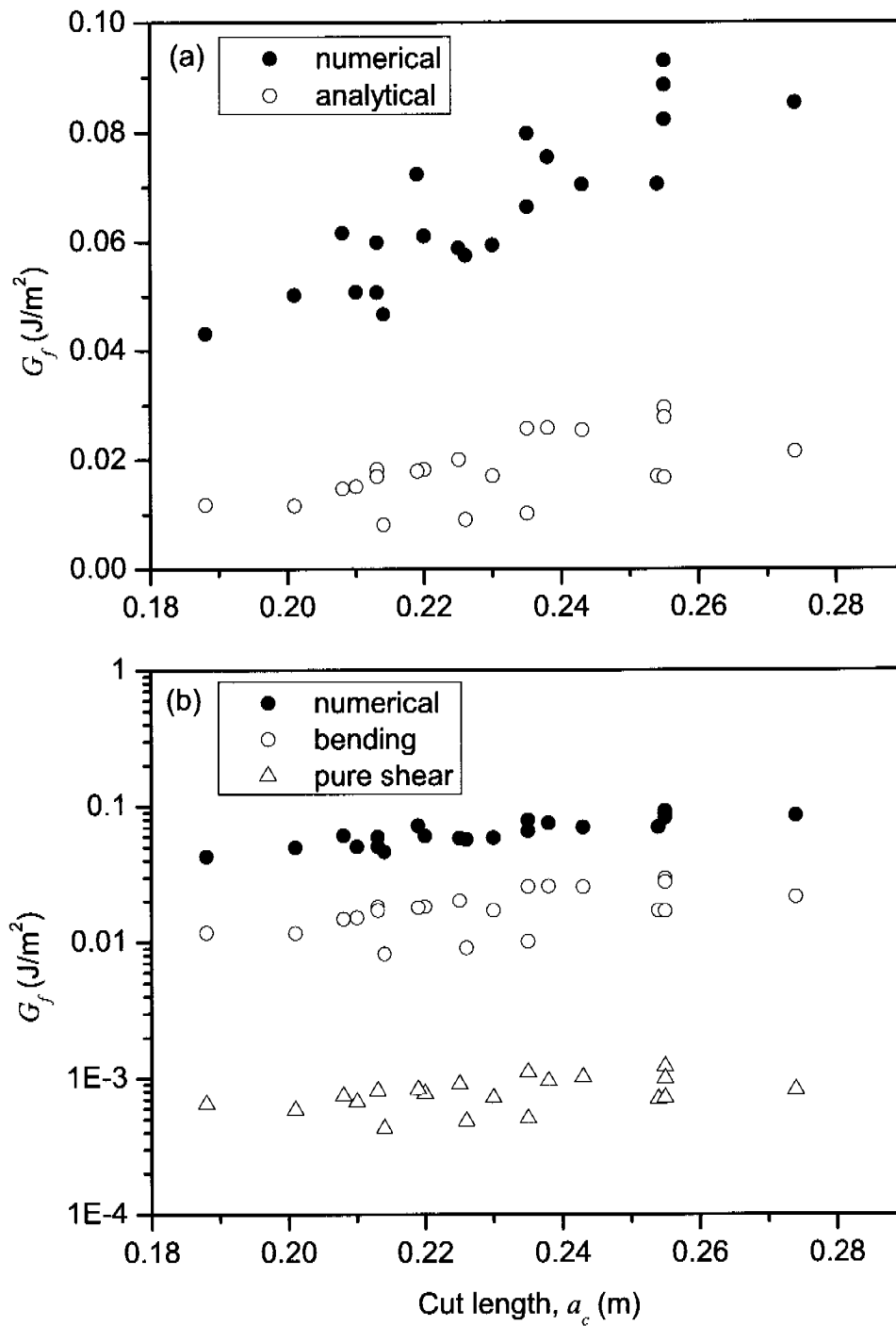


Figure 4.27: The critical energy release rate G_f in relation to the cut length a_c . (a) The analytical bending beam results are compared to the numerical FEM results. (b) Comparison with the pure shear results of Equation (2.42) in logarithmic scale.

Seite Leer /
Blank leaf

Discussion

5.1 Fracture in mode I

5.1.1 The load-displacement curve

In mechanics and engineering load-displacement or stress-strain diagrams play a crucial role for the characterization of material behaviour. Since a load-displacement curve was recorded for each three-point bending (3PB) test, a representative example of a load displacement curve (Figure 4.1) will be discussed here.

The strain rates $\dot{\epsilon}$ for the 3PB-tests were between $4.2 \times 10^{-1} \text{ s}^{-1}$ for the smallest specimen with a height of 8 cm and $1.3 \times 10^{-2} \text{ s}^{-1}$ for the largest specimen with a height of 32 cm. Thus the strain rates were clearly in the brittle range according to the brittle to ductile transition which is between $\dot{\epsilon} \simeq 1 \times 10^{-3} \text{ s}^{-1}$ and $\dot{\epsilon} \simeq 1 \times 10^{-5} \text{ s}^{-1}$ depending on grain type and temperature (Narita, 1980). Brittle behaviour is manifested in a linear increase of the load due to a displacement until failure. However, Figure 4.1 shows that this holds only to a limited extent for our fracture experiments. The slope decreases slightly towards the failure point. After the peak load is reached, the force signal does not instantly drop down to 0 N but remains at a level of about 28 N for a duration of 25 ms. These two observations indicate that strain softening processes took place during the experiment. Strain softening processes imply that snow behaves quasi-brittle (see Section 2.4.1).

The small drops in the force signal that became more pronounced and more frequently towards the point of global specimen failure resemble the so called pop-ins, known from other materials. Pop-ins are the result of very small brittle crack extensions (e.g. Sumpter, 1991). However, we suggest that these drops in the force signal are rather the result of local crushing of the ice matrix close to the point of loading. Comparable to the crushing of honeycombs described by Gibson and Ashby (1997). The load applied by the sensor head leads to a local compaction of the ice-matrix. This compaction is not

continuous but step wise provoking the drops. The compaction increases the contact area and decreases the pressure until the load can be applied to the surrounding ice-matrix without further local compaction. This assumption is supported by the observation of local deformation of the snow specimen close to the sensor head. The deformations increased with decreasing density but did not exceed a few millimeters.

In conclusion, it was found that even for fast loading rates snow undergoes strain softening. This indicates that the mechanical behaviour of snow involves non-linear effects that can not be neglected. The behaviour can not be assumed as to be purely linear elastic.

5.1.2 The bending experiment to determine tensile strength

The tensile strength of snow was measured in 3PB-tests with unnotched specimens of different snow densities.

Our results for the tensile strength are in good agreement with the results found by Mellor (1975) and the compilation by Jamieson and Johnston (1990) and others. Our data as well as the fit function fall into the ranges indicated in Figure 4.2. However, our data are constantly at the upper boundary of the range denoted by Jamieson and Johnston (1990) and for higher densities even beyond. This becomes obvious when our fit function (dash-dot line) is compared to the fit function of Jamieson and Johnston (1990) (dashed line). The difference is most probably due to the different type of test used. While Jamieson and Johnston (1990) performed a direct tension experiment, we performed a bending experiment. According to Schindler (private communication), it can be observed that the results for the tensile strength determined in bending experiment are generally higher than the ones determined in direct tension experiments. Furthermore, Jamieson and Johnston (1990) report in their study, that their experiments appeared lower for snow densities above 250 kg/m^3 than other in-situ studies. We confirm this observation with our data. A further explanation might be, that our experiments were performed in the cold laboratory at a constant snow temperature of -10°C , while the experiments of Jamieson and Johnston (1990) were performed in the field with no control on the temperature. Typical slab temperatures might be around -5°C . Since strength tends to decrease with increasing temperature (Narita, 1983) one part of the observed difference can be attributed to this effect. And finally, part of the difference could also origin in a size effect. Our specimen sizes were larger than the ones used by Jamieson and Johnston (1990) or (Narita, 1983).

In conclusion, the 3PB-test was well suited for the determination of the tensile strength, it was easy to perform and the obtained results were comparable to previously published data. The main advantage was that strength and fracture mechanical experiments could be performed simultaneously, with specimens of the same size and the same snow type. This guaranteed the best possible comparability between fracture and strength data.

5.1.3 Comparison of 3PB-tests and CB-tests

Mode I fracture experiments were made with homogeneous snow samples in three-point bending (3PB-tests). Additionally, cantilever beam tests (CB-tests) were made in order to directly compare our results with previously published results obtained with similar cantilever tests.

First, the results of the 3PB-tests will be discussed, especially the relation of the critical stress intensity factor (SIF), K_{Ic} , to snow density. Then, the 3PB-tests are compared to the CB-tests, and finally, the CB-tests and 3PB-tests are compared to similar tests performed in recent years.

For the first time, the 3PB-test was adapted to snow to determine the critical stress intensity factor K_{Ic} . (In the 1960ies Stearns (1964) used a hand-operated press to apply a three-point load on natural snow-ice samples and measured the flexural strength and elastic properties of the samples). The results of K_{Ic} determined in 3PB-tests are presented in relation to snow density in Figure 4.3. For this diagram only the data acquired with the standard specimen size 50 cm × 20 cm × 10 cm were considered. The data show a large scatter, which is however comparable to other experimental results in snow. Surprising is, that K_{Ic} for series D is about twice the K_{Ic} for series F, although both series have about the same mean density of 320 kg/m³ (see Table 4.1 for more details). The variation can not be attributed to a different snow temperature since the difference in temperature was small for the two series. It is assumed that the variation originates in the different snow type of the two series. While the samples for series D were collected in Davos and consisted of old snow with small rounded grains and partly mixed forms, the samples of series F were collected about 1000 meter higher at Weissfluhjoch. The snow was not older than four days and was cut out of a wind slab consisting of small rounded and partly decomposed and fragmented snow particles. The hand hardness index was higher for series D (1F-K) than for series F (1F) and a higher penetration resistance could be identified in the SMP signals (~ 1 N compared to ~ 0.5 N). This shows that although the series had the same density they differed in other mechanical properties such as the hardness, the penetration resistance or the Young's modulus.

It is not known, if a power-law best describes the density dependance of K_{Ic} . In fact, Perla et al. (1982) who used a power-law to describe a strength to density relation, stated that there is probably little justification for favouring any particular strength to density correlation, and this might be the same for other mechanical properties such as K_{Ic} . Our data could also be fitted by a bi-linear model or a more general model consisting of different functions for different density ranges. In fact, such transitions are known for other materials but also for snow. According to Golubev and Frolov (1998), there exist several transitions in snow. Two of them can physically be explained and are well known. The critical densities 550 kg/m³ and 820 kg/m³ are the borderlines between snow, firn and porous ice. Golubev and Frolov (1998) observed three more borderlines at about 150, 330 and 700 kg/m³. However, they stated that the structural stages of snow corresponding to these values remain unclear. In Figure 4.3 a transition could possibly be

located at a density of about 280 kg/m^3 . However, much more data would be required to assess such a density dependence. The choice of a particular correlation function would remain somehow arbitrary. Generally power-law fits are chosen to describe mechanical properties in relation to density, because the data linearize well in log-log plots.

In Figure 4.4 the CB-tests are compared to the 3PB-tests. According to LEFM, K_{If} should be a material constant and independent of the test method, i.e. equivalent to the fracture toughness K_{Ic} . However, the K_{If} values for the CB-tests in Figure 4.4a and Figure 4.4b were considerably smaller than those for the 3PB-tests. Among the CB-tests, the ones with a cantilever length of $L = 10 \text{ cm}$ failed at smaller K_{If} than the ones with $L = 15 \text{ cm}$. Hence, a dependence of K_{If} on the test method can be observed. The essential difference between the test methods is their different specimen shape, since the effect due to mixed-mode fracture in the CB-tests was taken into account (Equation 3.12). Therefore, the geometry of the specimens seems to be responsible for the difference.

The dependence of K_{If} on the cantilever length has previously been described by Failletaz et al. (2002). They proposed that the elastic energy might be stored along a fractal force pattern instead of being stored homogeneously in the material. Our explanation is that due to the different cantilever length, the specimens have different shapes. This shape dependence of K_{If} is a result of the fact that LEFM can not fully be applied for the present specimen dimensions, because the size criterion Equation (2.19) is not fulfilled. This is also supported by the fact that we estimated the size of the fracture process zone R_c in the order of 5 cm . Thus for cantilever beam specimen in which $a/h > 0.7$, the ligament size gets smaller than the fracture process zone. Therefore, the fracture process will be mostly governed by plasticity.

In Figure 4.4b linear regressions are applied to the 3PB data and the CB data. The linear regressions for the CB-tests are statistically significant, while the one for the 3PB-tests is not. This is due to the fact that for the CB-tests the loading of the crack tip is due to the weight of the protruding beam. No additional load is applied. Therefore, the load is approximately the same for different tests with a given L and thus for a longer cut depth a a higher critical stress intensity factor K_{If} will result. For the 3PB-tests the load is constantly increased up to failure for a given cut depth. For differing cut depths, different loadings will be required to bring the specimen to failure and thus the resulting K_{If} is approximately constant.

The power-law fits suggested by Schweizer et al. (2004) show that their K_{If} values were on average lower than the ones we obtained. Schweizer et al. (2004) reported values for A between $3.1 \times 10^{-5} \text{ kN m}^{3/2}/\text{kg}$ and $1.3 \times 10^{-5} \text{ kN m}^{3/2}/\text{kg}$ and for B between 1.9 and 2.1 depending on snow type. The difference is relatively small up to a density of about 250 kg/m^3 and further increases with increasing density. The main reason for the difference can be attributed to the equations used for the determination of K_{If} . Especially for deep cracks, which are expected for higher densities, Equation (3.4) can differ considerably from the one used by Schweizer et al. (2004). Figure 5.1 shows variations of up to 40% for our data. Since most of our cantilever experiments involved

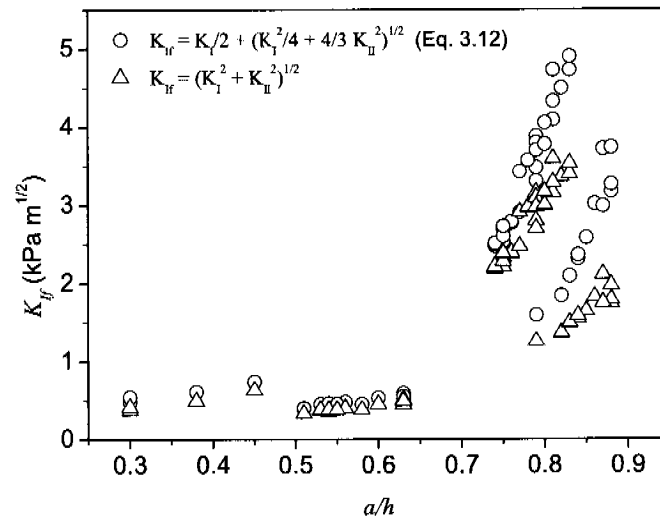


Figure 5.1: The critical energy release rate, K_{I_f} , in relation to the relative cut length. The CB-test data evaluated with Equation (3.12) (circles) compared to an evaluation of the same data with the Equation used by Schweizer et al. (2004) (triangles).

deep cracks it is assumed that K_{I_f} might have been underestimated by Schweizer et al. (2004).

In conclusion a clear shape dependence of K_{I_f} was found for the different experimental methods. This was attributed to a violation of the size criterion of LEFM (Equation 2.19). Our K_{I_f} results were in general higher than previously found values. This was attributed to a more appropriate evaluation method compared to previous studies. For future studies it should be considered to relate K_{I_f} to other mechanical properties than the density. A relation to the Young's modulus or the penetration resistance might decrease scatter considerably.

5.1.4 Fracture speed

3PB-tests were recorded with a high-speed camera. From the recordings the fracture speed was calculated.

The measurement of the fracture speed was not a primary objective of the high-speed recording. Primarily, the high speed photography was used to get an impression of the fracture processes. The measurement of the fracture speed was not very accurate, because the crack tip had to be identified on subsequent photos, in order to measure the crack advance. The identification of the crack tip could be done with a precision not

better than $\Delta l = \pm 5$ mm, because of the low contrast in snow. Maybe the contrast could be increased by illuminating the specimen with ultra-violet light. However, an ultra-violet light source was not at our disposal.

The fracture velocity in mode I increased until a maximum fracture speed of $v_{I,max}$ and then decreased again with further crack advance (Figure 4.11). This decrease is due to the compression forces in the upper part of a bending beam. Figure 4.11 shows that the maximum fracture speed depends on the specimen size. In the larger specimen ($h = 30$ cm) the fracture speed was about 40% higher than in the smaller specimen ($h = 20$ cm), this suggests that the maximum fracture speed that could be reached in snow of the tested density was not reached for our specimen sizes.

Observations show that the maximum crack speed in brittle materials reaches hardly more than half of the Rayleigh wave speed v_R (Rafiee et al., 2004). v_R is less than 10% smaller than the shear wave velocity v_S (Studer and Koller, 1997), thus

$$v_{max} \leq 0.5 v_S = 0.5 \sqrt{\frac{S}{\rho}} = 0.5 \sqrt{\frac{1}{\rho} \cdot \frac{E}{2(1+\nu)}}, \quad (5.1)$$

where S is the shear modulus, E the Young's modulus, ν the Poisson's ratio and ρ the snow density.

All recorded 3PB-tests were of series I with a mean snow density of 256 kg/m^3 and if we assume a Young's modulus between 2.5 MPa and 20 MPa, corresponding to what can be found in literature for this density (e.g. Mellor, 1975; Scapozza, 2004), and a Poisson's ratio of 0.2 a range of fracture speeds of

$$24 \text{ m/s} \leq (0.5 v_S) \leq 67 \text{ m/s} \quad (5.2)$$

is achieved. If however, the Young's modulus for every test is calculated according to the relation we found in Equation (4.9), the results for half of the shear wave velocity are somewhat higher ($96 \text{ m/s} \leq 0.5 v_S \leq 105 \text{ m/s}$). Therefore, the measured fracture speeds of ~ 20 m/s achieved in our largest specimen is most likely in a region where the fracture speed accelerated.

Recently, Johnson et al. (2004) and van Herwijnen and Jamieson (2005) measured independently propagation speeds of a fracture in a weak snowpack layer of about 20 m/s. However, their experiments were under shear loading and not under tensile loading like in our tests. Furthermore it is in both cases not clear if the maximum velocity was reached or if the fracture speed was still accelerating.

Heierli (2005) proposed an analytical model for fracture propagation in a partly collapsible snow stratification. For the fracture speed he proposed a velocity of $v = \sqrt{v_0 v_S}$ with $v_0^2 = gH^2/(12h_{WL}(1-\nu))$, where H is the slab height and h_{WL} the collapse height of the weak layer. By using the experimental data of Johnson et al. (2004), Heierli (2005) was able to reproduce the measured velocity of 20 m/s. Comparing the propagation of a shear fracture along a weak layer to the shear fracture propagation of earthquakes,

McClung (2005a) suggested that the shear fracture speed would be in the order of $v = (0.7 \dots 0.9) v_g$. However, if the processes in an earthquake can be compared to the processes in the snow cover remains unclear.

In conclusion we found fracture speeds of about 20 m/s for tensile fractures in snow. Indications were found that the measured fracture speeds were still accelerating and that a terminal velocity could not be measured because of the limited specimen size. The terminal velocity is assumed to be a factor 1.5 to 5 higher than the measured fracture speeds.

5.2 The limitation of LEFM for snow

5.2.1 The size correction function

3PB experiments with for different specimen sizes were performed to determine the size dependence of K_{If} and to find a suitable size correction function. Four experimental series were performed (Series E, F, H and I).

In Figures 4.5 and 4.6 the coefficients c_1 and c_2 of the four series E, F, H and I were determined. With these coefficients it was possible to evaluate the characteristic size D_0 being the point where the line for linear elastic behaviour intersects with the horizontal line for plastic collapse in Figure 2.4. The mean value of the characteristic size for the three statistically significant series was $\bar{D}_0 = 0.29 \pm 0.08$ m. Thus, \bar{D}_0 is of similar size as our specimen sizes. This suggests that our specimens were not large enough to be in a range where LEFM would be applicable (see Figure 2.4). The slope of a linear regression of -0.21 ± 0.05 in Figure 4.4 was significantly lower than the required slope of $-1/2$ corresponding to the specimen size range in which LEFM would be applicable (Figure 2.4). The reason for this is the large size of the fracture process zone as it will be discussed in the next section. Snow specimens would need to have a size of several meters to be in the linear elastic range. However, it is not possible to increase the sample size substantially, because larger samples cannot be handled any more.

Bazant and Planas (1998, p. 111) suggested that for concrete D_0 would be a multiple of the maximum aggregate size of about 2 to 20, depending on the test conditions. Based on this assumption and on volume fraction considerations, McClung (2005b) estimated D_0 to be about 10 cm for snow. Bazant and Planas (1998) wrote that the ratio $b = D/D_0$ should be at least 25 if the deviation from LEFM should be less than 2%. At best we obtain a ratio of $b \simeq 1$, because D_0 is similar to our specimen dimensions. This confirms that the specimen dimensions required for LEFM are not feasible for any experiments.

Even in the case of a snow slab avalanche this criterion is not fulfilled. Mean fracture depths measured slope perpendicular at the crown (tensile fracture) of slab avalanches were about 65 cm for a data set including natural and human triggers (Perla, 1977) and about 40 cm for only human-triggered avalanches (Schweizer and Lütschg, 2001).

With D_0 the so called equivalent fracture toughness, K_{Ic}^e (Equation 4.5), was determined. K_{Ic}^e is an experimental estimate of the real fracture toughness K_{Ic} . As can be seen in Equation (4.5), the equivalent fracture toughness, K_{Ic}^e , is always larger than the measured critical stress intensity factors, K_{Iff} . Once the equivalent fracture toughness is determined it is also possible to determine the critical SIF for any other problem size D by rearranging Equation (4.5). For example, Equation (4.5) can be used for a first estimate of a critical stress intensity value representative for a slab avalanche with a slab thickness D of 50 cm. However, to get a realistic value it would be necessary to add a shape correction factor accounting for the different shapes between laboratory experiments and slab geometry. For instance, the ratio (a/h) was kept at 1/10 for the various sizes of our 3PB specimen. There is no reason, why in a tensile fracture of a slab on a real slope the ratio between a crack and the slab thickness should also be 1:10.

With our experiments, we confirmed that fracture toughness for snow is very low compared to other materials, as it was previously stated by others (Kirchner et al., 2000; Schweizer et al., 2004). For the density range we observed (Figure 4.8) the equivalent fracture toughness did not exceed $10 \text{ kPa}\sqrt{\text{m}}$. To point out the order of magnitude a few examples for other materials are given (Gross and Seelig, 2001, p.85): concrete ($K_{Ic} = 150 \dots 950 \text{ MPa}\sqrt{\text{m}}$), glass ($K_{Ic} = 630 \dots 1250 \text{ MPa}\sqrt{\text{m}}$), or steel ($K_{Ic} = 30'000 \dots 120'000 \text{ MPa}\sqrt{\text{m}}$).

In conclusion, we determined the order of magnitude of the characteristic size D_0 for snow. The size of D_0 of several centimeters indicated that we are not in the LFM range with our specimen dimensions. With D_0 an equivalent fracture toughness, K_{Ic}^e , could be determined and a size correction function could be proposed. A size correction will be required for the results of any mechanical experiments in snow. We confirmed that snow has an extremely low value of K_{Ic} ($K_{Ic} \leq 10 \text{ kPa}\sqrt{\text{m}}$).

5.2.2 The fracture process zone

With the results for the tensile strength and the equivalent fracture toughness for snow, the fracture process zone in snow could be determined according to Equation (2.20)

The size of the fracture process zone R_c was estimated to be in the range of five centimeters (Figure 4.9) with a slight trend to decrease with increasing snow density. At a density of 100 kg/m^3 , R_c had a size of 8.9 cm and decreased to 4.1 cm for a density of 400 kg/m^3 . However, it was observed that this trend depended very much on the exponents of the fit functions for σ_c and K_{Ic}^e (Equations 4.1 and 4.6). Depending on how the data are fitted this trend can change, but, and this is important, the influence on the mean size of R_c stays low.

Nevertheless, it is assumed that R_c should decrease with increasing density, because according to Bazant and Planas (1998) the size of the fracture process zone is linked to the characteristic structural size of the material. Whereas in a metal, the characteristic structural size might be in the atomic scale, in snow, the characteristic structural size is

rather given by the size of the ice grains which build up the ice-matrix, comparable to the edges which interconnect vertices in a cellular solid (Gibson and Ashby, 1997, p.26). Typically this size will be in the order of 1/10 millimeter. If the snowpack settles, the grains get closer packed together which increases the density, resulting in a decrease of the characteristic size and thus in a decrease of the process zone.

The criterion for LEFM, introduced in Section 2.4.2, that the fracture process zone R_c should be smaller than $a/8$ or $(h - a)/8$ is clearly not fulfilled for our specimen sizes. We introduced a pre-crack of length $a = h/10$ in our specimens. The crack length a was between 1 cm and 3 cm depending on specimen size. Thus, R_c should be smaller than a few millimeters to fulfill the criterion. The determined R_c is larger by a factor of 10. Our experiments can therefore not be considered as to be in the linear elastic range. The fracture behaviour of a non-ductile material due to a relatively large fracture process zone is often called "quasi-brittle" (Bazant and Planas, 1998).

In conclusion, for the first time, the size of the fracture process zone was experimentally determined in snow. The fracture process zone is in the order of centimeters. This proves, that snow has to be considered as quasi-brittle material for feasible specimen sizes.

5.2.3 The FAD

A failure assessment diagram was established by plotting K_{If}/K_{Ic}^e over σ_{Na}/σ_c for our data. Therefore, the fit functions for σ_c and K_{Ic}^e (Equations 4.1 and 4.6) were used.

The failure assessment diagram (FAD) in Figure 4.10 shows that the method might work in principle but that the applicability to snow is questionable due to the large scatter of the data. In the diagram the critical stress intensity factor was divided by the equivalent fracture toughness and plotted against the effective stress σ_{Na} divided by the tensile strength σ_c . The results should lie on a curve between 1 on the y -axis and 1 on the x -axis indicated in Figure 2.5. Because we do not know how the shape of such a curve looks like for snow, the simplest possibility, a straight line between 1 on the y -axis and 1 on the x -axis was assumed in Figure 4.10 (dashed line). A fracture process governed only by the stress concentration at the crack tip would lie on the y -axis at 1 (pure brittle behaviour) whereas a failure process governed by overall strength would lie on the x -axis at point 1 (pure plastic collapse). Thus the closer the points in an FAD are to the y -axis, the more a fracture process is governed by the stress concentration at the crack tip and the better the fracture can be described by LEFM.

The four lines of data points originating from calculating the ratio of K_{If}/K_{Ic}^e represent the four different specimen sizes. Figure 4.10 illustrates that the larger the tested snow specimens were, the closer were the data points found to the y -axis. Or in other words, the larger a specimen is, the more important the processes acting at the crack tip become. Again, the size of the fracture process zone is a key parameter, because for a large specimen the process zone is negligible while for a small specimen it is not. This confirms what has been discussed in Section 5.2.1, the larger a specimen is, the closer

its behaviour gets to LEFM. This conclusion corresponds to the scaling law of Bazant and Planas (1998) (Figure 2.4).

The advantage of the FAD method compared to the scaling law of Bazant and Planas (1998) is that the FAD is independent of the test, whereas the scaling law is limited to short edge cracks.

Due to the large scatter the data do not concentrate on or around one point. If one considers the mean value of every specimen size, the mean values lie approximately on the dashed line.

In conclusion, one can say that due to the limited amount of experimental data and the large scatter, the shape of an FAD curve for snow could not yet be established. However, the results are in agreement with the principles of a FAD and the findings correspond to what had been found based on the scaling law of Bazant and Planas (1998).

5.3 Fracture in mode II

5.3.1 Determination of the Young's modulus

The Young's modulus of our samples was measured with a prototype of a cyclic loading device which was operated at a frequency of 100 Hz. The measured Young's modulus was compared to a calculated index for the Young's modulus derived from the SMP penetration resistance signal.

The dynamically measured Young's modulus for our samples was up to a factor of ten higher than previous quasistatic measurements summarized by Mellor (1975) (area A in Figure 4.14) and up to a factor of two higher than the results of Scapozza (2004) (area B). Mellor (1975) mentions that dynamically measured Young's modulus can be up to a factor of 2 higher than quasistatic ones. Our results are approximately a factor of two higher than the upper boundary of the Young's modulus reported by Scapozza (2004). The difference between our measurements and the ones compiled by Mellor (1975) (area A) can not entirely be explained by the different measurement techniques. However, the variations in the Young's modulus seem to be high even for comparable measurement techniques, since the results by Scapozza (2004) differ for low densities up to a factor of ten from the ones compiled by Mellor (1975), although both measurements were quasistatic.

As it was explained in Section 3.4.1, the frequency and the amplitude of a dynamic test can also have a distinct influence on the resulting Young's modulus (see Figure 3.9b and 3.10). Therefore, we used clear and reproducible criteria for the choice of these parameters: A frequency which ensures a measurement of the Young's modulus in the plateau region, a strain rate that ensures measurements in the brittle region and a deformation that does not cause any inelastic deformation of the snow sample.

The dynamic measurements compiled by Mellor (1975) (area C) are unfortunately only available for snow densities higher than 300 kg/m^3 . These values are even higher than our dynamic values, but again the measurement technique is different.

Since the slope of our data, in Figure 4.14, is flatter than a slope for the Scapozza (2004) data or the Mellor (1975) data, the deviations decrease between the results for increasing snow density.

The dynamically measured Young's modulus E_{dyn} showed good correlation with the index for the Young's modulus derived from the SMP penetration resistance signal E_{SMP} ($N = 24$, $R^2 = 0.81$, $P < 0.0001$) (Figure 4.15). The factor of 186 ± 7 is comparable to the factor of 150 found by Kronholm (2004). However, since Kronholm (2004) correlated his values to the ones found by Mellor (1975) and our measurements are a factor of ten higher than the Mellor (1975) results the question arises why our correlation factor is not a factor of ten higher than the one by Kronholm (2004). The origin of the difference remains unclear.

On the theoretical side, it is unclear why the theoretical approach by Johnson and Schneebeli (1999) to convert the penetration resistance into a Young's modulus needs a correction factor at all. Obviously, the conversion theory should further be investigated and calibrated.

It has to be pointed out that the cyclic loading device is only a prototype and that it was used for the first time on a regular basis for our experiments apart from a few tests in winter 2003/2004.

A further possibility to estimate the Young's modulus arose from the load-displacement curves recorded in our three-point bending tests. The slope of a tangent to the force-displacement curve can be used to estimate the Young's modulus of the tested specimen. For our example in Figure 4.16 this resulted in an Young's modulus between 5.5 and 6.5 MPa, depending on how the tangent was chosen. These values are well in the range of the results found by Scapozza (2004) and at the upper limit of the results summarized by Mellor (1975). However, the bending of the three-point bending beam was not considered, what would result in a decrease of the displacement and thus in an increase of the Young's modulus. Therefore, the estimated values might be lower limit values.

This method might be useful for an independent determination of the Young's modulus in relation to specimen density, but it would not be useful as an accompanying measurement to the shear fracture test, because after a shear fracture test the specimen is already destroyed and can not be used for a further three-point bending test. In this regard, the advantage of the cyclic loading device is that it needs only very small samples.

In conclusion, the cyclic loading device proved to provide reliable and reproducible results and seems therefore suited for further laboratory measurements of the Young's modulus. However, independent verification is recommended. The SMP measurement is by far the simplest, fastest and most suited for field testing. Therefore for the future, the goal has to be to further investigate and calibrate the conversion algorithm for the SMP penetration

resistance to a Young's modulus. More experiments with different snow types will be required as well as a sound measurement technique for the Young's modulus which can serve as basis for the calibration. We believe that the cyclic loading device has the potential to be used for calibrations.

5.3.2 Energy release rate in a mode II fracture

Mode II fracture experiments were made with layered snow samples. The energy release rate, G , was calculated by using a finite element model of the experimental geometry.

Based on the findings of Wei et al. (1996), it has been proposed by Schweizer and Camponovo (2001) that fracture propagation potential in snow would depend on the material mismatch between the snow layers, or in other words the difference in elastic properties. The fracture propagation potential is high, when a high critical energy release rate G_f can be achieved, i.e. when a high specific fracture energy w_f can be overcome by a crack extension. G_f was correlated to various elastic properties of the test specimen (Figure 4.17). However, only a slight trend for an increase in G_f with increasing elastic mismatch E_t/E_b could be observed which was statistically not significant. The findings on metal-ice interfaces showed that even for large changes in E_t/E_b only slight changes in G_f occurred (Wei et al., 1996). Since for our samples, the difference of the Young's modulus between the two adjacent layers was relatively small, typically not larger than a factor of two, and the scatter due to the inhomogeneity of the snow and/or due to the experimental method was large, a possible trend might be hidden. Wei et al. (1996) suggested decreasing G_f with increasing mismatch. The lack of dependence on the mismatch suggests G_f to be primarily a material property of the weak layer rather than to depend on the properties of the adjacent layers. In other words, the energy needed to destroy the bonds between the weak layer and the adjacent layers seems not to depend on the elastic mismatch between the two layers. This interpretation should be valid as long as the mismatch is not large ($E_t/E_b \lesssim 10$) which might be the case for most situations in a natural snow cover.

On the other hand, G_f did not depend on the Young's modulus of the weak layer either. However, the range of the Young's modulus for the weak layers tested in our experiments was relatively narrow, since the properties of the weak layers were similar for all series. For different types of weak layers, e.g. surface hoar, distinctly different material properties are expected. Therefore, we assume that different critical energy release rates would result and it should be possible to determine the critical energy release rate for various weak layer types, as long as the weak layer properties differ significantly so that potential relations of the energy release rate to material properties are not hidden by the inherently large scatter.

Compared to energy release rates, for example of ice-aluminium ($G_c = 1 \text{ J/m}^2$) or of ice-steel ($G_c = 5 \text{ J/m}^2$) (Wei et al., 1996), the mean energy release rate for our weak layers of $G_f \simeq 0.04 \text{ J/m}^2$ is extremely low. This coincides with other findings in snow,

for example the very low fracture toughness in mode I.

In conclusion, the obtained energy release rate for the tested weak layer were very low compared to other materials. No statistically significant dependance of G_f on the elastic mismatch of the adjacent layers could be observed.

5.3.3 Comparing numerical and analytical solutions

Two analytical approaches to determine G for our shear fracture experiment were compared to the FEM results: A cantilever beam with deep crack approach and a bilayer with interface crack approach. Therefore, specimens with different simulated material properties were modelled with finite elements and compared to the solutions of the two analytical approaches.

The results showed that for both approaches the resulting energy release rates correlated well with the modelled ones (Figure 4.18a and b).

The cantilever approach which considers a homogeneous material with a deep crack – in our experiments the ligament length b was for most cases smaller than the length of the protruding part $b/t_t < 1$ – showed a dependance on the elastic mismatch of the two layers. Obviously, this is a result of the fact that for the deep crack approach the Young's modulus of the protruding layer E_t was used as elastic property for the whole specimen (homogeneous specimen). Thus, the more the Young's modulus of the basal layer E_b differs from E_t the more the analytical solution differs from the FEM solution (Figure 4.18c). The factor of about 0.5 between the FEM results and the deep crack cantilever results seems to be plausible because the analytical calculation is for a cantilever experiment with free boundary conditions. However, in our experiment one side is fixed and contributes, if at all, only to a limited extent to the energy release.

The bilayer solution adapted from Hutchinson and Suo (1992) did correlate as well with the results of the FE simulations. Here, no dependance of the correlation on the elastic mismatch was observed (Figure 4.18d). This is what would be expected, since both, the Young's modulus for the slab E_t and for the basal layer E_b , are used in bilayer approach. As for the deep cantilever approach, a factor of 0.5 between the FEM results and the bilayer with interface crack approach was observed. The reason might be the same. A result of the fixation of one side of our experimental specimen.

In conclusion, the results of both analytical approaches showed a good correlation with the FEM results: Cantilever beam with deep crack approach ($R^2 = 0.93$, $N = 21$, $p < 0.0001$), bilayer with interface crack approach ($R^2 = 0.69$, $N = 21$, $p < 0.0001$). For both a correction factor of about 0.5 was found. However, due to the higher coefficient of determination (R^2), the cantilever beam with deep crack approach should be preferred. With the cantilever beam with deep crack approach an analytical solution was found to calculate an approximate energy release rate for our experiments without the need of finite element simulation.

5.3.4 Comparing mode I and mode II results

In Figure 4.19 the critical energy release rates for the interfacial fractures in mode II were compared to fractures in mode I. Thereby, G_f for a mode II fracture was about 2.2 times smaller than G_f for mode I fracture.

In a homogeneous material, the critical energy release rate in mode I is in general lower than in mode II. This is a further reason why shear fractures in a homogeneous material kink or resulting in a pure tensile fracture. The reason why this is different in snow is that results from homogeneous mode I experiments are compared to results of layered mode II experiments. The stability of a homogeneous snow block is much higher than the stability of a weak layer in snow, therefore it is not surprising, that the resulting critical energy release rates are lower in mode II than in mode I.

Additionally, the effective critical energy release rate G_c for the mode I tests, i.e. the size corrected critical energy release rates, comparable to the effective fracture toughness K_{Ic}^e , are shown in Figure 4.19. The values are on average 6.5 times bigger than G_f for the mode II experiments. It is assumed that a size correction function for the mode II experiments would result in a similar correction factor than for the mode I experiments, since the specimen size was the same. However, a specific size correction function was not developed for the mode II experiments. The methodology of Bazant and Planas (1998) would not have been applicable, because it is only valid for short edge cracks.

5.4 Field experiments

Tests were made in the field with isolated snow beams on an east-facing and 30° steep slope.

5.4.1 Failure behaviour

As explained in Section 4.3 the failure behaviour of the field tests could be divided into two categories. In the first category the weak layer failed over the whole beam area and in the second category the propagating fracture in the weak layer was arrested.

First the question has to be answered if what we observed was a true fracture process or if it was a global failure of the weak layer because the shear strength was overcome. That the shear strength was not overcome could be proved by the shear frame measurements, see Table 4.8. The shear strength was in all tests more than three times the effective shear stress applied on the remaining area of the weak layer. Two other evidences for a true fracture propagation were found. First, it was observed that a failure happened which did not fracture the whole weak layer. These failures could be heard by a cracking sound but could rarely be observed by eye because the snow did not offer enough contrast

to detect a fracture. However, occasionally the slab failed in a tensile failure ahead of the saw position, providing an evidence that a fracture had propagated a certain distance, generally between 20 cm and 50 cm. The position of such a tensile fracture seems to coincide with the location of the stress concentrations of the ANSYS simulation in Figure 4.25b. This image shows a stress concentration at a position ahead of the crack tip where such tensile fractures tended to occur. The second evidence is, that beams of different beam length l failed at the same critical cut length a_c . Since beams of different length were tested within meters on the same slab and at the same day, the differences in layer properties for the different beams can be neglected. Thus, a failure due to the strength exceeding stresses can definitely be excluded, since for the different beam length the failure area doubled or even tripled.

To conclude, field tests confirmed that a fracture started to propagate in a weak layer at a shear stress that was less than 30% of the shear strength of the weak layer, implying that a fracture mechanical processes led to the failure of the weak layer.

5.4.2 Energy release rate measured in the field

The geometry of the field experiments was modelled with finite elements. With this model the energy release rates were calculated.

By using the FE model a mean critical energy release rate of $G_f = 0.07 \pm 0.01 \text{ J/m}^2$ was found for the tested weak layer on 27 January 2006. This is about 65% higher than the value observed in the lab ($G_f \simeq 0.04 \text{ J/m}^2$). To compare these two values means to compare two characteristic values for two different weak layer types. One would assume that the weak layer tested in the field is less "weak" than the one tested in the laboratory, because the energy barrier that has to be overcome to fracture the weak layer is lower for the lab experiments. However, this did not coincide with our subjective impression of the weak layers. The weak layers tested in the field seemed to be weaker, from a visual and tactile point of view, than the ones tested in the laboratory. There are three explanations for this disagreement of subjective impression and results: First, the difference between the results is not large and since the results depended substantially on the numerous input parameters, the two results might have an error bar which is at least as large as the difference between the two values. Second, if a size effect is present as it was observed for fractures in mode I, what will most likely be the case, the G_f results of the field experiments will be higher, due to the larger specimen sizes in the field. Therefore, the effective critical energy release rate might be underestimated for the lab experiments compared to the field. Third, the compression tests showed for both weak layers results in the moderate stability range. This is a further indication that the stability of the weak layers was relatively similar.

The critical crack length a_c of our asymmetrical beam can be used to estimate a critical crack length in an intact slope. This can be done by calculating a_c^{sym} the critical cut or failure length in case of a symmetrical beam, i.e. a beam with an interior crack instead

of an edge crack. a_c^{sym} can be estimated by comparing Equation (2.45), the Equation for the half length of a critical crack r_c (Heierli and Zaiser, 2006) with Equation (4.21), the analytical calculation of a_c for our asymmetrical case. The result is

$$a_c^{sym} = 2 r_c = \sqrt[3]{36} a_c \simeq 2.45 a_c. \quad (5.3)$$

Thus, for our critical cut length of about 0.25 m, an a_c^{sym} of about 0.6 m results. A similar estimate was made by Kirchner et al. (2002a). From their experiments in homogeneous snow, Kirchner et al. (2002a) estimated the energy release rate to be of the order of 0.12 J/m². This would result in critical crack sizes in the order of tenth of centimeters. Our results confirm this estimate. The critical crack length is much less than the necessary length of more than 5 m that were proposed by various authors who modelled slab avalanche release (Bader and Salm, 1990; Stoffel and Bartelt, 2003) (see Section 1.3). The results correspond also to the suggestion of Bazant et al. (2003) that the crack half length r_c should be larger but in the order of the slab height H . However, a_c^{sym} is – like all the other mentioned critical crack length – still derived from two dimensional considerations. In a 3D case, a_c^{sym} is expected to slightly increase.

We can assume that disturbances a_c^{sym} of less than one meter in the weak layer can lead to a fracture propagation in snow. This is a size that can easily be destroyed by an over snow traveller (Schweizer and Camponovo, 2001).

In conclusion, the energy release rate G_f of a weak layer was for the first time measured in field experiments. The results for G_f are very low. Our results indicate that critical crack sizes of less than one meter might be required to start fracture propagation along a weak layer in a real slope.

5.4.3 FEM results

The FEM results showed, that even a small gap of 2 mm induced by a snow saw can provoke bending of the slab. The bending contributes a considerable amount of energy to the available energy for crack propagation.

Figure 4.26a compares the resulting energy release rates G for the case of a pure slope parallel shear loading of a crack tip (due to the fact that no gap is present between the cut surfaces) and for the case of a slope parallel shear loading combined with a slope normal bending component. For slope angles between 30° and 45°, i.e. in the relevant slope angle range for snow avalanche release, the combined loading provides much more energy per cracked area. No friction was considered between the cut interfaces for the pure shear case, therefore the curve (dots) in Figure 4.26 is an upper boundary. A critical energy release rate for the cracking of a weak layer can much easier be overcome by a combined loading.

In a second simulation with different Young's modulus for the slab and the basal layer (Figure 4.26b) it could be shown that the shape of the curves did not change, only the magnitude of the released energy G changed.

The assumption of a combined loading situation is not restricted to our field experiments. If a weak layer is collapsible, even a small collapse in the order of millimeters or even less (compare Figure 4.24) is sufficient to cause bending in the slab. However, a gap will not be present and the bending will be restricted by the collapsed weak layer but it will contribute to the total energy release rate. The resulting strain energy will thus be smaller than for the assumption of a gap.

Critical energy release rates or fracture toughness values which base on the shear fracture propagation model of McClung (1979) may therefore overestimate the actual values.

The small kink in the pure shear curve at a slope angle of 55° in Figure 4.24 originates from an opening moment that decreases the shear loading. For slope angles $\geq 55^\circ$ the crack has a mode I component due to bending of the slab in opposite direction of the bending for lower slope angles. This small kink and the point where the two curves start to coincide depend on the geometry of the modelled specimen. However, the qualitative behaviour will stay the same for geometry variations.

In conclusion, it was found that for our test beams a slope normal bending of the slab contributed considerably to the energy release rate G . Under certain conditions the bending component was more important than the component due to shear loading. It is assumed that this holds too for the fracture processes leading to slab release.

5.4.4 Analytical approach

The numerically obtained G_f results for our field experiments were compared to the results of an analytical solution for collapse in horizontal stratifications. The analytical solution was adapted from a model for a localized collapse of the weak layer in flat terrain proposed by Heierli and Zaiser (2006).

Due to the findings discussed in the last section a model which considers the slope normal component was adapted to our geometry.

The results obtained with the adapted analytical approach were about a factor of four lower than the modelled results. Several reasons lead to this underestimation of the critical energy release rate G_f : First, the energy contribution due to the shear forces acting at the crack tip, being a result of the slope angle φ (see Figure 4.26), are neglected. Second, the Young's modulus that was used in Equation (4.22), was derived from the SMP signal as an average over the layering of the slab height H . The determination of an equivalent Young's modulus for an arbitrary layered slab will be a challenging task. An equivalent Young's modulus applied to a homogeneous slab would result in the same deformation for a given load than the real layered slab. Third, the solution proposed by Heierli and Zaiser (2006) was developed for a thin beam, which means that the crack length is long in relation to the slab thickness ($a \gg H$), which leads to a minimal value for G_f , as the bending energy for a thick beam ($a \simeq H$) increases due to the shear deformation.

In conclusion, an analytical solution was found that shows a good correlation with the results of the FE simulation. The analytical results were lower by about a factor of four, for our specific geometry. However, further experiments will be necessary to approve these findings, it is assumed that the factor will change when the geometry or the weak layer properties change.

5.4.5 Further use of the field test

The field test proved to be reproducible and easy to perform. It is of high importance that every fracture experiment is accompanied with structural information, e.g. by SMP measurements. The SMP signal is used to evaluate the layering and to get an index of the elastic properties. This information is indispensable for a subsequent determination of the energy release rate. About 30 minutes are required to perform a compression test to identify the weak layer, one or two fracture tests and to acquire a SMP profile.

The field test is suited to assess the propensity for crack propagation in terms of the critical crack length or the critical energy release rate. Whereas the crack length gives information about how long a failure in the weak layer has to be until a fracture starts to propagate, the critical energy release rate provides information about the energy that is needed to fracture the weak layer. The energy release rate is a mechanical property of snow that has not been considered in field tests so far.

The advantage of this field test compared to common stability tests, such as the compression test, is that it does not only consider the weak layer but focuses on the interaction between the properties of the weak layer and the properties of the overlaying slab. This information is believed to be essential for slab avalanche release. Furthermore, it is assumed, that because the beams are long compared to a compression test, the fracture process zone might be fully incorporated in the beam and thus lead to results which are directly comparable to the processes in the snowpack without a size correction.

However more experiments will be needed. It will be important to test different types of weak layer to see how they influence the test results. If the field test should become a standard field test in snow science a calibration of the analytical solution or the analytical adaptation to thick beams would be necessary to replace the time consuming FEM simulations.

Conclusions

6.1 Summary

Fracture mechanical experiments with samples of naturally fallen snow were performed in the cold laboratory and in-situ with snow beams in the field. Three different types of experiments were designed or adapted to snow for fracture tests in mode I and mode II. By determining the critical stress intensity factor in mode I with different specimen sizes, the limitations of linear elastic fracture mechanics for snow could be quantified. A size correction function could be proposed. The energy release rate for a mode II fracture in a weak layer was evaluated in the laboratory and in the field. Layered snow specimens were used. Experimental and FEM results suggest that in case of slab avalanche release bending of the slab due to a slope normal collapse of the weak layer can supply a substantial amount of energy to the fracture process.

6.2 Conclusions

By applying new test methods to snow and acquiring a considerable data set of fracture mechanical properties of snow with laboratory and field tests, it was possible to improve the knowledge and the understanding of the fracture mechanical behaviour of snow and to experimentally confirm several hypotheses in snow mechanics.

In the following the Conclusions are structured according to the objectives that were defined for this thesis and presented in Section 1.4. The order of the objectives was rearranged to fit the structure of the thesis.

1. Assess the relevance of fracture toughness for fracture propagation resistance in snow and for snow slab release in general. Relate fracture toughness to other mechanical properties. (Objective 1)

Field tests confirmed that a fracture started to propagate in a weak layer at a shear stress that was less than 30% of the shear strength of the weak layer, implying that a fracture mechanical processes led to the failure of the weak layer.

Fracture mechanical parameters, such as the fracture toughness or the critical energy release rate, are essential to determine if a fracture under a certain loading condition can start to propagate or not. It might be one of the most important stability criteria for slab release.

Numerical slab release models base on fracture toughness as an input parameter. However, the experimental data on fracture mechanical properties were found to be scarce and only obtained from samples of homogeneous snow.

Fracture mechanical parameters were related to other material and mechanical properties such as the snow density and the Young's modulus, see the following paragraphs.

2. Design a suitable experimental setup and determine snow fracture toughness in tension for homogeneous snow samples. (Objective 2)

The classical three-point bending test method was successfully adapted to experiments with snow. The three-point bending test proved to be applicable and suitable for fracture mechanical experiments in mode I, as well as for the determination of the tensile strength.

Simultaneously to the three-point bending tests, cantilever beam tests were made. The critical stress intensity factors, K_{Ic} , of the cantilever beam tests were in general slightly higher than previously found values of similar tests. The discrepancy was attributed to a more appropriate evaluation method compared to previous studies.

Cantilever beam tests provided approximately 30% lower stress intensity factors than the three-point bending tests for specimens of the same snow type. The results of the cantilever beam tests depended furthermore on the cantilever length. The differences between the test methods were significant and attributed to non-negligible size and shape effects.

3. Quantify size and shape effects, so that the results of small scale experiments can be transferred to the slope scale. (Objective 4)

In order to investigate the size and shape-dependence of fracture toughness measurements on laboratory-sized specimens of snow, tests with three different specimen geometries and four different sizes were performed.

The three test geometries consisted of a three-point bending test and two cantilever beam tests with cantilever lengths of 10 cm and of 15 cm. A clear shape dependence of the critical stress intensity factor, K_{I_f} , was found for the different test geometries. The influence of an additional size effect was minimized by using the same specimen size for all three test methods.

In three-point bending tests with four different specimen sizes the size effect was experimentally determined and quantified according to Bazant and Planas (1998). The characteristic size D_0 , a measure for the "deviation" from linear elastic behaviour (Section 2.4.3), was determined to be about 30 cm for snow or about the same size as our specimens. The specimen size D should be about 25 times larger than D_0 in order to apply linear elastic fracture mechanics without a size correction.

As a method to correct the critical stress intensity factor to the size-independent material property K_{I_c} the equivalent fracture toughness, $K_{I_c}^e$, was determined according to Bazant and Planas (1998) and a size correction function based on the specimen size D was proposed: $K_{I_c}^e = \sqrt{1 + 0.29/D} K_{I_f}$. The results for $K_{I_c}^e$ ranged from $0.8 \text{ kPa}\sqrt{\text{m}}$ for a density of $\rho = 150 \text{ kg/m}^3$ up to $6 \text{ kPa}\sqrt{\text{m}}$ for a density of $\rho = 350 \text{ kg/m}^3$. This corresponds to an effective critical energy release rate G_c of 0.14 J/m^2 ($E = 4.7 \text{ MPa}$) and 0.62 J/m^2 ($E = 57 \text{ MPa}$) (Section 4.2.5). We confirmed that snow has an extremely low value of K_{I_c} .

The large D_0 suggests that fracture toughness is size dependent up to the scale of a slab avalanche.

The size of the fracture process zone, R_c , was estimated from measurements of the equivalent fracture toughness, $K_{I_c}^e$, and the tensile strength, σ_c , to be in the order of several centimeters. R_c was in the same order as the cut length or ligament length of our tests, and thus snow has to be considered as a quasi-brittle material at the scale of our experiments. For a quasi-brittle material linear elastic fracture mechanics (LEFM) is applicable only with a size correction. The assumption of snow as a quasi-brittle material could be experimentally confirmed.

If linear elastic fracture mechanics is used to describe snow failure, size and shape effects have to be taken into account when results of laboratory or field experiments have to be extrapolated to the slope scale. Therefore, appropriate scaling laws are essential. This might be of particular importance for slab release models or for stability assessment by numerical simulations of snow stratigraphy.

4. Design a suitable experimental setup and determine snow fracture toughness in shear for layered snow samples. (Objective 3)

Layered snow samples including a weak layer were tested in shear to determine the energy release rate of a crack propagating along the weak layer. A

new experimental setup was designed and proved to be applicable for layered samples.

In absence of an analytical solution, the finite element method (FEM) was used to simulate the experiments and determine the energy release rate numerically. A critical energy release rate of $G_f = 0.04 \pm 0.02 \text{ J/m}^2$ was found for the tested weak layers (mainly faceted crystals and mixed forms). No correlation was found between G_f and the elastic properties of the slab, the weak layer or the basal layer. However, G_f is expected to depend on the elastic properties of the weak layer for distinctly different weak layer types.

Two analytical approaches were tested and compared to the FEM results. Both analytical approaches, a homogeneous cantilever beam with a deep crack, and a bilayer beam with interface crack were highly correlated with the results obtained from the FE model. The analytical results were too large by a factor of about 2. Due to the higher coefficient of determination, the cantilever beam approach should be preferred.

For similar snow densities, critical energy release rates in mode I were on average a factor of about 2 higher than in mode II.

It is assumed that the size dependance of the critical energy release rate is in the same order as for the critical stress intensity factor in mode I, since the specimen had the same size. However, the size correction function of Bazant and Planas (1998) can not be adapted to mode II because it is only valid for short edge cracks.

5. Design a field test, based on the experience with the different laboratory tests and determine in-situ fracture mechanical properties. (Objective 6)

A new type of field test was developed in which isolated snow beams were tested in-situ on a slope. The field test is suited to assess the propensity for crack propagation in terms of the critical crack length or the critical energy release rate. Whereas the crack length gives information about how long a failure in the weak layer has to be until a fracture starts to propagate, the critical energy release rate provides information about the energy that is needed to fracture the weak layer.

A critical cut length of about 25 cm was required to start fracture propagation in the tested weak layers (mainly faceted crystals). The critical energy release rate was $G_f = 0.07 \pm 0.01 \text{ J/m}^2$. The critical energy release rate of a weak layer was for the first time measured in a field experiment.

The measured critical energy release rates G_f are expected to be much closer to the effective size independent critical energy release rate G_c . Since the beams are long, the fracture process zone might be fully incorporated in the beam and thus lead to results which are comparable to the processes in the snowpack without a size correction.

6. *Develop a conceptual model which relates measurable fracture mechanical properties of snow to the fracture processes involved in slab release. (Objective 5)*

In finite element simulations of our field test beams it was found that bending of the slab in slope normal direction contributes considerably to the energy release rate G and dominates the component due to shear loading for slope angles between 30° and 45° . Bending in slope normal direction can be the result of a gap induced by a snow saw but can also be the result of a collapse of the weak layer. It is assumed that this will hold for the real slab release case too.

Critical energy release rates or fracture toughness values calculated based on the shear fracture propagation model of McClung (1979) may therefore overestimate the actual values.

Critical crack length found in field tests can be multiplied by a factor of 2.5 to get a rough estimate of the required failure length in a slab. From our tests results, a failure length of less than one meter would result.

The specific fracture energy that has to be overcome to fracture a weak layer in the snowpack will depend on the material properties of the weak layer. In contrast, the available energy for crack propagation will mainly depend on the material properties of the overlaying slab and the slope normal collapse height of a weak layer, i.e. for a given weak layer with a given fracture energy the critical crack length will strongly depend on the slab properties.

7. *Additional work*

The tensile strength was measured in three-point bending tests. The results were comparable to previously published data. The main advantage was that strength and fracture mechanical experiments could be performed simultaneously, with specimens of the same size and snow type.

Mode I fracture speeds were derived from high-speed recordings. The maximum fracture speeds were about 20 m/s. As the samples were small the fracture speed was still accelerating and a terminal velocity could not be observed. The terminal velocity is assumed to be a factor of 1.5 to 5 higher than the measured fracture speeds.

The Young's modulus of our samples was determined in dynamic measurements with a frequency of 100 Hz using a prototype of a cyclic loading device. The device provided reliable and reproducible results which were at the upper limit of previously published data.

The results for the Young's modulus were strongly correlated with an index for the Young's modulus derived from a penetration resistance profile recorded with a snow micro-penetrometer SMP.

6.3 Outlook

We generally recommend for future fracture mechanical studies in snow, to concentrate on the determination of the energy release rate rather than on the stress intensity factor. This has several reasons: First, in most cases the additional information about the mode interaction at the crack tip is not needed. Second, apart from homogeneous materials a determination of the stress intensity factor is complex. Third, a global energy approach is more adequate and more intuitive to the avalanche release problem than a local stress field approach. Once, the sum of the contributory energies exceeds a given threshold a fracture can propagate.

There are two important points concerning a further development of the field test: First, different types of weak layers should be tested to see if, and how much their specific fracture energies vary. These results could be very important for stability assessment in numerical simulations of the snow stratigraphy. Therefore, a calibration of the analytical solution would be helpful, to replace the time consuming FEM simulations. Second, if the field test should become a standard field test for snow slope stability assessment, it should be investigated if it is not sufficient to measure the critical crack length a_c to judge the fracture propagation propensity. a_c is supposed to provide the combined information about how much energy can be released by the slab and how much is required to destroy the weak layer.

The interaction of slope parallel shear loading at the crack tip and slope normal collapse has to be further investigated. Therefore more simulations with different geometries and material properties would be helpful.

To derive the Young's modulus from SMP measurement is by far the simplest and fastest option, and the most suited one for field testing. Therefore for the future, the goal should be to further calibrate the conversion algorithm for the SMP penetration resistance to a Young's modulus. More experiments with different snow types will be required as well as a sound measurement technique for the Young's modulus which can serve as basis for the calibration. The cyclic loading device is promising in this respect but further verification will be needed.

The influence of slab layering on its elastic properties should be assessed in more detail. After all it will be of interest, if an equivalent Young's modulus of the slab can be determined or estimated from an SMP penetration resistance signal, this would simplify calculations or simulations considerably because a homogeneous slab could be assumed instead of a layered one. This could be done by determining an equivalent Young's modulus from the bending of a slab in field experiments or simulations. The problem to be solved would be to find an appropriate algorithm to convert the penetration resistance signal into an index for an equivalent Young's modulus which could be correlated with the field data.

For future studies, it should be considered to relate K_{Jf} to other mechanical properties

than snow density. A relation to the Young's modulus or the penetration resistance might decrease scatter considerably.

Seite Leer /
Blank leaf

Bibliography

- Ammann, W., Buser, O., and Vollenwyder, U. (1997). *Lawinen*. Birkhäuser Verlag, Basel, Switzerland.
- Anderson, T. (1995). *Fracture mechanics: fundamentals and applications*. CRC Press, Boca Raton, U.S.A., 2nd edition.
- Arons, E. M. and Colbeck, S. C. (1995). Geometry of heat and mass transfer in dry snow: A review of theory and experiment. *Reviews of Geophysics*, 33(4):463–493.
- Bader, H. and Salm, B. (1990). On the mechanics of snow slab release. *Cold Regions Science and Technology*, 17:287–300.
- Bader, H. P., Haefeli, R., Bucher, E., Thams, C., Neher, J., and Eckel, O. (1939). *Der Schnee und seine Metamorphose*. Kümmerly & Frey, Zürich, Switzerland, 3rd edition.
- Barenblatt, G. (1962). The mathematical theory of equilibrium of cracks in brittle fracture. *Advances in Applied Mechanics*, 7:55–129.
- Bazant, Z. and Planas, J. (1998). *Fracture and size effect in concrete and other quasibrittle materials*. CRC Press, Boca Raton, U.S.A.
- Bazant, Z., Zi, G., and McClung, D. (2003). Size effect law and fracture mechanics of the triggering of dry snow slab avalanches. *Journal of Geophysical Research*, 108(B2):2119.
- Birkeland, K. W., Kronholm, K., Logan, S., and Schweizer, J. (2006). Field measurements of sintering after fracture of snowpack weak layers. *Geophysical Research Letters*, 33:03501.
- Camponovo, C. and Schweizer, J. (2001). Rheological measurements of the viscoelastic properties of snow. *Annals of Glaciology*, 32:44–50.
- Colbeck, S., Akitaya, E., Armstrong, R., Gubler, H. U., Lafeuille, J., Lied, K., McClung, D., and Morris, E. (1990). *The international classification for seasonal snow on the ground*. International Commission of Snow and Ice of International Association of Scientific Hydrology / prep. by Working group on Snow Classification, Wallingford, U.K.

- Dempsey, J., Adamson, R., and Mulmule, S. (1999a). Scale effects on the in-situ tensile strength and fracture of ice. Part II: First-year sea ice at Resolute, N.W.T. *International Journal of Fracture*, 95:347–366.
- Dempsey, J., Defranco, S., Adamson, R., and Mulmule, S. (1999b). Scale effects on the in-situ tensile strength and fracture of ice. Part I: Large grained freshwater ice at Spray Lakes Reservoir, Alberta. *International Journal of Fracture*, 95:325–345.
- Erdogan, F. and Sih, G. (1990). On the crack extension in plates under plane loading and transverse shear. *Metallurgical Transactions A*, 21A:2419–2429.
- Evans, A., Ruhle, M., Dalgleish, B., and Charalambides, P. (1963). The fracture energy of bimaterial interfaces. *Journal of Basic Engineering*, 85:519–527.
- Faillettaz, J., Daudon, D., Bonjean, D., and Louchet, F. (2002). Snow toughness measurements and possible applications to avalanche triggering. In Stevens, J., editor, *Proceedings ISSW 2002. International Snow Science Workshop*, pages 540–543, Pen-ticton BC, Canada, 29 September–4 October 2002.
- Fyffe, B. and Zaiser, M. (2004). The effects of snow variability on slab avalanche release. *Cold Regions Science and Technology*, 40:229–242.
- Gauthier, D. and Jamieson, J. B. (2006). Towards a field test for fracture propagation propensity in weak snowpack layers. *Journal of Glaciology*, 52(176):164–168.
- German, R. M. (1996). *Sintering theory and practice*. John Wiley and Sons Inc., New York, U.S.A.
- Gibson, L. and Ashby, M. (1997). *Cellular solids: structure and properties*. Cambridge University Press, Cambridge, U.K., 2nd edition.
- Golubev, V. N. and Frolov, A. D. (1998). Modelling the change in structure and mechanical properties in dry-snow densification to ice. *Annals Of Glaciology*, 26:45–50.
- Good, W. (1987). Thin sections, serial cuts and 3-d analysis of snow. In *Davos symposium on avalanche formation, movement and effects*, volume 162, pages 35–47. IAHS Publication.
- Gränicher, H. (1996). *Messung beendet - was nun?* Teubner, Stuttgart, Germany.
- Griffith, A. (1921). The phenomena of rupture and flow in solids. *Philosophical Transactions of the Royal Society of London, Series A*, 221:163–197.
- Gross, D. and Seelig, T. (2001). *Bruchmechanik: mit einer Einführung in die Mikromechanik*. Springer-Verlag, Berlin, Germany, 3rd edition.
- Heierli, J. (2005). Solitary fracture waves in metastable snow stratifications. *Journal of Geophysical Research-Earth Surface*, 110(F2).

- Heierli, J. and Zaiser, M. (2006). An analytical model for fracture nucleation in collapsible stratifications. *Geophysical Research Letters*, 33:06501.
- Hempel, F. (2004). Evaluation of the macro-elastic-modulus of snow. Technical report, Internal report SLF.
- Hutchinson, J. W. and Suo, Z. (1992). Mixed-mode cracking in layered materials. *Advances in Applied Mechanics*, 29:63–191.
- Irwin, G. R. (1957). Analysis of stresses and strains near the end of a crack traversing a plate. *Journal of Applied Mechanics*, 24:361–364.
- Irwin, G. R. (1958). *Fracture*, volume 6. Springer-Verlag, Berlin, Germany.
- Jamieson, J. and Johnston, C. (1990). In-situ tensile tests of snowpack layers. *Journal of Glaciology*, 36(122):102–106.
- Jamieson, J. B. (1999). The compression test - after 25 years. *The Avalanche Review*, 18(1):10–12.
- Jamieson, J. B. and Johnston, C. (2001). Evaluation of the shear frame test for weak snowpack layers. *Annals of Glaciology*, 32:59–68.
- Jamieson, J. B. and Schweizer, J. (2000). Texture and strength changes of buried surface hoar layers with implications for dry snow-slab avalanche release. *Journal of Glaciology*, 46(152):151–160.
- Johnson, B. C., Jamieson, J. B., and Stewart, R. R. (2004). Seismic measurement of fracture speed in a weak snowpack layer. *Cold Regions Science and Technology*, 40(1-2):41–45.
- Johnson, J. and Schneebeli, M. (1999). Characterizing the microstructural and micromechanical properties of snow. *Cold Regions Science and Technology*, 30(1-3):91–100.
- Kirchner, H., Michot, G., and Schweizer, J. (2002a). Fracture toughness of snow in shear and tension. *Scripta Materialia*, 46(6):425–429.
- Kirchner, H., Michot, G., and Schweizer, J. (2002b). Fracture toughness of snow in shear under friction. *Physical Review E*, 66(2):027103(3).
- Kirchner, H., Michot, G., and Suzuki, T. (2000). Fracture toughness of snow in tension. *Philosophical Magazine A*, 80(5):1265–1272.
- Kronholm, K. (2004). *Spatial variability of snow mechanical properties*. PhD thesis, University of Zürich.
- Kronholm, K. and Birkeland, K. W. (2005). Integrating spatial patterns into a snow avalanche cellular automata model. *Geophysical Research Letters*, 32:19504.

- Kronholm, K., Schneebell, M., and Schweizer, J. (2004). Spatial variability of micropenetration resistance in snow layers on a small slope. *Annals Of Glaciology*, 38:202–208.
- Kronholm, K. and Schweizer, J. (2003). Snow stability variation on small slopes. *Cold Regions Science And Technology*, 37:453–465.
- Malyshev, B. M. and Salganik, R. L. (1965). Strength of adhesive joints using theory of cracks. *International Journal of Fracture Mechanics*, 1(2):114–128.
- McClung, D. M. (1979). Shear fracture precipitated by strain softening as a mechanism of dry slab avalanche release. *Journal Of Geophysical Research*, 84(NB7):3519–3526.
- McClung, D. M. (1981). Fracture mechanical models of dry slab avalanche release. *Journal of Geophysical Research*, 86(NB11):10783–10790.
- McClung, D. M. (1987). Mechanics of snow slab failure from a geotechnical perspective. In *Davos Symposium on Avalanche formation, movement and effects*, volume 162, pages 475–508. IAHS Publication.
- McClung, D. M. (1996). Effects of temperature on fracture in dry slab avalanche release. *Journal of Geophysical Research - Solid Earth*, 101:21907–21920.
- McClung, D. M. (2005a). Approximate estimates of fracture speeds for dry slab avalanches. *Geophysical Research Letters*, 32(8).
- McClung, D. M. (2005b). Dry slab avalanche shear fracture properties from field measurements. *Journal of Geophysical Research - Earth Surface*, 110(F4):04005.
- McClung, D. M. and Schaerer, P. (1993). *The Avalanche Handbook*. The Mountaineers, Seattle, U.S.A.
- McClung, D. M. and Schweizer, J. (1999). Skier triggering, snow temperatures and the stability index for dry slab avalanche initiation. *Journal of Glaciology*, 45(150):190–200.
- Mellor, M. (1975). A review of basic snow mechanics. In *Symposium at Grindelwald 1974–Snow Mechanics*, volume 114, pages 251–291. IAHS Publication.
- Narita, H. (1980). Mechanical behaviour and structure of snow under uniaxial tensile stress. *Journal of Glaciology*, 26(94):275–282.
- Narita, H. (1983). An experimental study on tensile fracture of snow. *Contributions from the Institute of Low Temperature Science, Hokkaido University, Sapporo, Japan. Series A , No. 32*, pages 1–37.
- Palmer, A. and Rice, J. (1973). The growth of slip surfaces in the progressive failure of over-consolidated clay. *Proceedings of the Royal Society of London Series A*, 332:527–548.

- Perla, R. (1977). Slab avalanche measurements. *Canadian Geotechnical Journal*, 14(2):206–213.
- Perla, R., Beck, T. M. H., and Cheng, T. T. (1982). The shear-strength index of alpine snow. *Cold Regions Science and Technology*, 6:11–20.
- Rafiee, S., Gross, D., and Seelig, T. (2004). The influence of microcrack nucleation on dynamic crack growth - a numerical study. *Engineering Fracture Mechanics*, 71:849–857.
- Rice, J. (1988). Elastic fracture-mechanics concepts for interfacial cracks. *Journal of Applied Mechanics-Transactions of the ASME*, 55:98–103.
- Scapozza, C. (2004). *Entwicklung eines dichte- und temperaturabhängigen Stoffgesetzes zur Beschreibung des visko-elastischen Verhaltens von Schnee*. PhD thesis, ETH Zürich.
- Schindler, H. (1996). Size effects on fracture toughness of brittle materials. *International Journal of Fracture*, 82:R3–R10.
- Schindler, H. (2004). *Grundlagen der Bruchmechanik*. Lecture Notes. ETH, Zürich.
- Schneebeli, M. (2002). The importance of the microstructure of snow in nature and engineering. In Brebbia, C. A., Sucharov, L. J., and Pascolo, P., editors, *Design and nature: Comparing design in nature with science and engineering (First International Conference, Udine, Italy)*, pages 87–93. WIT Press, Southampton, Boston.
- Schneebeli, M. and Johnson, J. B. (1998). A constant speed penetrometer for high resolution stratigraphy. *Annals of Glaciology*, 26:107–111.
- Schneebeli, M., Pielmeier, C., and Johnson, J. B. (1999). Measuring snow microstructure and hardness using a high resolution penetrometer. *Cold Regions Science and Technology*, 30(1-3):101–114.
- Schweizer, J. (1998). Laboratory experiments on shear failure of snow. *Annals of Glaciology*, 26:97–102.
- Schweizer, J. (1999). Review of dry snow slab avalanche release. *Cold Regions Science and Technology*, 30(1-3):43–57.
- Schweizer, J. (2002). Zufall und Muster. Die Variabilität der Schneedecke in neuem Licht. *Berg & Steigen*, 4/02:53–56.
- Schweizer, J. and Camponovo, C. (2001). The skier's zone of influence in triggering slab avalanches. *Annals of Glaciology*, 32:314–320.
- Schweizer, J. and Camponovo, C. (2002). The temperature dependence of the effective elastic shear modulus of snow. *Cold Regions Science and Technology*, 35:55–64.

- Schweizer, J. and Jamieson, J. (2003). Snowpack properties for snow profile interpretation. *Cold Regions Science and Technology*, 37(3):233–241.
- Schweizer, J., Jamieson, J., and Schneebeli, M. (2003). Snow slab avalanche formation. *Reviews of Geophysics*, 41(4):1016.
- Schweizer, J. and Lütschg, M. (2001). Characteristics of human-triggered avalanches. *Cold Regions Science and Technology*, 33:147–162.
- Schweizer, J., Michot, G., and Kirchner, H. O. K. (2004). On the fracture toughness of snow. *Annals of Glaciology*, 38:1–8.
- Sigrist, C., Schweizer, J., Schindler, H., and Dual, J. (2005). On size and shape effects in snow fracture toughness measurements. *Cold Regions Science and Technology*, 43(1-2):24–35.
- Sigrist, C., Schweizer, J., Schindler, H., and Dual, J. (2006). The energy release rate of mode II fractures in layered snow samples. *International Journal of Fracture*, 139(3-4):461–475.
- Sinha, N. (1978). Short-term rheology of polycrystalline ice. *Journal of Glaciology*, 21(85):457–473.
- Stearns, S. R. (1964). Flexural properties of snow and snow-ice. Technical Report (Special Report 59), US Army CRREL, Hanover, New Hampshire, USA.
- Stoffel, M. and Bartelt, P. (2003). Modelling snow slab release using a temperature-dependent viscoelastic finite element model with weak layers. *Surveys in Geophysics*, 24:417–430.
- Studer, J. and Koller, M. (1997). *Bodendynamik – Grundlagen, Kennziffern, Probleme*. Springer-Verlag, Berlin, Germany, 2nd edition.
- Sumpter, J. D. G. (1991). Pop-in fracture - observations on load drop, displacement increase, and crack advance. *International Journal of Fracture*, 49:203–218.
- Suo, Z. G. and Hutchinson, J. W. (1990). Interface crack between two elastic layers. *International Journal of Fracture*, 43(1):1–18.
- Tada, H., Paris, P. C., and Irwin, G. R. (2000). *The stress analysis of cracks handbook*. Paris Productions, MO, Saint Louis.
- Tschirky, F., Brabec, B., and Kern, M. (2000). Avalanche rescue systems in Switzerland: Experience and limitations. In *Proceedings of the International Snow Science Workshop, Big Sky, Montana, U.S.A., 1-6 October, 2000*, pages 369–376, Montana State University, Bozeman, U.S.A.
- van Herwijnen, A. and Jamieson, B. (2005). High-speed photography of fractures in weak snowpack layers. *Cold Regions Science and Technology*, 43:71–82.

Wei, Y., Adamson, R., and Dempsey, J. (1996). Ice/metal interfaces: fracture energy and fractography. *Journal of Materials Science*, 31:943–947.

Zaiser, M. (2004). Slab avalanche release viewed as interface fracture in a random medium. *Annals of Glaciology*, 38:9–14.

Seite Leer /
Blank leaf

Calculation of errors

A.1 The error of σ_N

In this section the calculation of the error for the nominal stress σ_N of a three-point bending test, defined in Equation (3.3), will be detailed.

By substitution of Equations (3.1) and (3.2) into Equation (3.3), σ_N is expressed as a function of the specimen dimensions l , s , h and w , the force F and the density ρ

$$\sigma_N = \frac{6}{h^2} \left\{ \frac{Fs}{4w} + \frac{h\rho g}{8} [s^2 - (l-s)^2] \right\}. \quad (\text{A.1})$$

The dimensions of the specimen could be measured with a precision of 5 mm. Thus, $\Delta l = \Delta s = \Delta h = \Delta w = \pm 0.005$ m. Divided by the standard specimen dimensions (Table 3.1), following relative errors result:

$$\frac{\Delta l}{l} \simeq 1\%,$$

$$\frac{\Delta s}{s} \simeq 1.2\%,$$

$$\frac{\Delta h}{h} \simeq 2.5\%,$$

$$\frac{\Delta w}{w} \simeq 5\%.$$

The error of the density measurement was $\Delta\rho = \pm 10$ kg/m³ and the force was measured

with a precision of $\Delta F = \pm 0.02 \text{ N}$, resulting in relative errors of

$$\frac{\Delta \rho}{\rho} \geq 2.5\%,$$

$$\frac{\Delta F}{F} < 0.1\%.$$

In the following, errors smaller or around 1% were neglected. Thus, only h , w and ρ were considered in the error calculation. Equation (A.2) can thus be rearranged to

$$\sigma_N = c_1 w^{-1} h^{-2} + c_2 \rho h^{-1}, \quad (\text{A.2})$$

with $c_1 = 3/2 Fs$ and $c_2 = 3/4(s^2 - (l - s)^2)g$. According to the elementary laws of error propagation (e.g. Gränicher, 1996) the error of $A = w^{-1}h^{-2}$ and $B = \rho h^{-1}$ can be calculated as

$$\left(\frac{\Delta A}{A}\right)^2 = \left(\frac{\Delta w}{w}\right)^2 + 4\left(\frac{\Delta h}{h}\right)^2, \quad (\text{A.3})$$

$$\left(\frac{\Delta B}{B}\right)^2 = \left(\frac{\Delta \rho}{\rho}\right)^2 + \left(\frac{\Delta h}{h}\right)^2. \quad (\text{A.4})$$

The error of σ_N can then be calculated as

$$\Delta \sigma_N^2 = c_1^2 \Delta A^2 + c_2^2 \Delta B^2, \quad (\text{A.5})$$

and by substitution:

$$\begin{aligned} \Delta \sigma_N^2 = & \left(\frac{3Fs}{2}\right)^2 \frac{1}{w^2 h^4} \left[\left(\frac{\Delta w}{w}\right)^2 + 4\left(\frac{\Delta h}{h}\right)^2 \right] + \\ & \left(\frac{3}{4}(s^2 - (l - s)^2)g\right)^2 \frac{\rho^2}{h^2} \left[\left(\frac{\Delta \rho}{\rho}\right)^2 + \left(\frac{\Delta h}{h}\right)^2 \right]. \end{aligned} \quad (\text{A.6})$$

Stratigraphic snow cover profiles

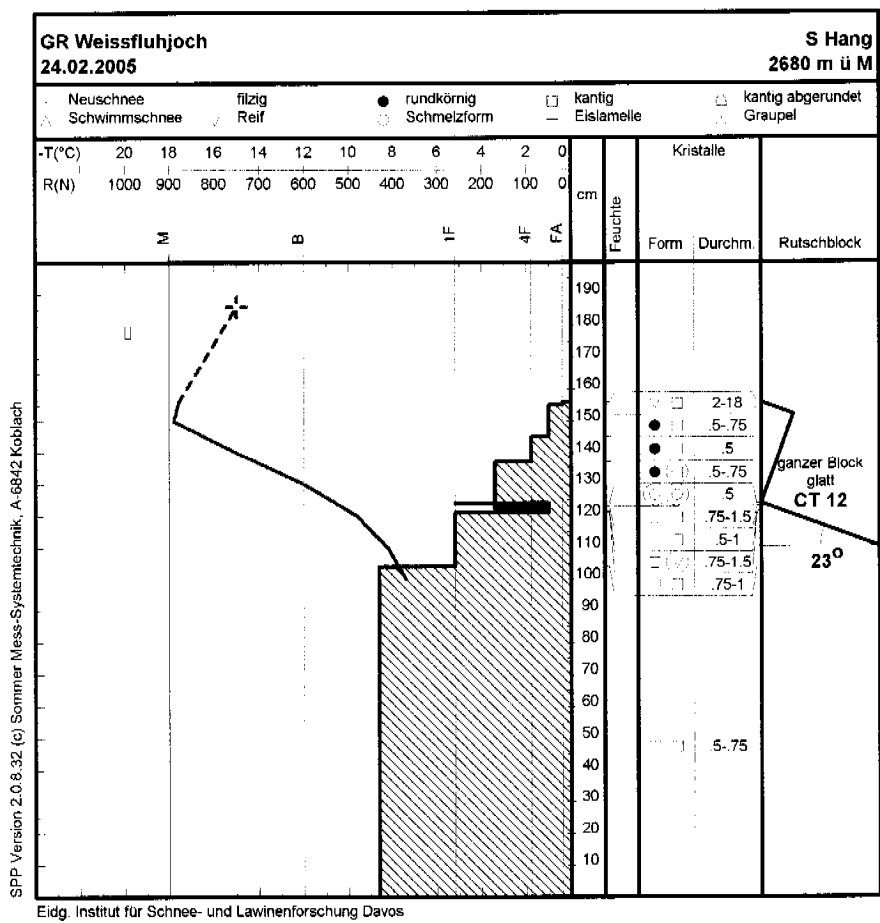


Figure B.1: Stratigraphic snow cover profile including the weak layers tested in series 2A and 2B.

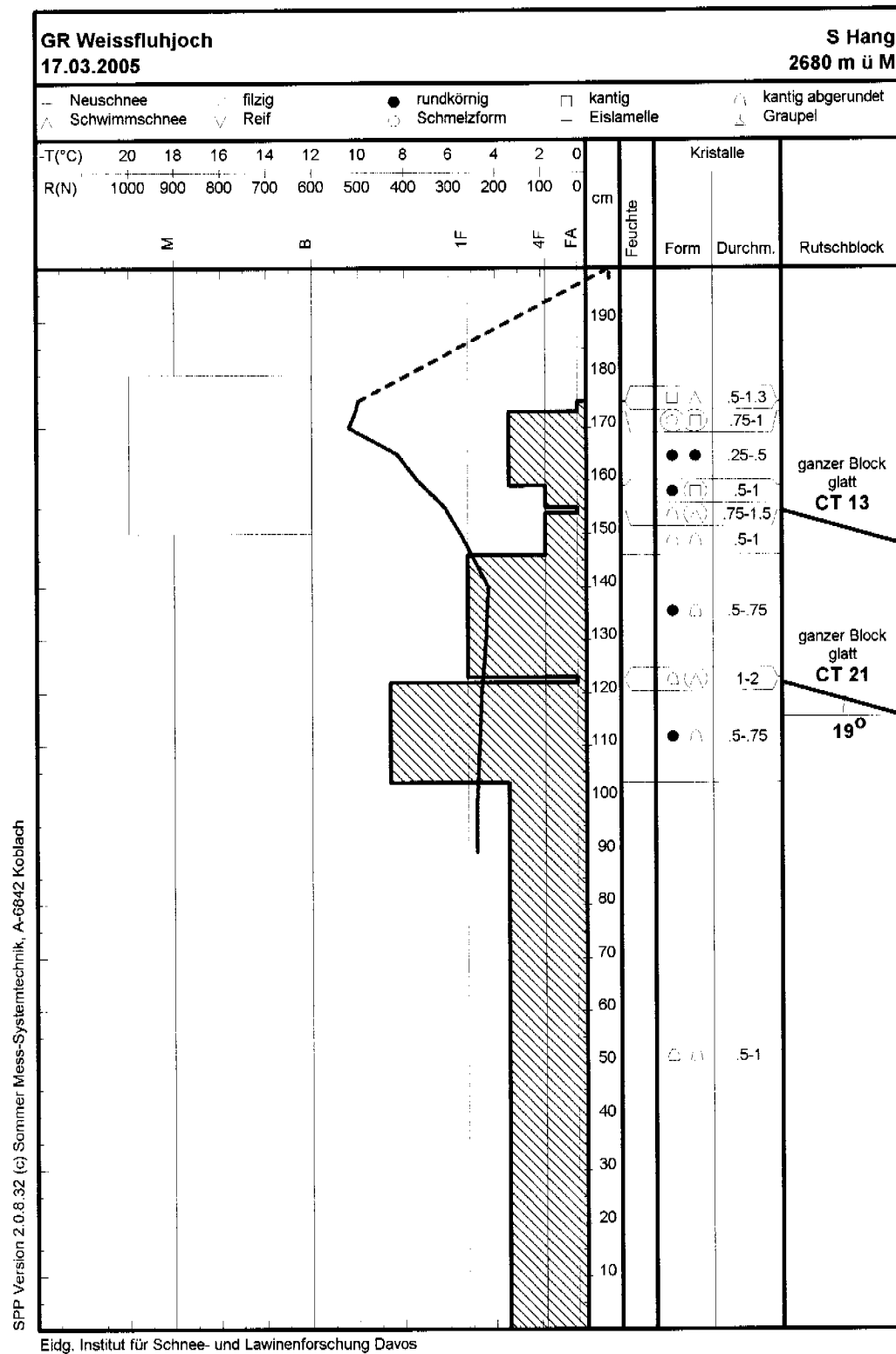


Figure B.2: Stratigraphic snow cover profile including the weak layers tested in series 2C and 2D.

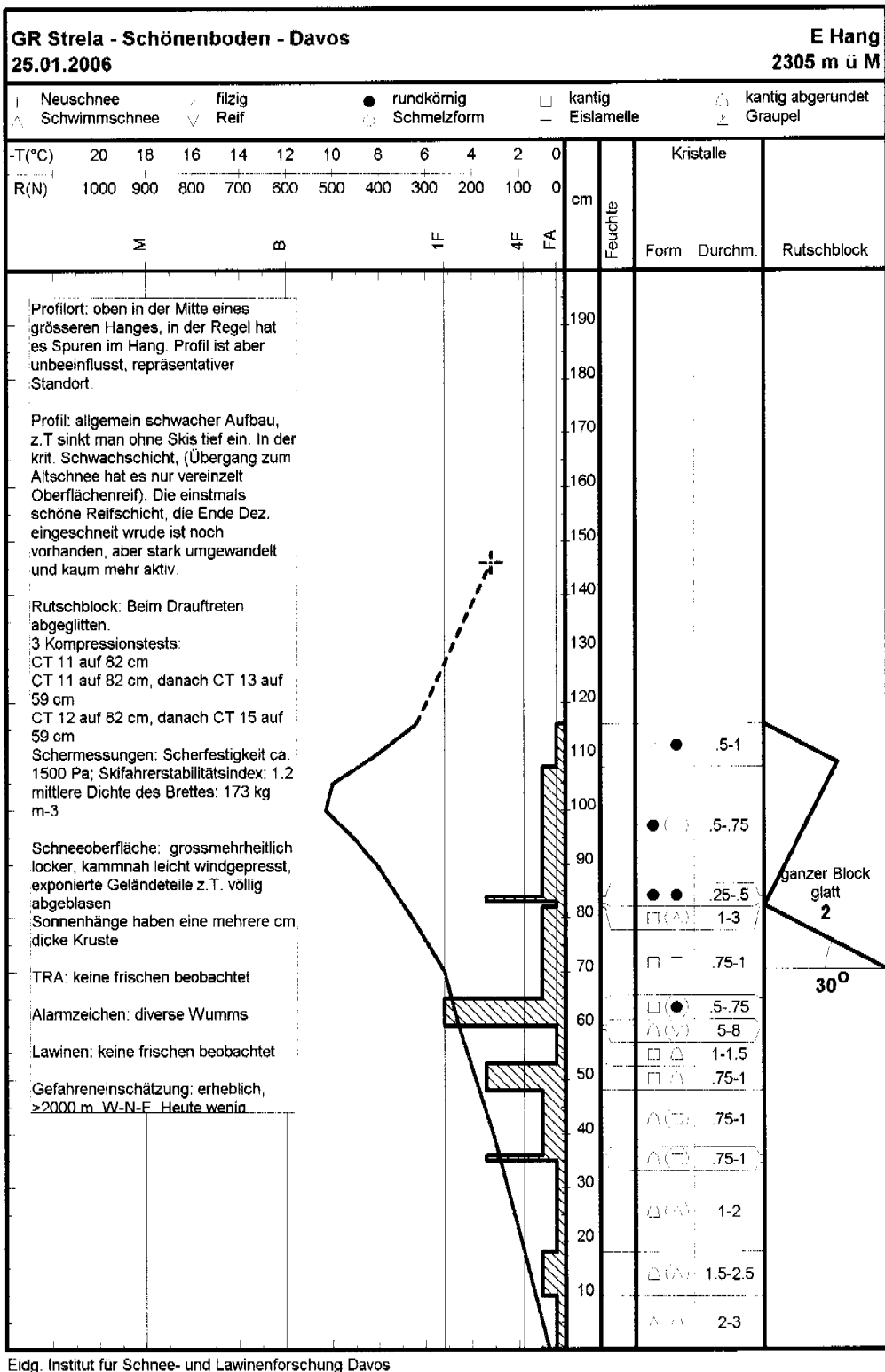


Figure B.3: Stratigraphic snow cover profile of the field test day on 25 January 2006.

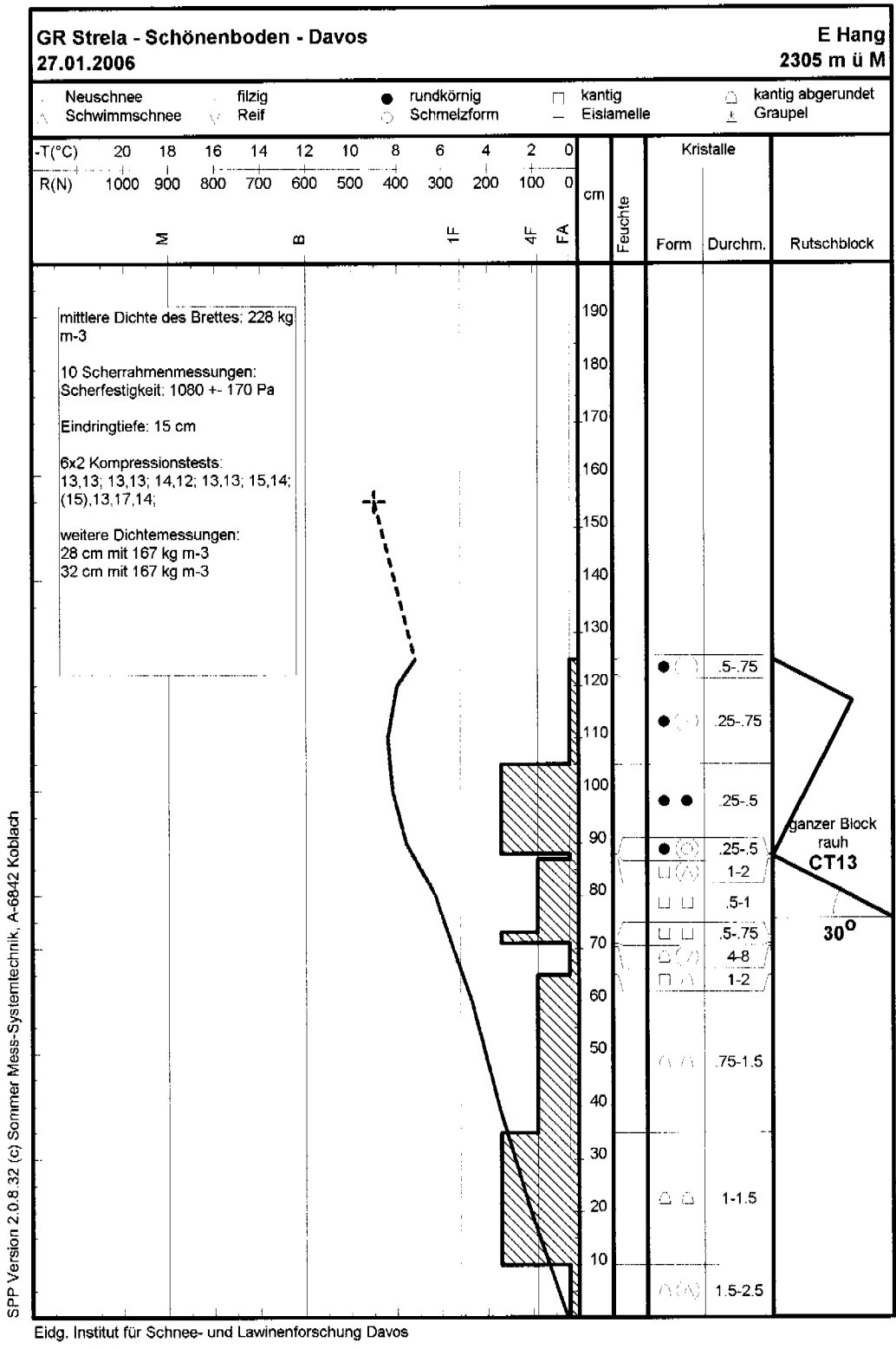


Figure B.4: Stratigraphic snow cover profile of the field test day on 27 January 2006.

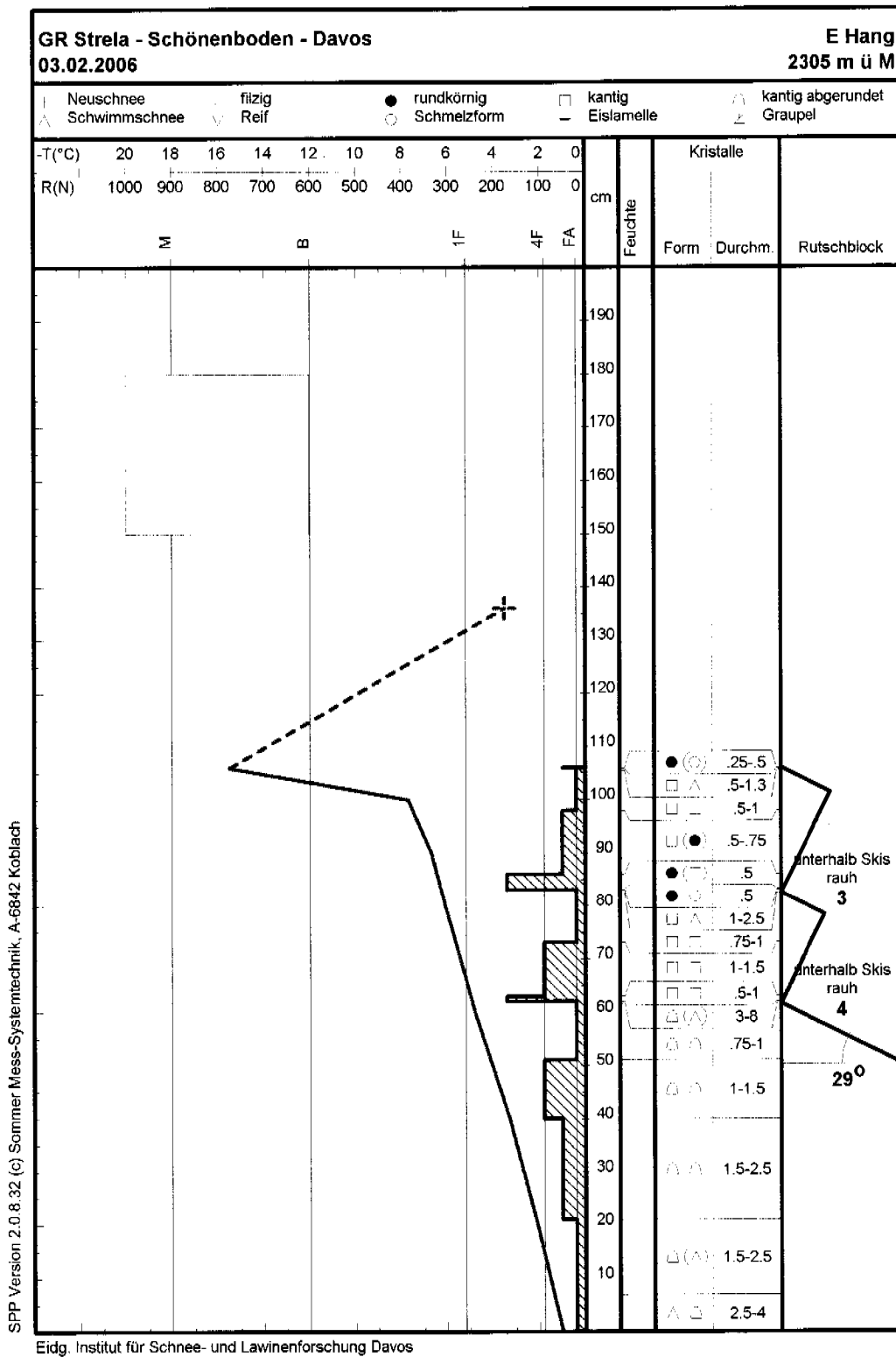


Figure B.5: Stratigraphic snow cover profile of the field test day on 3 February 2006.

Seite Leer /
Blank leaf

Acknowledgements

Jürg Schweizer was my adviser at the SLF over the past three years. During this time he was also a teacher and mentor to me. Under his guidance I was able to enhance my scientific skills and to benefit from his profound knowledge of snow and of avalanche release. Despite his workload, his door was always open whenever questions arose. Therefore, I wish to express my deep gratitude to him.

I would like to thank Prof. Jürg Dual, head of the Center of Mechanics at ETH Zürich, who offered me the opportunity to write my thesis under his supervision. Our bi-monthly meetings in Zürich became the "anchor points" throughout these three years.

Hans-Jakob Schindler an expert in fracture mechanics was my co-supervisor. I would like to thank him especially for his fast and concise replies on all my fracture mechanical questions, even though most of our communication had to take place by email.

A special thank goes to Joachim Heierli. In countless discussions we used piles of paper for our drawings and notes, and finally saw clearer into the complexities of fracturing snow beams and collapsing weak layers. In addition, he was so kind as to review my thesis.

My thanks go to my group head, Martin Schneebeli. Due to him, the working climate was ever agreeable and fruitful.

Denes Szabo was the man for any problem concerning the ANSYS workbench. My thanks go to him.

Felix Book, Ruzica Dadic, Nora Staack and Daniela Schmid helped with the experiments in the cold lab. In their company the cold temperatures were much easier to bear. Sincere thanks are given to all of them.

Cordial thanks go to my office mates Kalle Kronholm and Margret Matzl. Kalle familiarized me with what it meant to be a PhD student. I appreciated the great time and the many laughs in his company. He became much more than just an office mate to me. Thanks to Margret, the long days and nights in the office, while we both wrote up our theses, were much less boring. And thanks to her, the food supply never ran dry!

Mathieu Fauve granted me asylum during my first month in Davos. He also shared my passion for flying discs. Merci beaucoup, Mat!

My most cordial thanks go to my parents, Hedi and Paul Sigrüst and my sister Daniela, who supported me during all these years.

And finally, thank you Flurina for letting me share life and love with you.

Curriculum Vitae

Personal data

Name Christian Sigrist
Date of birth March 24, 1976
Place of origin Sigriswil (BE), Switzerland
Nationality Swiss
Languages German (mothertongue), English (spoken, written),
French (spoken, written)

Education

1983–1987 Primary school in Heimberg, Switzerland
1987–1992 Secondary school in Heimberg, Switzerland
1992–1996 Gymnasium in Thun, Switzerland
1996 **Matura Type C** (Natural sciences) at Gymnasium Thun
1996–2001 Studies in Physics, Mathematics and Astronomy at the *University of Bern*, Switzerland
2000–2001 Master's thesis in Physics at the Division for Space Research and Planetary Sciences (Physikalisches Institut) of the *University of Bern*, Switzerland, entitled "Self Optimisation of a Time of Flight Mass Spectrometer based on a Simplex Algorithm", Supervisors: Prof. Dr. Kathrin Altwegg, Prof. Dr. Hans Balsiger
2001 Graduated as **Master of Science in Physics**

Academic record

2002 Temporary assistant at the Processor Architecture Laboratory of the *Ecole Polytechnique Fédéral de Lausanne EPFL* in Lausanne, Switzerland
2002–2003 Scientific employee at the Institute for Surgical Technology and Biomechanics of the *Maurice E. Müller Research Center* in Bern, Switzerland
2003–2006 PhD studies at the *Swiss Federal Institute for Snow and Avalanche Research SLF* in Davos, Switzerland and the Center of Mechanics (Department of Mechanical and Process Engineering) at the *Swiss Federal Institute of Technology ETH* in Zürich, Switzerland, entitled "Measurement of Fracture Mechanical Properties of Snow and Application to Dry Snow Slab Avalanche Release" under the supervision of Prof. Dr. Jürg Dual, Dr. Jürg Schweizer and Dr. Hans-Jakob Schindler